Density Functional Theory applied to liquid metals and
the Adjacent Pairs Exchange correction to the Random Phase
Approximation

Draft 0.8

Felix Hummel

supervisor: Prof. Georg Kresse

September 2, 2015

Draft 0.8

Contents

Draft 0.8

Part III

The Adjacent Pairs Exchange correction to the Random Phase Approximation

Chapter 5

Many Body Perturbation Theory

Density Functional Theroy (DFT) calculations are sufficiently accurate for many applications. However its description of electronic correlation is just approximated locally from the uniform electron gas. It lacks, for instance, indirect effects of the electron-electron interaction, such as Van-der-Walls force where electrostatic repulsion deforms the distribution of electrons and these polarized electron distributions in turn can attract each other. This effect can not be captured by DFT or HF as they only take the instantaneous electrostatic interaction into consideration but the formation of the polarized electron distributions requires time. The missing descriptions of such dynamical effects is referred to as *dynamical correlation* (Shavitt and Bartlett 2009).

Static correlation occurs when the DFT or HF approximation is not appropriate for the chemical environment per se. A good example is the the dissociation of a hydrogen ion where the protons are already at a great distance. The single electron should be in a superposition of two states, quite localized at each respective proton. DFT rather places half an electron on each proton and yields just one orbital spanning both protons.

Perturbation theory expands properties of the exact solution of the Schrödinger equation in terms of the orbitals and orbital energies of the corresponding Hartree-Fock approximation. One can also start from DFT orbitals or from other reference which is feasible to solve. It is mostly the dynamic correlation that is captured by the perturbation expansion but it can also include some static correlation when going to sufficiently many terms. In cases where the static correlation is large multi reference perturbation theory may be required. Not unlike a Taylor expansion, a perturbation expansion is not guaranteed to converge or may converge slowly with the number of terms included. The convergence also strongly depends on the quality of the reference state.

We will use time dependent many body perturbation theory following the original derivation of (Goldstone 1957) as it is independent of the reference system (DFT or HF) and it is extensive. Extensivity means that for two systems A and B the energy of the combined system equals the sum of the energy of the individual constituents

$$E(AB) = E(A) + E(B),$$

assuming an identical chemical environment. The time dependent formulation of perturbation theory also lends itself naturally to Goldstone diagrams to visualize terms occurring in the perturbation expansion.

Complementary treatments can be found in (Kutzelnigg 2009; Lancaster and Blundell 2014; Shavitt and Bartlett 2009; Fetter and Walecka 2003; Coleman 2015).

5.1   Time dependent perturbation theory

In perturbation theory the exact Hamiltonian is separated into the unperturbed part $\hat{H}_0$, which can be solved, and the perturbation $\hat{H}_1$, which contains the full Coulomb electron-electron interaction:

$$\hat{H} = \underbrace{\hat{T} + \hat{V}_{\text{ne}} + \hat{V}_{\text{eff}}}_{\hat{H}_0} + \underbrace{\hat{V}_{ee} - \hat{V}_{\text{eff}}}_{\hat{H}_1}.$$

$\hat{V}_{\text{eff}}$ is the effective interaction employed by the reference, e.g. the Hartree-Fock approximation. Note that this effective interaction included in $\hat{H}_0$ must be subtracted again by the perturbation to arrive at results of the full Hamiltonian.

Let ψ_p be the spin-orbitals of the unperturbed Hamiltonian of the HF or DFT reference and let $|\Phi\rangle$ denote the Slater determinant of the ground state, where the lowest N states are occupied by the N electrons present in the system. These states are called *unexcited states* while the states that are unoccupied in $|\Phi\rangle$ are called *excited* states. We will use the letters $i, j, k, \ldots$ to label unexcited states, $a, b, c, \ldots$ to label excited states and $p, q, r, \ldots$ to label general states. We can write $|\Phi\rangle$ in second quantization as the result of applying the electron creation operator $\hat{c}_i^\dagger$ for all unexcited states i on the vacuum state, $|\,\rangle$, without any electrons:

$$|\Phi\rangle = \prod_i \hat{c}_i^\dagger \,|\,\rangle = \hat{c}_1^\dagger \ldots \hat{c}_N^\dagger \,|\,\rangle.$$

Note that each application of $\hat{c}_i^\dagger$ changes the number of particles and thus the dimensionality of the Hilbert space. The states of second quantization are elements of the union of all Hilbert spaces of zero particles, one particle, two particle and so forth, which is called *Fock-space*. The beauty of second quantization is that it hides all the tedious footwork of anti-symmetrization in the algebra of the creation and annihilation operators, which is completely given by the anti-commutator relations:

$$\{\hat{c}_p^\dagger, \hat{c}_q^\dagger\} = 0 \qquad \{\hat{c}_p, \hat{c}_q\} = 0 \qquad \{\hat{c}_p^\dagger, \hat{c}_q\} = \delta_{pq}, \tag{5.1}$$

where $\{\hat{A}, \hat{B}\} = \hat{A}\hat{B} + \hat{B}\hat{A}$. One immediate consequence of the these relations is the Pauli exclusion principle disallowing two fermions in the same state:

$$\hat{c}_p^\dagger \hat{c}_p^\dagger \,|\,\rangle = \frac{1}{2}\{\hat{c}_p^\dagger, \hat{c}_p^\dagger\}\,|\,\rangle = 0.$$

Note that the vacuum, $|\,\rangle$, is a state while the number 0 is not.

The Fock-space used for the creation and annihilation operators is spanned by the Slater determinants of the eigenfunctions ψ_p of the unperturbed Hamiltonian $\hat{H}_0$. $\hat{H}_0$ is therefore diagonal, counting the eigenenergy ε_p for each occupied state p, irrespective of whether it is an excited or unexcited state:

$$\hat{H}_0 = \sum_p \varepsilon_p \hat{c}_p^\dagger \hat{c}_p. \tag{5.2}$$

5.1.1   Particle/hole picture

Let us now introduce the particle/hole picture where we want to consider the non-interacting ground state $|\Phi\rangle$ as the new vacuum state instead of the true vacuum, $|\,\rangle$, without any

electrons. In this picture we care about the difference to the non-interacting ground state $|\Phi\rangle$ and we only count excited states that are now occupied called *particles*, and unexcited states that are no longer occupied called *holes*. While $\hat{c}_a^\dagger$ indeed creates a particle in an excited state, a hole in an unexcited state has to be created by annihilating a formerly occupied state by $\hat{c}_i$. For unexcited states below the Fermi energy the meaning of creation and annihilation has to be reversed. We define the creation and annihilation operators for particles $(\hat{a}^\dagger, \hat{a})$ and for holes $(\hat{i}^\dagger, \hat{i})$:

$$
\begin{array}{llll}
\hat{a}^\dagger = \hat{c}_a^\dagger & \hat{a} = \hat{c}_a & \text{for} & \varepsilon_a > \varepsilon_{\mathrm{F}} \\
\hat{i}^\dagger = \hat{c}_i & \hat{i} = \hat{c}_i^\dagger & \text{for} & \varepsilon_i \leq \varepsilon_{\mathrm{F}}
\end{array}
\tag{5.3}
$$

The anti-commutator relations for these operators follow directly from (5.1) and the only non-vanishing relations are

$$
\{\hat{i}^\dagger, \hat{j}\} = \delta_{ij} \qquad \{\hat{a}^\dagger, \hat{b}\} = \delta_{ab}.
\tag{5.4}
$$

Inserting the particle/hole operators into (5.2) splits the sum over states p into a sum over holes i and a sum over particles a, giving

$$
\begin{aligned}
\hat{H}_0 &= \sum_i \varepsilon_i \hat{i}\hat{i}^\dagger + \sum_a \varepsilon_a \hat{a}^\dagger \hat{a} \\
&= \underbrace{\sum_i \varepsilon_i}_{=E_0} - \sum_i \varepsilon_i \hat{i}^\dagger \hat{i} + \sum_a \varepsilon_a \hat{a}^\dagger \hat{a},
\end{aligned}
\tag{5.5}
$$

where we have used the anti-commutator relation to put the operators into normal order, such that all annihilation operators appear on the right.

Next, we need to translate the perturbation $\hat{H}_1$ into the particle/hole formalism. We start with its second quantized representation using the electron creation and annihilation operators $\hat{c}_p^\dagger$ and $\hat{c}_p$:

$$
\hat{H}_1 = \frac{1}{2} \sum_{pqrs} V_{sr}^{pq} \hat{c}_p^\dagger \hat{c}_q^\dagger \hat{c}_r \hat{c}_s - \sum_{pq} v_q^p \hat{c}_p^\dagger \hat{c}_q,
\tag{5.6}
$$

where V_{sr}^{pq} and v_q^p are the matrix elements of the first quantized operators $\hat{V}_{\mathrm{ee}}$ and $\hat{V}_{\mathrm{eff}}$, given by

$$
V_{sr}^{pq} = \langle pq|\hat{V}_{\mathrm{ee}}|sr\rangle = \iint \mathrm{d}\mathbf{x}\,\mathrm{d}\mathbf{x}'\, \psi_p^*(\mathbf{x})\psi_q^*(\mathbf{x}') \frac{1}{|\mathbf{r}-\mathbf{r}'|} \psi_r(\mathbf{x}')\psi_s(\mathbf{x})
\tag{5.7}
$$

$$
v_q^p = \langle p|\hat{V}_{\mathrm{eff}}|q\rangle = \int \mathrm{d}\mathbf{x}\, \psi_p^*(\mathbf{x}) \left(\hat{V}_{\mathrm{eff}}\psi_q\right)(\mathbf{x}),
\tag{5.8}
$$

with $\int \mathrm{d}\mathbf{x} = \sum_\alpha \int \mathrm{d}\mathbf{r}$. The factor $\frac{1}{2}$ in (5.6) accounts for double counting when not restricting the sum over p, q, r and s to distinct elements of V_{sr}^{pq}.

Unfortunately, it is not as straight forward to translate $\hat{H}_1$ into the particle/hole picture as it was for $\hat{H}_0$ since there are now up to 4 different indices which can be either holes or particles. If, for example, p, q, r are particle indices a, c, b and s is a hole index i, $\hat{V}_{\mathrm{ee}}$ creates the particles a, c and the hole i while it destroys the particle b, as shown in Figure 5.1. The electron creation and annihilation operators $\hat{c}^\dagger$ and $\hat{c}$ always occur in pairs thus keeping the number of electrons constant. However, particle and hole creation and annihilation operators are in general not normal ordered and occur in any constellation. The number of particles and holes is therefore not necessarily constant. Figure 5.1 also shows a particle/hole pair created by the action of $\hat{V}_{\mathrm{eff}}$ indicated by a shaded circle.

$$V_{ib}^{ac}\hat{c}_a^\dagger\hat{c}_c^\dagger\hat{c}_b\hat{c}_i = V_{ib}^{ac}\hat{a}^\dagger\hat{c}^\dagger\hat{b}\hat{i}^\dagger =$$

$$v_i^a\hat{c}_a^\dagger\hat{c}_i = v_i^a\hat{a}^\dagger\hat{i}^\dagger =$$

Figure 5.1: Examples of terms occurring in $\hat{H}_1$ and their respective diagrammatic representation

5.1.2 Interaction picture

So far, all operators were given in the Schrödinger picture, where all time evolution takes place in the states ψ_p and the operators are time independent. The Heisenberg picture, on the other hand, keeps the states time independent and all time evolution is put into the operators. In order to do time dependent perturbation theory, it is convenient to use the interaction picture, which is a hybrid of the Schrödinger and the Heisenberg picture. In the interaction picture the operators evolve according to a time evolution solely based on the unperturbed part of the Hamiltonian $\hat{H}_0$, while the states evolve only due to the action of the perturbation $\hat{H}_1$.

Given a state in the Schrödinger picture $|\Psi(t)\rangle$ we define the corresponding state in the interaction picture $|\Psi_I(t)\rangle$ by "undoing" the time evolution which originates from $\hat{H}_0$:

$$|\Psi_I(t)\rangle = e^{i\hat{H}_0 t}|\Psi(t)\rangle. \tag{5.9}$$

To find the equation of motion for states in the interaction picture we derive with respect to time, giving

$$
\begin{aligned}
i\frac{\partial}{\partial t}|\Psi_I(t)\rangle &= -\hat{H}_0 e^{i\hat{H}_0 t}|\Psi(t)\rangle + e^{i\hat{H}_0 t}i\frac{\partial}{\partial t}|\Psi(t)\rangle \\
&= -e^{i\hat{H}_0 t}\hat{H}_0|\Psi(t)\rangle + e^{i\hat{H}_0 t}(\hat{H}_0 + \hat{H}_1)|\Psi(t)\rangle \\
&= \underbrace{e^{i\hat{H}_0 t}\hat{H}_1 e^{-i\hat{H}_0 t}}_{=\hat{H}_{1I}(t)}|\Psi_I(t)\rangle.
\end{aligned}
\tag{5.10}
$$

So the time evolution of $|\Psi_I(t)\rangle$ is determined by the perturbation $\hat{H}_{1I}(t)$ only. The time dependence of $\hat{H}_{1I}(t)$, on the other hand, solely depends on the unperturbed part of the Hamiltonian $\hat{H}_0$. We are now interested in the time evolution operator $\hat{U}_I(t, t_0)$ that evolves a state in the interaction picture from the time t_0 to the time t:

$$\hat{U}_I(t, t_0)|\Psi_I(t_0)\rangle = |\Psi_I(t)\rangle. \tag{5.11}$$

Operating with $i\partial/\partial t$ on both sides and using (5.10) gives

$$i\frac{\partial}{\partial t}\hat{U}_I(t, t_0)|\Psi_I(t_0)\rangle = \hat{H}_{1I}(t)\hat{U}_I(t, t_0)|\Psi_I(t_0)\rangle,$$

which must holds for all $|\Psi_I(t_0)\rangle$ thus leading to the equation of motion for the time evolution operator in the interaction picture

$$i\frac{\partial}{\partial t}\hat{U}_I(t, t_0) = \hat{H}_{1I}(t)\hat{U}_I(t, t_0). \tag{5.12}$$

Integrating both sides of the above equation with respect to the first argument from t_0 to t yields

$$\hat{U}_I(t, t_0) = 1 - \mathrm{i} \int_{t_0}^{t} \mathrm{d}t' \, \hat{H}_{1I}(t') \hat{U}_I(t', t_0), \tag{5.13}$$

where we have used $\hat{U}_I(t_0, t_0) = 1$, which follows from (5.11). This integral equation can be solved by iteratively applying the above equation to each occurrence of $\hat{U}_I(t', t_0), \hat{U}_I(t'', t_0)$ and so forth, giving

$$
\begin{aligned}
\hat{U}_I(t, t_0) &= 1 - \mathrm{i} \int_{t_0}^{t} \mathrm{d}t' \, \hat{H}_{1I}(t') + \mathrm{i}^2 \int_{t_0}^{t} \mathrm{d}t' \int_{t_0}^{t'} \mathrm{d}t'' \, \hat{H}_{1I}(t') \hat{H}_{1I}(t'') - \mathrm{i}^3 \dots \\
&= \sum_{n=0}^{\infty} (-\mathrm{i})^n \int_{t > t_1 > \dots > t_n > t_0} \mathrm{d}t_1 \dots \mathrm{d}t_n \, \hat{H}_{1I}(t_1) \dots \hat{H}_{1I}(t_n).
\end{aligned} \tag{5.14}
$$

This means that the time evolution operator in the interaction picture can be constructed by applying the perturbation $\hat{H}_{1I}$ any number of times and at all possible times between t_0 and t in a time ordered manner. The number of applications of $\hat{H}_{1I}$ is called the *order* in the perturbation expansion. The perturbation expansion for the time evolution operator can be truncated at a finite order. However, the truncated expansion is not guaranteed to converge at any finite order. In metals, for example, no truncation is convergent beyond first order. This is a considerable drawback for finite order perturbation methods, such as second order Møller–Plesset perturbation theory (MP2).

5.2 The Gell-Mann–Low theorem

In the previous section we have seen how to evolve any given state from t_0 to t. We are, however, interested in eigenstates of the full Hamiltonian, most importantly in its ground state $|\Psi\rangle$. All we have are eigenstates of the non-interacting Hamiltonian $\hat{H}_0$ which we can evolve from. In general, such an evolved state $\hat{U}_I(t, t_0) |\Phi(t_0)\rangle$ will be neither an eigenstate of the non-interacting Hamiltonian $\hat{H}_0$ nor of the full Hamiltonian $\hat{H}$. We can, however, introduce a time dependent perturbation

$$\hat{H}(t) = \hat{H}_0 + e^{\eta t} \hat{H}_1 \tag{5.15}$$

for $t \leq 0$, slowly turning on the electron-electron interaction for small $\eta > 0$. The system starts with the unperturbed Hamiltonian $\hat{H}_0$ at $t = -\infty$ and at $t = 0$ the interaction is fully turned on, giving $\hat{H}$. According to the adiabatic theorem, the system will stay in an eigenstate of $\hat{H}(t)$ at all times when starting from an eigenstate of $\hat{H}_0$ at $t = -\infty$ if the transition is sufficiently slow, which holds for

$$\eta \ll \Delta E.$$

ΔE is the energy change of the ground state when turning on the interaction. Note that starting in the ground state of $\hat{H}_0$ at $t = -\infty$ does not guaranteed that the evolved eigenstate at $t = 0$ is indeed the ground state of the full Hamiltonian $\hat{H}$. Level crossings may occur. We will, however, assume that they do not occur for the ground state and that the ground state $|\Phi\rangle$ of $\hat{H}_0$ evolves adiabatically into the ground state $|\Psi\rangle$ of $\hat{H}$:

$$|\Psi\rangle = \hat{U}_\eta(0, -\infty) |\Phi\rangle, \tag{5.16}$$

where we drop the explicit denotation of the interaction picture in favor of denoting the dependence on the parameter η of the transition speed, writing from now on

$$\hat{U}_\eta(t, t_0) = \sum_{n=0}^\infty (-\mathrm{i})^n \int_{t > t_1 > \ldots > t_n > t_0} \mathrm{d}t_1 \ldots \mathrm{d}t_n \, \hat{H}_1(t_1) \ldots \hat{H}_1(t_n) \tag{5.17}$$

and

$$\hat{H}_1(t) = e^{\mathrm{i}\hat{H}_0 t} e^{\eta t} \hat{H}_1 e^{-\mathrm{i}\hat{H}_0 t}. \tag{5.18}$$

Although $\hat{U}_\eta$ and $\hat{H}_1$ depend on η we hope that the results are, in the end, independent of η if it is chosen sufficiently small. The quantity we are now most interested in is the energy difference ΔE between the ground state energy of the non-interacting Hamiltonian $\hat{H}_0$ and the ground state energy of the fully interacting Hamiltonian $\hat{H} = \hat{H}_0 + \hat{H}_1$. The fully interacting ground state $|\Psi\rangle$ satisfies the Schrödinger equation

$$(\hat{H}_0 + \hat{H}_1) |\Psi\rangle = (E_0 + \Delta E) |\Psi\rangle .$$

Multiplying both sides with $\langle\Phi|$ from the left and using (5.16) gives

$$\begin{aligned}
E_0 + \Delta E &= \frac{\langle\Phi|\hat{H}_0|\Psi\rangle}{\langle\Phi|\Psi\rangle} + \frac{\langle\Phi|\hat{H}_1|\Psi\rangle}{\langle\Phi|\Psi\rangle} \\
&= \frac{\langle\Phi|\hat{H}_0\hat{U}_\eta(0, -\infty)|\Phi\rangle}{\langle\Phi|\hat{U}_\eta(0, -\infty)|\Phi\rangle} + \frac{\langle\Phi|\hat{H}_1(0)\hat{U}_\eta(0, -\infty)|\Phi\rangle}{\langle\Phi|\hat{U}_\eta(0, -\infty)|\Phi\rangle}
\end{aligned} \tag{5.19}$$

The last equation now relates the ground state energy of the fully interacting system to vacuum expectation values (VEV) of the non-interacting system in the particle/hole picture, where $|\Phi\rangle$ is the vacuum state without any particle or hole excitations. In principle, these expectation values can be evaluated despite the infinite sums hidden in the time evolution operators $\hat{U}_\eta$.

5.3   Wick's theorem

Equation (5.19) still has two practical drawbacks. First, there is yet no systematic recipe given how to approximate the time evolution operator $\hat{U}_\eta$, consisting of an infinite sum, and second, one still needs to show that ΔE does not depend on the choice of η if it is chosen sufficiently small. We start with the diagrammatic representation of the terms occurring in (5.19), where we need to evaluate terms of the form

$$\langle\Phi|\hat{A}\hat{B}\ldots|\Phi\rangle.$$

$\hat{A}, \hat{B}, \ldots$ are arbitrary creation or annihilation operators. If these operators were normal ordered, such that all annihilation operators are on the right side of all creation operators, its vacuum expectation value (VEV) would simply be 0, given there is at least one creation or annihilation operator. A relation between the VEV of the operators in the order given and the VEV in normal order is therefore desired. Let $N[\hat{A}\hat{B}\ldots]$ denote normal ordering of the operators where in the case of fermions the sign changes for each transposition. For two creation or annihilation operators, there is only one non-trivial case

$$N[\hat{p}\hat{q}^\dagger] = -\hat{q}^\dagger\hat{p},$$

in the other three cases the operators are already in normal order. Since the vacuum expectation value of two operators in normal order is 0, we can rewrite a given VEV of two operators

$$\langle\Phi|\hat{A}\hat{B}|\Phi\rangle = \langle\Phi|\hat{A}\hat{B}|\Phi\rangle - \langle\Phi|N[\hat{A}\hat{B}]|\Phi\rangle = \langle\Phi|\hat{A}\hat{B} - N[\hat{A}\hat{B}]|\Phi\rangle = \langle\Phi|\overset{\sqcap}{\hat{A}\hat{B}}|\Phi\rangle, \qquad (5.20)$$

defining the *contraction* of two operators $\hat{A}$ and $\hat{B}$ by[1]

$$\overset{\sqcap}{\hat{A}\hat{B}} := \hat{A}\hat{B} - N[\hat{A}\hat{B}].$$

This may seem arbitrary but it turns out that the contraction of two operators is simply a number. For two creation or annihilation operators there are four possible contractions

$$\overset{\sqcap}{\hat{p}\hat{q}} = 0 \qquad \overset{\sqcap}{\hat{p}\hat{q}^{\dagger}} = \{\hat{p}, \hat{q}^{\dagger}\} = \delta_{pq} \qquad \overset{\sqcap}{\hat{p}^{\dagger}\hat{q}} = 0 \qquad \overset{\sqcap}{\hat{p}^{\dagger}\hat{q}^{\dagger}} = 0. \qquad (5.21)$$

Since the contraction of two operators is a number it is unaffected by normal ordering. This allows us to make the desired connection between the given order and the normal order of two operators $\hat{A}\hat{B}$:

$$\hat{A}\hat{B} = N[\hat{A}\hat{B}] + \overset{\sqcap}{\hat{A}\hat{B}} = N[\hat{A}\hat{B} + \overset{\sqcap}{\hat{A}\hat{B}}]$$

This result can be generalized to more than two operators by the virtue of Wick's theorem (Wick 1950; Peskin and Schroeder 1995):

$$\hat{A}\hat{B}\hat{C}\ldots = N\left[\hat{A}\hat{B}\hat{C}\ldots + \textit{all possible contractions of } \hat{A}\hat{B}\hat{C}\ldots\right] \qquad (5.22)$$

For a sequence of four operators this gives for instance

$$\begin{aligned}
\hat{A}\hat{B}\hat{C}\hat{D} &= N[\hat{A}\hat{B}\hat{C}\hat{D}] + N[\overset{\sqcap}{\hat{A}\hat{B}}\hat{C}\hat{D}] + N[\hat{A}\overset{\sqcap}{\hat{B}\hat{C}}\hat{D}] + N[\hat{A}\hat{B}\overset{\sqcap}{\hat{C}\hat{D}}] + N[\overset{\sqcap\quad\sqcap}{\hat{A}\hat{B}\hat{C}\hat{D}}] + \\
&\quad N[\hat{A}\overset{\sqcap\quad\sqcap}{\hat{B}\hat{C}\hat{D}}] + N[\overset{\sqcap\quad\sqcap}{\hat{A}\hat{B}\hat{C}\hat{D}}] + N[\hat{A}\overset{\sqcap}{\hat{B}}\overset{\sqcap}{\hat{C}\hat{D}}] + N[\overset{\sqcap\sqcap}{\hat{A}\hat{B}\hat{C}\hat{D}}] + N[\overset{\sqcap\;\sqcap}{\hat{A}\hat{B}\hat{C}\hat{D}}], \quad (5.23)
\end{aligned}$$

where we can now reorder the operators, changing the sign appropriately, to pull contracted operators out of the normal ordering operator. For example

$$N[\overset{\sqcap\quad\sqcap}{\hat{A}\hat{B}\hat{C}\hat{D}}] = -\overset{\sqcap}{\hat{A}\hat{C}} \times N[\hat{B}\hat{D}].$$

Since vacuum expectation values of normal ordered operators vanish, only the fully contracted terms survive. The VEV of the four operators in (5.23) thus evaluates to

$$\langle\Phi|\hat{A}\hat{B}\hat{C}\hat{D}|\Phi\rangle = \overset{\sqcap\quad\sqcap}{\hat{A}\hat{B}\hat{C}\hat{D}} - \overset{\sqcap\quad\sqcap}{\hat{A}\hat{C}\hat{B}\hat{D}} + \overset{\sqcap\quad\sqcap}{\hat{A}\hat{D}\hat{B}\hat{C}}. \qquad (5.24)$$

---

[1]Note that contractions are usually defined by $\overset{\sqcap}{\hat{A}\hat{B}} = T[\hat{A}\hat{B}] - N[\hat{A}\hat{B}]$, where $T[\hat{A}\hat{B}]$ denotes time ordering of the operators, such that the time increases from right to left. In our case, the terms occurring in (5.19) are already time ordered by the constraints of the integrals so we will drop the time ordering symbol.

5.3.1   Application to the perturbation

We can now apply this algebra to a simplified case without an effective interaction where the perturbation is given by

$$\hat{H}_1(t) = e^{\mathrm{i}\hat{H}_0 t} e^{\eta t} \frac{1}{2} \sum_{pqrs} V^{pq}_{sr} \hat{c}^\dagger_p \hat{c}^\dagger_q \hat{c}_r \hat{c}_s e^{-\mathrm{i}\hat{H}_0 t}. \tag{5.25}$$

Note that the electron creation and annihilation operators $\hat{c}^\dagger_p$ and $\hat{c}_p$ have to be expressed in terms of particle and hole creation and annihilation operators $\hat{p}^\dagger$ and $\hat{p}$, since we want to use the non-interacting ground state $|\Phi\rangle$ as the vacuum state. From (5.3) we get

$$\hat{c}^\dagger_p = \left\{ \begin{array}{ll} \hat{p}^\dagger & \text{for } \varepsilon_p > \varepsilon_\mathrm{F} \\ \hat{p} & \text{otherwise,} \end{array} \right. \qquad \hat{c}_p = \left\{ \begin{array}{ll} \hat{p} & \text{for } \varepsilon_p > \varepsilon_\mathrm{F} \\ \hat{p}^\dagger & \text{otherwise.} \end{array} \right. \tag{5.26}$$

We start with evaluating the numerator of the right term in (5.19) in zeroth order of the expansion of the time evolution operator, where $\hat{U}^{(0)}_\eta(0,-\infty) = 1$:

$$\langle\Phi|\hat{H}_1(0)|\Phi\rangle = \frac{1}{2} \sum_{pqrs} V^{pq}_{sr} \overline{\hat{c}^\dagger_p \hat{c}^\dagger_q} \,\overline{\hat{c}_r \hat{c}_s} + \frac{1}{2} \sum_{pqrs} V^{pq}_{sr} \overline{\hat{c}^\dagger_p \overline{\hat{c}^\dagger_q \hat{c}_r} \hat{c}_s} + \frac{1}{2} \sum_{pqrs} V^{pq}_{sr} \overline{\hat{c}^\dagger_p \overline{\hat{c}^\dagger_q \hat{c}_r} \hat{c}_s} \tag{5.27}$$

According to (5.21) the only non-vanishing contraction comes from operators of the form $\hat{p}\hat{p}^\dagger$, first creating a hole or a particle in the state p and subsequently destroying it. Thus, the first term in (5.27) must vanish. The second and the third term can only survive if p, q, r and s are hole indices i, j, k and l, giving

$$\langle\Phi|\hat{H}_1(0)|\Phi\rangle = \frac{1}{2} \sum_{ijkl} V^{ij}_{lk} \overline{\hat{i}\,\overline{\hat{j}\hat{k}^\dagger}\hat{l}^\dagger} + \frac{1}{2} \sum_{ijkl} V^{ij}_{lk} \overline{\hat{i}\,\overline{\hat{j}\hat{k}^\dagger}\hat{l}^\dagger} = -\frac{1}{2}\sum_{ij} V^{ij}_{ji} + \frac{1}{2}\sum_{ij} V^{ij}_{ij}. \tag{5.28}$$

Note that neither of the two terms individually respects the Pauli exclusion principle. However, the offending terms, where $i = j$, cancel in the sum of all terms. By the merit of Wick's theorem it is no longer necessary to keep track of disallowed states individually. They simply cancel in the sum of all contractions.

Let us now proceed evaluating the numerator of (5.19) in the simplified case of above with the perturbation given by (5.25). The next order in the expansion of the time evolution operator is

$$\hat{U}^{(1)}_\eta(0,-\infty) = -\mathrm{i} \int\limits_{-\infty}^{0} \mathrm{d}t_1 \, \hat{H}_1(t_1).$$

For the application of Wick's theorem at $t \neq 0$ it is more convenient to write the Hamiltonian of the perturbation $\hat{H}_1(t)$ in terms of time dependent creation and annihilation operators. All states in (5.25) appear in both exponents of $\pm\mathrm{i}\hat{H}_0 t$ except for p, q and r, s which can only appear in the left or in the right exponent, respectively. Thus, we get

$$\hat{H}_1(t) = e^{\eta t} \frac{1}{2} \sum_{pqrs} V^{pq}_{sr} \underbrace{\left(\hat{c}^\dagger_p e^{\mathrm{i}\varepsilon_p t}\right)}_{=\hat{c}^\dagger_p(t)} \left(\hat{c}^\dagger_q e^{\mathrm{i}\varepsilon_q t}\right) \left(\hat{c}_r e^{-\mathrm{i}\varepsilon_r t}\right) \underbrace{\left(\hat{c}_s e^{-\mathrm{i}\varepsilon_s t}\right)}_{=\hat{c}_s(t)},$$

which can be used to evaluate the next order: $\langle\Phi|\hat{H}_1(0)\hat{U}_\eta^{(1)}(0,-\infty)|\Phi\rangle$

$$= \left\langle \Phi \left| -\mathrm{i}\int_{-\infty}^0 \mathrm{d}t_1\, e^{\eta t_1}\frac{1}{4}\sum_{pqrstuvw} V_{sr}^{pq}V_{wv}^{tu}\, \hat{c}_p^\dagger\hat{c}_q^\dagger\hat{c}_r\hat{c}_s\hat{c}_t^\dagger(t_1)\hat{c}_u^\dagger(t_1)\hat{c}_v(t_1)\hat{c}_w(t_1) \right| \Phi \right\rangle$$

There are 4 creation and 4 annihilation operators in this expression, thus there are $4! = 24$ non-vanishing ways of contractions possible. We will, for now, just look at the following:

$$-\mathrm{i}\int_{-\infty}^0 \mathrm{d}t_1\, e^{\eta t_1}\frac{1}{4}\sum_{pqrstuvw} V_{sr}^{pq}V_{wv}^{tu}\, \hat{c}_p^\dagger\hat{c}_q^\dagger\hat{c}_r\hat{c}_s\hat{c}_t^\dagger(t_1)\hat{c}_u^\dagger(t_1)\hat{c}_v(t_1)\hat{c}_w(t_1)$$

$$= -\mathrm{i}\int_{-\infty}^0 \mathrm{d}t_1\, e^{\eta t_1}\frac{1}{4}\sum_{pqrstuvw} V_{sr}^{pq}V_{wv}^{tu}\, \hat{c}_p^\dagger\hat{c}_w(t_1)\hat{c}_s\hat{c}_t^\dagger(t_1)\hat{c}_q^\dagger\hat{c}_v(t_1)\hat{c}_r\hat{c}_u^\dagger(t_1)$$

For non-vanishing terms, p, w and q, v must be hole indices i and j, respectively. Similarly, s, t and r, u must be particle indices a and b, giving

$$-\mathrm{i}\int_{-\infty}^0 \mathrm{d}t_1\, e^{\eta t_1}\frac{1}{4}\sum_{ijab} V_{ab}^{ij}V_{ij}^{ab}\, e^{-\mathrm{i}\varepsilon_i t_1}e^{\mathrm{i}\varepsilon_a t_1}e^{-\mathrm{i}\varepsilon_j t_1}e^{\mathrm{i}\varepsilon_b t_1} = \frac{1}{4}\sum_{ijab}\frac{V_{ab}^{ij}V_{ij}^{ab}}{\varepsilon_i+\varepsilon_j-\varepsilon_a-\varepsilon_b+\mathrm{i}\eta}. \tag{5.29}$$

For a system where there exists a finite gap $E_g > 0$ such that $|\varepsilon_i - \varepsilon_a| > E_g$ for all holes i and particles a we can simply choose $\eta \ll E_g$ to get a result independent of the choice of η. For metals with a non-degenerate ground state there is no finite $E_g > 0$ for all i and a, however, $|\varepsilon_i - \varepsilon_a| > 0$. In this case the limit $\eta \to 0$ can only be taken after summing over all states, as done in Section 6.4 for the Uniform Electron Gas. If the ground state is degenerate we have to resort to Degenerate State Perturbation Theory, which is not discussed here.

Wick's theorem provides a systematic way to evaluate the vacuum expectation values occurring in the Gell-Mann–Low theorem (5.19). Instead of keeping track of which states are occupied after each interaction we can simply sum over contractions of the operator matrices V_{sr}^{pq} and v_q^p occurring in the perturbation, as shown in (5.28) and in (5.29). We do, however, have to sum over all possible contractions.

5.4 Goldstone diagrams

The number of possible contractions in Wick's theorem quickly becomes too large to evaluate vacuum expectation values as we did in the previous section. So far, we have used diagrams solely for depicting the action of a second quantized operator where the initial state was shown below and the final state above the operator symbol, as shown in Figure 5.1. It is time to rigorously introduce the diagrammatic notation employed by Goldstone in order to enumerate and evaluate all contractions.

Each Coulomb interaction $\hat{V}_{ee}$ is represented by a horizontal wiggly line between two vertices. Each *vertex* consists of one electron creation operator and one electron annihilation operator represented by an outbound and an inbound *leg*, respectively. Without loss of generality, the outer operators $\hat{c}_p^\dagger$ and $\hat{c}_s$ are associated with the left vertex and the inner operators $\hat{c}_q^\dagger$ and $\hat{c}_r$ with the right vertex. Each effective interaction $\hat{V}_{eff}$ is represented by a vertex in form of a shaded circle. Therefore, lower indices of the matrices V_{sr}^{pq} and v_q^p are from inbound legs, upper indices are from outbound legs and left indices are from left legs.
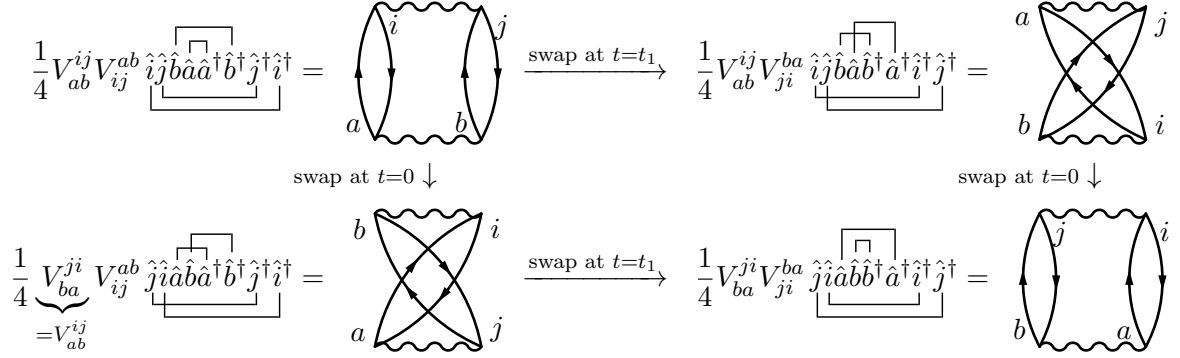
$$V_{sr}^{pq}\hat{c}_p^\dagger\hat{c}_q^\dagger\hat{c}_r\hat{c}_s = \qquad\qquad\qquad v_q^p\hat{c}_p^\dagger\hat{c}_q = $$

Figure 5.2: Representation of the Coulomb and effective interaction in Goldstone diagrams

Connections of these legs represent the contractions, where only outbound legs may be connected to inbound legs, as they are the only non-vanishing operator contractions. The connections are directed from an outbound to an inbound leg, indicated by an arrow. Time propagates from bottom to top and the last Coulomb or effective interaction is usually at $t = 0$. Connections directed forwards in time represent contractions of the form $\hat{c}_p \ldots \hat{c}_q^\dagger$ and are hence restricted to particles. Conversely, connections directed backwards in time are restricted to holes. Connections between legs of the same Coulomb interaction are called *non-propagating* and are also restricted to holes, since they are of the form $\hat{c}_p^\dagger\hat{c}_q^\dagger\hat{c}_r\hat{c}_s$. Each connection is labeled with a unique index, over which to contract, $a, b, c, \ldots$ for particles and $i, j, k, \ldots$ for holes.

$$\frac{1}{2}\sum_{ij} V_{ji}^{ij}\hat{i}\hat{j}\hat{i}^\dagger\hat{j}^\dagger = \qquad\qquad \frac{1}{2}\sum_{ij} V_{ij}^{ij}\hat{i}\hat{j}\hat{j}^\dagger\hat{i}^\dagger = i \qquad j$$

Figure 5.3: Goldstone diagrams for the terms of (5.28) with non-propagating connections

5.4.1   Symmetries

Interchanging the left and the right side of a Coulomb interaction including all its connections in the Goldstone diagram leaves the the respective matrix elements V_{sr}^{pq} invariant. In general, however, we get a different contraction from the swapped connections. Since we have to sum over all possible contractions, both contributions have to be counted if they are distinct. Figure 5.4 shows all possible left/right interchanges for the diagram representing the contraction evaluted in (5.29). For the sake of simplicity the time arguments of the operators are omitted. The two cases on the left hand side have distinct contractions, so both must be counted. Both evaluate to the same number since they can be transformed into each other with an even number of operator transpositions and $V_{sr}^{pq} = V_{rs}^{qp}$. We can do that with every Coulomb interaction and from now on identify one Goldstone diagram with all contractions that arise from interchanging the left and the right side of all its Coulomb interactions. In general, this cancels the factor $\frac{1}{2}$ in all Coulomb operators for evaluating one Goldstone diagram as opposed to evaluating one single contraction, where this factor is needed according to (5.7).

If there is however a global left/right symmetry in the Goldstone diagram, interchanging all Coulomb interactions simultaneously does not give a distinct contraction. It merely interchanges the names of the indices over which to contract, as shown in the right two cases of Figure 5.4. Thus, for a Goldstone diagram with a global left/right symmetry only half of the cases arising from interchanging each Coulomb interaction are distinct, which gives rise to a factor of $\frac{1}{2}$ for the whole diagram.

$$\frac{1}{4} V_{ab}^{ij} V_{ij}^{ab}\, \hat{i}\hat{j}\hat{b}\hat{a}\hat{a}^\dagger \hat{b}^\dagger \hat{j}^\dagger \hat{i}^\dagger = \qquad \xrightarrow{\text{swap at } t=t_1} \qquad \frac{1}{4} V_{ab}^{ij} V_{ji}^{ba}\, \hat{i}\hat{j}\hat{b}\hat{a}\hat{b}^\dagger \hat{a}^\dagger \hat{i}^\dagger \hat{j}^\dagger =$$

swap at $t=0 \downarrow$ $\qquad\qquad\qquad\qquad\qquad$ swap at $t=0 \downarrow$

$$\frac{1}{4} \underbrace{V_{ba}^{ji}}_{=V_{ab}^{ij}} V_{ij}^{ab}\, \hat{j}\hat{i}\hat{a}\hat{b}\hat{a}^\dagger \hat{b}^\dagger \hat{j}^\dagger \hat{i}^\dagger = \qquad \xrightarrow{\text{swap at } t=t_1} \qquad \frac{1}{4} V_{ba}^{ji} V_{ji}^{ba}\, \hat{j}\hat{i}\hat{a}\hat{b}\hat{b}^\dagger \hat{a}^\dagger \hat{i}^\dagger \hat{j}^\dagger =$$

Figure 5.4: All possible left/right interchanges of Coulomb interactions for the diagram representing the contraction evaluated in (5.29). The sums and the time arguments of the operators are omitted.

5.4.2 Time integration

The number of interactions occurring in the diagram is called its *order*, which is $n+1$, where n is the order of the expansion of the time evolution operator $\hat{U}_\eta$ in (5.17). According to the expansion of $\hat{U}_\eta$, we must integrate over all times $t_1, \ldots, t_n$ of all interactions except the last one, respecting the order $0 > t_1 > \ldots > t_n$. We can make the substitutions $t_{01} = 0 - t_1, \ldots, t_{n-1n} = t_{n-1} - t_n$ to integrate over the times between each interaction $t_{01}, t_{12}, \ldots, t_{n-1n}$. For a particle state a propagating from an interaction at the time t_n to the time $t = 0$ this gives for instance

$$(-\mathrm{i})^n \int\limits_{0>t_1>\ldots>t_n} \hat{a} e^{-\mathrm{i}\varepsilon_a 0} \ldots e^{\eta t_1} \ldots e^{\eta t_n} \hat{a}^\dagger e^{\mathrm{i}\varepsilon_a t_n} \ldots =$$

$$(-\mathrm{i})^n \int\limits_0^\infty \mathrm{d}t_{01}\, e^{-\mathrm{i}(\varepsilon_a + \ldots - n\mathrm{i}\eta)t_{01}} \int\limits_0^\infty \mathrm{d}t_{12}\, e^{-\mathrm{i}(\varepsilon_a + \ldots - (n-1)\mathrm{i}\eta)t_{12}} \ldots \int\limits_0^\infty \mathrm{d}t_{n-1n}\, e^{-\mathrm{i}(\varepsilon_a + \ldots - \mathrm{i}\eta)t_{n-1n}}$$

$$\ldots \hat{a} \ldots \hat{a}^\dagger \ldots \quad (5.30)$$

So the eigenenergy ε_a appears in the exponential of each time interval where the state propagates. For hole states i the sign is inverted. Integrating out all time intervals gives an energy denominator for each interval between two interactions of the form

$$\frac{1}{\sum\limits_{i\in H_k} \varepsilon_i - \sum\limits_{a\in P_k} \varepsilon_a + k\mathrm{i}\eta},$$

where H_k and P_k are the sets of the holes and particles propagating in the respective k-th time interval. k is counted from the bottom. Figure 5.5 shows an example with two holes and two particles.

For finite orders n of the diagrams and systems with a finite energy gap E_g one can choose $n\eta \ll E_g$ to retrieve results independent of η. When going to infinite orders in the diagrams, as it is done in the Random Phase Approximation, one has to care of the limit of $\eta \to 0$.

$$\frac{1}{2}\sum_{ijab}\frac{V_{ab}^{ij}V_{ij}^{ab}}{\varepsilon_i+\varepsilon_j-\varepsilon_a-\varepsilon_b+\mathrm{i}\eta}= \qquad H=\{i,j\},P=\{a,b\}$$

Figure 5.5: Evaluation of all contractions represented by the given Goldstone diagram. There is one time interval where the holes i,j and the particles a,b are propagating. The symmetry factor is $\frac{1}{2}$.

5.4.3 Fermion sign

Finally, we need a rule to determine the sign of all contractions arising from one Goldstone diagram in a graphical way. The sign of a contraction depends on whether an even or an odd number P of transpositions is required to reorder the contractions in pairs:

$$\hat{A}\hat{B}\hat{C}\ldots\hat{Z}=(-1)^P\hat{A}\hat{C}\hat{B}\hat{Z}\ldots$$

Note that contracted operators must not be swapped since that turns a particle connection into a hole connection or vice versa, representing a different diagram. In the upper example, the following reordering is therefore not allowed: $\hat{A}\hat{C}\hat{Z}\hat{B}\ldots$ In Goldstone diagrams the contracted operators are the operators occurring in the perturbation. They are of the general form

$$\ldots V_{sr}^{pq}\hat{c}_p^\dagger\hat{c}_q^\dagger\hat{c}_r\hat{c}_s\ldots v_{q'}^{p'}\hat{c}_{p'}^\dagger\hat{c}_{q'}\ldots$$

omiting the sums for brevity. Their respective time arguments can be integrated out according to the last section, the order of the interactions from right to left is, however, still relevant.

To determine the sign of all contractions of one Goldstone diagram, we first reorder the operators such that operators of the same vertex of an interaction are grouped together:

$$\ldots V_{sr}^{pq}\underbrace{\hat{c}_p^\dagger\hat{c}_s}_{\text{vertex}}\hat{c}_q^\dagger\hat{c}_r\ldots v_{q'}^{p'}\hat{c}_{p'}^\dagger\hat{c}_{q'}\ldots$$

This only affects the Coulomb interactions and involves an even number of transpositions leaving the sign invariant. The matrix elements V_{sr}^{pq} and v_q^p are complex numbers. Their order is therefore irrelevant and we will omit them here.

The finite set of vertices and connections form a directed graph, where each vertex has exactly one outgoing and one incoming connection. Thus, the graph consists of disconnected loops of vertices allowing us to group the vertices of each loop together as long as we do not change the order of the vertices within each loop. The sign will not be affected since we only move vertices. For the diagram in Figure 5.5 this gives for instance

$$\hat{i}\hat{a}\hat{j}\hat{b}\hat{a}^\dagger\hat{i}^\dagger\hat{b}^\dagger\hat{j}^\dagger=(+1)\,\hat{i}\hat{a}\hat{a}^\dagger\hat{i}^\dagger\hat{j}\hat{b}\hat{b}^\dagger\hat{j}^\dagger. \tag{5.31}$$

The symmetry of the Coulomb interaction allows us to freely move the vertices horizontally such that each loop forms a simple polygon where the connections do not intersect each other.

Without loss of generality, we choose a clockwise orientation of the directed connections in order to resemble the order of the creation operators in a vertex of the form $\hat{a}^\dagger \hat{i}^\dagger$ as shown in Figure 5.6.
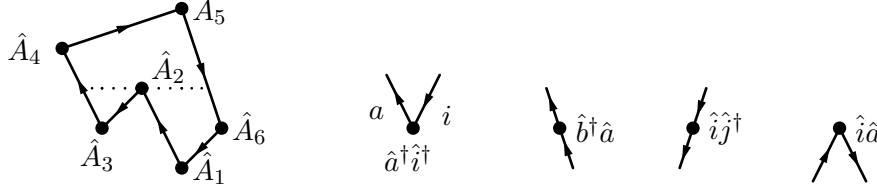

Figure 5.6: A closed loop of vertices $\hat{A}_1, \ldots, \hat{A}_6$, where each vertex operator $\hat{A}$ is of one of the four possible forms shown.

Simple polygons can be decomposed into truncated monotone polygons (Preparata and Shamos 2008). In a monotone polygon a horizontal line intersects the edges at most twice, such that its left side consists only of particle connections and its right side only of hole connections. In the loop in Figure 5.6 there are two monotone polygons starting at the vertices $\hat{A}_1$ and $\hat{A}_3$. After merging a particle and a hole connection from two different monotone polygons at vertex $\hat{A}_2$ the rest of the polygon above the dotted line is also monotone ending at vertex $\hat{A}_5$.

We have already reordered the operators to group vertices and loops together, as shown in (5.31). As a last preparatory step we will group vertices of monotone polygons together, keeping the time order within each monotone polygon. For the loop in Figure 5.6 this rearrangement from the initial time order in the gives

$$\hat{A}_5 \hat{A}_4 \hat{A}_2 \hat{A}_6 \hat{A}_3 \hat{A}_1 = (+1) \, \hat{A}_5 \hat{A}_4 \hat{A}_2 (\hat{A}_3)(\hat{A}_6 \hat{A}_1),$$

where the operators in the left and in the right parenthesis respectively belong to the left and right monotone polygon below the dotted line.

With the operators ordered this way it is now sufficient to treat monotone polygons only. We will follow the vertices within a monotone polygon starting with a vertex of the form $\hat{a}^\dagger \hat{i}^\dagger$. Then, vertices of the form $\hat{b}^\dagger \hat{a}$ add particle connections on the left side of the monotone polygon under consideration while vertices of the form $\hat{j} \hat{i}^\dagger$ add hole connections on the right side. A vertex of the form $\hat{i} \hat{a}$ can either join two different monotone polygons, as $\hat{A}_2$ does in Figure 5.6, or it can close the loop. At each vertex we reorder the involved contractions into the general form

$$\overbrace{\hat{i}\hat{a}....\hat{a}^\dagger \hat{i}^\dagger} \hat{P} \qquad a \diagdown\!\!\!\diagup i \atop \bigcirc \hat{P} \tag{5.32}$$

such that $\hat{P}$ consists only of contracted pairs $\hat{b}\hat{b}^\dagger \hat{j}\hat{j}^\dagger \ldots$ and the creation operators $\hat{a}^\dagger \hat{i}^\dagger$ of the open particle and hole connections are to the left of $\hat{P}$. All operators to the right of $\hat{a}^\dagger \hat{i}^\dagger$ are then in the desired order, denoted here by a circle in the diagram. Note that the order of the creation operators $\hat{a}^\dagger \hat{i}^\dagger$ is relevant and the particle creation operator must stand to the left of the hole creation operator.

A monotone polygon starts with a vertex of the form $\hat{a}^\dagger \hat{i}^\dagger$. This is trivially in the above form

$$a \diagdown\!\!\!\diagup i \qquad \overbrace{\hat{i}\hat{a}....\hat{a}^\dagger \hat{i}^\dagger} = (+1) \overbrace{\hat{i}\hat{a}....\hat{a}^\dagger \hat{i}^\dagger} \underbrace{1}_{\hat{P}} \qquad a \diagdown\!\!\!\diagup i \atop \bigcirc \hat{P} \tag{5.33}$$

with no change of sign. A vertex of the form $\hat{b}^\dagger\hat{a}$ adds a particle connection on the left side of the polygon. Using two transpositions we can bring the operators into the desired form

$$\hat{i}\hat{b}....\hat{b}^\dagger\hat{a}\hat{a}^\dagger\hat{i}^\dagger\hat{P} = (+1)\, \hat{i}\hat{b}....\hat{b}^\dagger\hat{i}^\dagger\underbrace{\hat{a}\hat{a}^\dagger\hat{P}}_{\hat{P}'} \tag{5.34}$$

such that $\hat{a}\hat{a}^\dagger$ can be absorbed into the set of paired operators $\hat{P}'$ to continue with. The sign does not change in this case. A vertex of the form $\hat{i}\hat{j}^\dagger$ adds a hole connection on the right side of the polygon. Now, three transpositions are required to bring the operators into the form

$$\hat{j}\hat{a}....\hat{i}\hat{j}^\dagger\hat{a}^\dagger\hat{i}^\dagger\hat{P} = (-1)\, \hat{j}\hat{a}....\hat{a}^\dagger\hat{j}^\dagger\underbrace{\hat{i}\hat{i}^\dagger\hat{P}}_{\hat{P}'} \tag{5.35}$$

to absorb $\hat{i}\hat{i}^\dagger$ into $\hat{P}'$ and to bring the hole creation operator $\hat{j}^\dagger$ of the open connection to the right side of the particle creation operator $\hat{a}^\dagger$, as required by (5.32). In this case the sign changes.

At a vertex of the form $\hat{j}\hat{a}$ two different monotone polygons can be joined to a polygon that is monotone after this vertex. We assume that the right monotone polygon starts earlier in time, such that all its operators $\hat{a}^\dagger\hat{i}^\dagger\hat{P}$ are to the right of all operators of the left monotone polygon $\hat{b}^\dagger\hat{j}^\dagger\hat{Q}$. The converse case can be treated analogously. Bringing the operators into the desired form

$$\hat{i}\hat{b}....\hat{j}\hat{a}\hat{b}^\dagger\hat{j}^\dagger\hat{Q}\hat{a}^\dagger\hat{i}^\dagger\hat{P} = (-1)\, \hat{i}\hat{b}....\hat{b}^\dagger\hat{i}^\dagger\underbrace{\hat{j}\hat{j}^\dagger\hat{Q}\hat{a}\hat{a}^\dagger\hat{P}}_{\hat{P}'} \tag{5.36}$$

requires an odd number of transpositions and changes the sign. The last vertex of a loop is of the form $\hat{i}\hat{a}$. It closes the monotone polygon without change of sign

$$\hat{i}\hat{a}\hat{a}^\dagger\hat{i}^\dagger\hat{P} = (+1)\, \underbrace{\hat{a}\hat{a}^\dagger\hat{i}\hat{i}^\dagger\hat{P}}_{\hat{P}'}. \tag{5.37}$$

In summary, the sign changes when a contraction of hole operators $\hat{i}\hat{i}^\dagger$ is absorbed into the set of paired operators $\hat{P}'$, as in (5.35) and (5.36). When closing the loop in (5.37) there is however no change of sign although there is a pair of hole operators absorbed in $\hat{P}'$. The Fermion sign of a single loop is therefore $(-1)^{h-1} = (-1)(-1)^h$, where h is the number of hole connections in the loop. For a Goldstone diagram consisting of l loops and h hole connections in total the Fermion sign is thus

$$(-1)^{l+h}, \tag{5.38}$$

which can easily be determined graphically. Note that non-propagating connections, as shown in Figure 5.3 also count as holes.

5.5 The Linked-Cluster theorem

We can now employ the framework of Goldstone diagrams to systematically evaluate the terms of the Gell-Mann–Low theorem (5.19):

$$E_0 + \Delta E = \frac{\langle \Phi | \hat{H}_0 \hat{U}_\eta(0, -\infty) | \Phi \rangle}{\langle \Phi | \hat{U}_\eta(0, -\infty) | \Phi \rangle} + \frac{\langle \Phi | \hat{H}_1(0) \hat{U}_\eta(0, -\infty) | \Phi \rangle}{\langle \Phi | \hat{U}_\eta(0, -\infty) | \Phi \rangle}$$

Only fully contracted operators contribute to the vacuum expectation values which requires that all occurring diagrams are closed with no dangling connection left. In Figure 5.3 and 5.5 we have already evaluated selected diagrams of the numerator containing the final interaction $\hat{H}_1(0)$. Diagrams that are connected to the final interaction at $t = 0$ are called *connected* or, historically, *linked* diagrams. In second order there are already disconnected diagrams, such as

$$\hat{H}_1(0)\ \text{⦵⟿◯} \\ = \quad -\mathrm{i}\int_{-\infty}^{0}\mathrm{d}t_1 \sum_{ijkl} V_{ij}^{ij}\,\hat{i}\hat{j}\hat{j}^{\dagger}\hat{i}^{\dagger}\,e^{\eta t_1}\,V_{kl}^{kl}\,\hat{k}\hat{l}\hat{l}^{\dagger}\hat{k}^{\dagger} = \left(\sum_{ij} V_{ij}^{ij}\right)\left(\sum_{ij}\frac{V_{ij}^{ij}}{\mathrm{i}\eta}\right), \\ \hat{H}_1(t_1)\ \text{⦵⟿◯}$$

where the lower diagram is disconnected. Since there are no contractions between disconnected diagrams their vacuum expectation value decomposes into factors which can be evaluated independently. Note that each disconnected diagram comes with an additional factor of $1/\mathrm{i}\eta$ which diverges in the limit of $\eta \to 0$. In general, we get the following form for the numerator of the Gell-Mann–Low energy expression containing the final interaction:

$$\langle \Phi | \hat{H}_1(0) \hat{U}_\eta(0, -\infty) | \Phi \rangle = \left(\sum \textit{connected diagrams}\right)\left(\sum \textit{disconnected diagrams}\right).$$

Let us now look at the denominator $\langle \Phi | \hat{U}_\eta(0, -\infty) | \Phi \rangle$, where there is no operator at $t = 0$. Since the diagrams must be closed we simply get the same diagrams as the disconnected diagrams in the previous case, as for instance in

$$t = 0\ \cdots\cdots \\ = \quad \left(\sum_{ij}\frac{V_{ij}^{ij}}{\mathrm{i}\eta}\right). \\ \hat{H}_1(t_1)\ \text{⦵⟿◯}$$

Thus, the denominator has the following general form

$$\langle \Phi | \hat{U}_\eta(0, -\infty) | \Phi \rangle = \left(\sum \text{disconnected diagrams}\right).$$

Finally, we need to evaluate the numerator containing $\hat{H}_0$, which is by construction diagonal and from (5.5) given by $\hat{H}_0 = E_0 - \sum_i \varepsilon_i \hat{i}^{\dagger}\hat{i} + \sum_a \varepsilon_a \hat{a}^{\dagger}\hat{a}$. Therefore, all diagrams from $\hat{U}_\eta$ must already be closed at $t = 0$ for non-vanishing contributions, just like in the denominator. In general we get

$$\langle \Phi | \hat{H}_0 \hat{U}_\eta(0, -\infty) | \Phi \rangle = E_0 \left(\sum \textit{disconnected diagrams}\right).$$

Thus, all disconnected diagrams, containing diverging factors $1/\mathrm{i}\eta$, cancel and we finally arrive at the expression for the correlation energy in many-body perturbation theory

$$\Delta E = \left(\sum \textit{connected diagrams}\right).$$

5.6   Hartree-Fock reference

For the sake of simplicity we have not yet taken the effective interaction $\hat{V}_{\text{eff}}$ into consideration although it is an integral part of the perturbation $\hat{H}_1$. Including the effective interaction in first order gives just one additional diagram leading to three non-vanishing contributions:

$$+ \;\; \text{⊙⌇⊙} \qquad\qquad + \;\; \text{⌇} \qquad\qquad - \;\; \text{⊛} \tag{5.39}$$

The perturbation $\hat{H}_1$ contains $\hat{V}_{\text{eff}}$ with a negative sign which has to be taken into account additionally to the sign of the Goldstone diagram originating from the number its loops and holes. The former is explicitly given here, the latter not.

For a Hartree-Fock Hamiltonian $\hat{H}_0$, $\hat{V}_{\text{eff}}$ can be explicitly given

$$v_q^p \hat{c}_p^\dagger \hat{c}_q \;=\; \sum_i V_{qi}^{pi} \hat{c}_p^\dagger \hat{c}_q - \sum_i V_{qi}^{ip} \hat{c}_p^\dagger \hat{c}_q,$$

or in diagrams:

$$\tag{5.40}$$

We can insert (5.40) into (5.39) giving

$$\text{⊙⌇⊙} \;+\; \text{⌇} \;-\; \text{⊙⌇⊙} \;-\; \text{⌇} \;=\; 0.$$

In the case of the Hartree-Fock reference it turns out that the effective interaction contained in the perturbation exactly cancels with all Coulomb interactions containing non-propagating connections. This greatly simplifies the set of Goldstone diagrams to consider. In second order there are already 11 connected Goldstone diagrams, which are shown in Figure 5.7, and only two of them do not cancel in Hartree-Fock. Finite order many-body perturbation theory based on Hartree-Fock is referred to as Møller–Plesset perturbation theory: MP2, MP3 or MP4. The maximum order is given as suffix and rarely exceeds four. Møller–Plesset perturbation theory was developed by (Møller and Plesset 1934) well before Goldstone introduced the diagrammatic treatment of perturbation theory discussed here.

For a non-Hartree-Fock reference, such as Density Functional Theory, one must take all diagrams into consideration that contain either the effective interaction or non-propagating connections. There are nine such diagrams in second order, shown on the left in Figure 5.7. In case of Density Functional Theory, where the effective interaction consists of the Hartree contribution and an exchange-correlation interaction

$$\hat{V}_{\text{xc}}$$

all diagrams containing the Hartree contribution cancel. This leaves only 4 of the 9 additional diagrams and they are to be evaluated with $\hat{V}_{\text{xc}}$ instead of $\hat{V}_{\text{eff}}$. Note that these diagrams are convergent in second order even for metals, offering an alternative to renormalization as done for instance by (Ren et al. 2013). Unless explicitly stated, the diagrams containing the effective or the exchange-correlation interaction are only taken into account to first order according to (5.39) computing the Hartree-Fock interaction energy with the DFT orbitals.
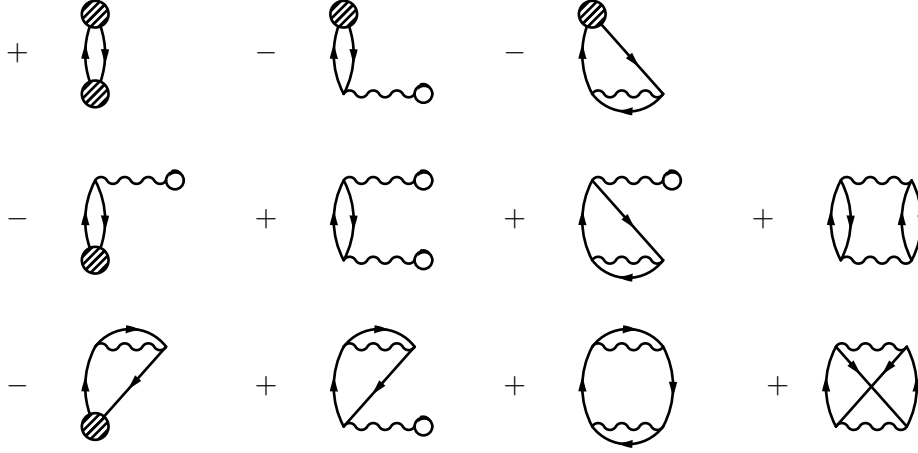
Figure 5.7: All connected Goldstone diagrams of second order. In a Hartree-Fock reference the left three columns cancel leaving only the two contributions of second order Møller–Plesset perturbation theory (MP2).

5.7 Propagators

In the current approach to many-body perturbation theory we use the matrix elements V_{sr}^{pq} and v_q^p from the second quantized representation of the interactions present in the perturbation $\hat{H}_1$. However, storing the Coulomb integrals V_{sr}^{pq} on the computer requires a large amount of memory scaling like $\mathcal{O}(N^4)$ with the size of the system since this matrix has four indices. It is also time consuming to calculate all elements of V_{sr}^{pq} scaling like $\mathcal{O}(N^5)$ with system size. V_{sr}^{pq} must be computed before we can even begin to evaluate any of its contractions for the diagrams in the perturbation expansion.

It can be beneficial to defer the calculation of the Coulomb integrals to a later stage, especially for diagrams where the sums of the Coulomb integrals can be factored into independent contributions, such as in the Hartree term

$$\text{\raisebox{-0.5ex}{\includegraphics{}}} \;=\; \frac{1}{2}\sum_{ij} V_{ij}^{ij} = \frac{1}{2}\sum_{ij} \iint \mathrm{d}\mathbf{x}_1 \mathrm{d}\mathbf{x}_2 \, \psi_i^*(\mathbf{x}_1)\psi_j^*(\mathbf{x}_2)\frac{1}{|\mathbf{r}_1 - \mathbf{r}_2|}\psi_j(\mathbf{x}_2)\psi_i(\mathbf{x}_1)$$

$$= \frac{1}{2}\iint \mathrm{d}\mathbf{x}_1 \mathrm{d}\mathbf{x}_2 \left(\sum_i \psi_i^*(\mathbf{x}_1)\psi_i(\mathbf{x}_1)\right)\frac{1}{|\mathbf{r}_1 - \mathbf{r}_2|}\left(\sum_i \psi_i^*(\mathbf{x}_2)\psi_i(\mathbf{x}_2)\right)$$

which can even be computed in $\mathcal{O}(N^2)$. We can rewrite the above expression to

$$\frac{1}{2}\iint \mathrm{d}\mathbf{x}_1 \mathrm{d}\mathbf{x}_2 \, G_0(\mathbf{x}_1 0, \mathbf{x}_1 0)\frac{1}{|\mathbf{r}_1 - \mathbf{r}_2|}G_0(\mathbf{x}_2 0, \mathbf{x}_2 0)\,,$$

defining the complex valued *propagator* or *Green's function* from the spin-position $\mathbf{x}'$ to the spin-position $\mathbf{x}$ at the same instance in time t

$$G_0(\mathbf{x}t, \mathbf{x}'t) := -\sum_i \psi_i(\mathbf{x})\psi_i^*(\mathbf{x}')\,. \tag{5.41}$$

Note that the sign in the non-propagating case for equal times is negative in accordance with the Fermion sign rules discussed in Subsection 5.4.3.

For propagating states we can use the time dependent creation and annihilation operators to express contractions over V_{sr}^{pq} and v_q^p in terms of complex valued functions of two spin, space and time coordinates. In case of the direct MP2 diagram this gives

$$
\begin{aligned}
\text{[diagram]} \;=\;& \frac{1}{2}(-\mathrm{i})\int_{-\infty}^0 \mathrm{d}t\, e^{\eta t}\sum_{ijab} V_{ij}^{ab}V_{ab}^{ij} \\
=\;& \frac{1}{2}(-\mathrm{i})\int_{-\infty}^0 \mathrm{d}t\, e^{\eta t}\iiiint \mathrm{d}\mathbf{x}_1\,\mathrm{d}\mathbf{x}_2\,\mathrm{d}\mathbf{x}_3\,\mathrm{d}\mathbf{x}_4\,\frac{1}{|\mathbf{r}_1-\mathbf{r}_3|}\,\frac{1}{|\mathbf{r}_2-\mathbf{r}_4|} \\
& \sum_i \psi_i^*(\mathbf{x}_1)\psi_i(\mathbf{x}_3)e^{-\mathrm{i}\varepsilon_i t}\sum_a \psi_a(\mathbf{x}_1)\psi_a^*(\mathbf{x}_3)e^{\mathrm{i}\varepsilon_a t} \\
& \sum_j \psi_j^*(\mathbf{x}_2)\psi_j(\mathbf{x}_4)e^{-\mathrm{i}\varepsilon_j t}\sum_b \psi_b(\mathbf{x}_2)\psi_b^*(\mathbf{x}_4)e^{\mathrm{i}\varepsilon_b t}\,.
\end{aligned}
$$

According to the Linked-Cluster theorem we can choose η arbitrarily small since the terms diverging with $\eta \to 0$ cancel. Therefore, the adiabatic switching function $e^{\eta t}$ has no physical effect and rather serves to make the integrals convergent in the considered interval. Thus, we can as well absorb the switching function into the time dependent creation and annihilation operators. We get

$$
\begin{aligned}
\text{[diagram]} \;=\;& \frac{1}{2}(-\mathrm{i})\int_{-\infty}^0 \mathrm{d}t\iiiint \mathrm{d}\mathbf{x}_1\,\mathrm{d}\mathbf{x}_2\,\mathrm{d}\mathbf{x}_3\,\mathrm{d}\mathbf{x}_4\,\frac{1}{|\mathbf{r}_1-\mathbf{r}_3|}\,\frac{1}{|\mathbf{r}_2-\mathbf{r}_4|} \\
& \sum_i \psi_i^*(\mathbf{x}_1)\psi_i(\mathbf{x}_3)e^{(-\mathrm{i}\varepsilon_i+\eta)t}\sum_a \psi_a(\mathbf{x}_1)\psi_a^*(\mathbf{x}_3)e^{(\mathrm{i}\varepsilon_a+\eta)t} \\
& \underbrace{\sum_j \psi_j^*(\mathbf{x}_2)\psi_j(\mathbf{x}_4)e^{(-\mathrm{i}\varepsilon_j+\eta)t}}_{=-G_0(\mathbf{x}_4 t,\mathbf{x}_2 0)}\underbrace{\sum_b \psi_b(\mathbf{x}_2)\psi_b^*(\mathbf{x}_4)e^{(\mathrm{i}\varepsilon_b+\eta)t}}_{=+G_0(\mathbf{x}_2 0,\mathbf{x}_4 t)}\,,\qquad (5.42)
\end{aligned}
$$

extending the definition of the propagator[2] to all cases:

$$
G_0(\mathbf{x}t,\mathbf{x}'t') := \begin{cases} -\displaystyle\sum_i \psi_i(\mathbf{x})\psi_i^*(\mathbf{x}')e^{(-\mathrm{i}\varepsilon_i+\eta)(t-t')} & \text{for } t \le t' \\ +\displaystyle\sum_a \psi_a(\mathbf{x})\psi_a^*(\mathbf{x}')e^{(-\mathrm{i}\varepsilon_a-\eta)(t-t')} & \text{otherwise.} \end{cases} \qquad (5.43)
$$

In other words, particle states a propagate forwards in time form t' to t, while hole states i propagate backwards in time from t' to t. Note that we have to use hole states i in the non-propagating case, where $t' = t$, to be consistent with definition (5.41). The adiabatic switching function is now part the propagator and its sole purpose is to make positive time intervals convergent for particles and negative time intervals convergent for holes.

---

[2]Note that it is often $\mathrm{i}G_0$ which is defined by the right hand side of (5.43). This factor is normally introduced such that the time evolution of the propagator is compatible to that of the Hamiltonian. We omit this factor here for brevity and in accordance with (Lancaster and Blundell 2014).

5.8 Feynman diagrams

Eventually, it is desirable to have a diagrammatic framework that treats space and time on equal footing. Here, we do not need it for a relativistic treatment of the many-body system, however we want to be able to work in the frequency domain. This requires independent integrals over the whole time domain of the form $\int_{-\infty}^{\infty} dt_1 \ldots \int_{-\infty}^{\infty} dt_n$ rather than the dependent integrals $\int_{0>t_1>\ldots>t_n} dt_1 \ldots dt_n$ we have from the expansion of the time evolution operator $\hat{U}_\eta(0, -\infty)$ according to (5.17):

$$\hat{U}_\eta(t, t_0) = \sum_{n=0}^{\infty} (-i)^n \int_{t>t_1>\ldots>t_n>t_0} dt_1 \ldots dt_n \, \hat{H}_1(t_1) \ldots \hat{H}_1(t_n) \, .$$

Each interaction that comes from the time evolution operator introduces a time variable to integrate over and a factor of $(-i)$. In connected diagrams that applies to all interactions except the last one. We can, however, introduce the same for the last interaction and rewrite (5.42) to

$$(-i) \; \vcenter{\hbox{}} \; = \; \frac{1}{2} \int_{t_1>t_3} dt_1 dt_3 \iiiint d\mathbf{x}_1 \, d\mathbf{x}_2 \, d\mathbf{x}_3 \, d\mathbf{x}_4 \, \delta(t_1) \frac{(-i)}{|\mathbf{r}_1 - \mathbf{r}_2|} \frac{(-i)}{|\mathbf{r}_3 - \mathbf{r}_4|}$$

$$G_0(x_1t_1, x_3t_3) \, G_0(x_3t_3, x_1t_1) \, G_0(x_2t_1, x_4t_3) \, G_0(x_4t_3, x_2t_1)$$

Since the propagators G_0 only depend on time differences we no longer explicitly require the times to be negative and we can integrate over the whole domain instead. However, we still require the times to be ordered and we also need to anchor one of the interaction times for a convergent result. Without loss of generality, we choose to fix the last interaction at $t_1 = 0$ by including $\delta(t_1)$.

In the case of the MP2 direct diagram, we can now simply drop the constraints on the time variables taking double counting into consideration:

$$(-i) \; \vcenter{\hbox{}} \; = \; \frac{1}{4} \iint_{-\infty}^{\infty} dt_1 dt_3 \iiiint d\mathbf{x}_1 \, d\mathbf{x}_2 \, d\mathbf{x}_3 \, d\mathbf{x}_4 \, \delta(t_1) \frac{(-i)}{|\mathbf{r}_1 - \mathbf{r}_2|} \frac{(-i)}{|\mathbf{r}_3 - \mathbf{r}_4|}$$

$$G_0(x_1t_1, x_3t_3) \, G_0(x_3t_3, x_1t_1) \, G_0(x_2t_1, x_4t_3) \, G_0(x_4t_3, x_2t_1)$$

In general, most permutations of the order of the time variables will lead to distinct Goldstone diagrams that we all want to include. This will be discussed in Subsection 5.8.2.

Finally, we introduce time variables on every vertex to arrive at an expression where time and space coordinates are treated on equal footing

$$(-i) \; \vcenter{\hbox{}} \; = \; \frac{1}{4} \iiiint_{-\infty}^{\infty} dt_1 dt_2 dt_3 dt_4 \iiiint d\mathbf{x}_1 \, d\mathbf{x}_2 \, d\mathbf{x}_3 \, d\mathbf{x}_4$$

$$G_0(x_1t_1, x_3t_3) \, G_0(x_3t_3, x_1t_1) \, G_0(x_4t_4, x_2t_2) \, G_0(x_2t_2, x_4t_4)$$

$$\delta(t_1) \underbrace{\frac{(-i)}{|\mathbf{r}_1 - \mathbf{r}_2|} \delta(t_1 - t_2)}_{=V(\mathbf{x}_1t_1, \mathbf{x}_2t_2)} \frac{(-i)}{|\mathbf{r}_3 - \mathbf{r}_4|} \delta(t_3 - t_4)$$

$$= \frac{1}{4} \iiiint d1 \, d2 \, d3 \, d4 \, \delta(t_1)$$

$$G_0(1, 3) \, G_0(3, 1) \, V(3, 4) \, G_0(4, 2) \, G_0(2, 4) \, V(2, 1) \tag{5.44}$$

defining the propagator for the Coulomb interaction

$$V(\mathbf{x}t, \mathbf{x}'t') := \frac{(-\mathrm{i})}{|\mathbf{r} - \mathbf{r}'|}\,\delta(t - t') \tag{5.45}$$

and the short forms $G_0(1, 2) = G_0(\mathbf{x}_1 t_1, \mathbf{x}_2 t_2)$ and $\int \mathrm{d}1 = \int_{-\infty}^{\infty} \mathrm{d}t_1 \int \mathrm{d}\mathbf{r}_1 \sum_{\alpha_1}$. Figure 5.8 shows the coordinate labels used in (5.44) and it is called *Feynman diagram*.

Figure 5.8: In Feynman diagrams space and time coordinates are integrated over the entire domain and there is no required time order of the Coulomb interactions. Each vertex is given a label denoting its space and time coordinates. The propagator G_0 represents particles or holes propagating between the respective vertices and the propagator V represents Coulomb interactions between vertices. The depicted diagram is the one evaluated in (5.44).

5.8.1 Effective interaction

If the effective interaction is a multiplicative effective potential $\left(\hat{V}_{\mathrm{eff}}\psi_q\right)(\mathbf{x}) = v_{\mathrm{eff}}(\mathbf{x})\psi_q(\mathbf{x})$ we can simply use the potential $v_{\mathrm{eff}}(\mathbf{x})$ to evaluate Feynman diagrams containing effective interactions, respecting its negative sign. For a process involving a single effective interaction to be inserted between the two space-time coordinates 1 and 2 we get for instance

5.8.2 Symmetries

When dropping the constraints on the order of the interaction times we get $n!$ permutations of the initial order. We now have to consider, how many of them lead to distinct Goldstone diagrams and in turn to distinct contractions, which we all have to count. Due to symmetries some permutations may lead to the same Goldstone diagram and must not be counted more than once. Figure 5.9 shows the case for a third order diagram, where three of the six possible permutations lead to distinct Goldstone diagrams. This is due to the reflection symmetry when swapping t_1 and t_2, indicated by the dotted line.

The product of the order of all symmetry operations on a certain Feynman diagram is called its *symmetry factor*. In the example in Figure 5.9 there is only one reflection symmetry with the order 2. Thus, the symmetry factor of the considered diagram is 2, which means that

Figure 5.9: One Feynman diagram on the left represents all Goldstone diagrams originating from permutations of its interaction times t_1, t_2 and t_3. Due to the reflection symmetry when swapping t_1 and t_2, indicated by the dotted line, only three of the six permutations give rise to distinct Goldstone diagrams. The symmetry factor is 2 and the diagram must be divided by that upon evaluation.

only half of all the six permutations are distinct. The symmetry factor can be determined graphically or computer aided, considering all permutations of the vertices. For the diagram in Figure 5.8 there are 4 vertices, 2 Bosonic edges B and 4 Fermionic edges F:

$$B = \{\{1,2\}, \{3,4\}\}$$
$$F = \{(1,3), (3,1), (2,4), (4,2)\}\,.$$

The Bosonic edges are undirected since swapping the left and the right side of a Coulomb interaction leads to the same Goldstone diagram. The Fermionic edges are directed. The permutation $\tau = \begin{pmatrix} 1 & 2 & 3 & 4 \\ 4 & 3 & 2 & 1 \end{pmatrix}$ is for instance one of four permutations leaving the sets B and F unaltered:

$$\tau(B) = \{\{4,3\}, \{2,1\}\} = B$$
$$\tau(F) = \{(4,2), (2,4), (3,1), (1,3)\} = F\,,$$

thus being a symmetry operation. For this diagram, there are two reflection symmetries of order 2 resulting in a symmetry factor of 4. Therefore, the diagram has to be divided by 4 as done in (5.44).

5.8.3 Fermion sign

The Fermion sign of a Goldstone diagram is $(-1)^{l+h}$, where l is the number of Fermion loops and h is the number of hole connections in the entire diagram. In Feynman diagrams, the

negative sign for each hole connection is already contained in the definition of the propagator G_0 in (5.43) for the hole case. Thus, only the number of loops l still needs to be taken into consideration and the Fermion sign of a given Feynman diagram is

$$(-1)^l.$$

Summary

Many-body perturbation theory provides a recipe to approximate the ground state energy of the fully interacting Hamiltonian given the spin orbitals $\psi_p(\mathbf{x})$ and their eigenenergies ε_p of a single body reference, such as Hartree-Fock or DFT. It is derived from time dependent Rayleigh-Schrödinger perturbation theory which makes it extensive and thus applicable to molecules as well as solids. We can write the expansion of the perturbation series leading to the ground state in terms of connected diagrams and we can use either the rules of Goldstone diagrams or the ones of Feynman diagrams to evaluate the individual terms in the expansion.

One Goldstone diagram of order n expands in general to 2^n different contractions originating from swapping the two vertices at each Coulomb interaction. The time order of the interactions is fixed indicated by drawing the Coulomb interactions as parallel wiggly lines. Goldstone diagrams are evaluated by contracting the occurring matrix elements of the Coulomb integrals V_{sr}^{pq}. One Feynman diagram of order n expands in general to $n!$ different Goldstone diagrams arising from all permutations of the order of the interactions. The order of the interactions is not fixed and Coulomb interactions are normally not drawn as parallel lines. Feynman diagrams are evaluated by integrating the spin, space and time coordinates of all its vertices which are arguments to complex valued functions, the propagators, defining its connections.

The symmetry of a diagram determines how many distinct contractions arise from evaluating a single Goldstone or Feynman diagram. In a Goldstone diagram there can only be a global left/right symmetry with a symmetry factor of 2, while in a Feynman diagram more complex symmetries are possible. In both approaches we can define diagrams with open legs as building blocks to be inserted in larger diagrams. In the Goldstone approach this has to be done in a time ordered fashion while in Feynman diagrams it cannot be done in a time ordered way.

Although, many-body perturbation theory is a valuable framework for approximating the ground state energy it also has several drawbacks. The number of diagrams is still infinite and one can only evaluate a small subset. Using building blocks iteratively allows for evaluating an infinite number of diagrams of a certain class. This improves the results in many cases but there are still infinitely many diagrams neglected that can not be constructed by iterating building blocks. The Random Phase Approximation is a prominent example for this procedure. Another drawback of MBPT is that it requires not only the reference solutions of the unexcited states $\psi_i(x)$ and ε_i but also of the theoretically infinite number of excited states $\psi_a(x)$ and ε_a, called virtual orbitals. The convergence with respect to the number of virtual orbitals if often slow and it easilly exceeds twice the number of electrons. Finally, MBPT is not variational and one cannot give an upper bound for the ground state energy as it is given by the Hartree-Fock approximation. The non-variational nature of MBPT also considerably complicates the evaluation of analytic gradients, for instance with respect to the atom positions, i.e. forces.

Chapter 6

The Random Phase Approximation

The Random Phase Approximation (RPA) is one of the most prominent methods beyond Hartree-Fock or DFT. Historically, it has been derived within two different frameworks rather independently. Within Rayleigh-Schrödinger perturbation theory, Heisenberg already noticed that certain processes are diverging in the uniform electron gas due to the vanishing band gap and the sign of the divergence is alternating with the order. In the diagrammatic notation introduced later by Feynman and Goldstone these processes are

 $= -\infty$ $= +\infty$ $= -\infty$ ...

and they are referred to as *ring diagrams*. These divergencies pose serious problems as they render any finite order perturbation theory useless for metals. However, (Macke 1950), a student of Heisenberg, found a finite sum of all such diagrams - later to be termed RPA - if one carries out the summation over the perturbation orders before summing over the states in the perturbation expression of each term. This reconciles the use of perturbation theory for metals again. The summation over the perturbation orders can be done by iterating the diagram as a building block like in a geometric series.

With the advent of Quantum Field Theory the procedure of redefining summation orders became more common and was termed *resummation* or *renormalization*. We will not argue in depth whether this procedure is justified. After all, the sum of a conditionally convergent series depends crucially on the order in which the individual terms are summed and - even worse - any result can be achieved just by choosing an appropriate order. However, we can argue that the notion of perturbation order is in a way arbitrary regarding that it solely originates from iteratively solving the equation of motion for the time evolution operator $\hat{U}(t, t_0)$ in (5.14). Therefore, it seems a natural choice to sum over the perturbation order first.

In 1953, Bohm and Pines developed the RPA independenlty in the framework of the adiabatic connection (AC) and coined the term Random Phase Approximation. Both frameworks arrive at the same result in case of the RPA but despite the common use of diagrams in the adiabatic connection their meaning differs from Goldstone and Feynman diagrams of many-body perturbation theory discussed in Chapter 5.

From a more applied point of view, RPA poses an important improvement over Hartree-Fock and DFT. Just like finite order perturbation theories, such as Møller–Plesset PT, it can describe van der Waals interaction but unlike its finite order counterparts it can also be applied to metals. Recent developments allow the RPA to be calculated in $\mathcal{O}(N^3)$ steps, just as DFT but with a considerably higher prefactor compared to DFT (Kaltak, Klimeš, and Kresse 2014b).

6.1   RPA in the frequency domain

We will first derive the Random Phase Approximation using many-body perturbation theory in the frequency domain. Given the propagators $G_0(\mathbf{x}t, \mathbf{x}'t')$ and $V(\mathbf{x}t, \mathbf{x}'t')$ of a system according to (5.43) and (5.45), we introduce the matrix notation[1]

$$\mathbf{G}_{0\mathbf{x}\mathbf{x}'}(t - t') = G_0(\mathbf{x}t, \mathbf{x}'t') \quad \text{and} \quad \mathbf{V}_{\mathbf{x}\mathbf{x}'}(t - t') = \frac{(-\mathrm{i})}{|\mathbf{r} - \mathbf{r}'|}\, \delta(t - t') \tag{6.1}$$

noting that the propagators only depend on the time difference. We define the trace and the matrix product of two propagators $\mathbf{A}$ and $\mathbf{B}$ by

$$\mathrm{tr}\{\mathbf{A}\} = \int \mathrm{d}\mathbf{x}\, \mathbf{A}_{\mathbf{x}\mathbf{x}}\,, \qquad (\mathbf{A}\mathbf{B})_{\mathbf{x}\mathbf{x}''} = \int \mathrm{d}\mathbf{x}'\, \mathbf{A}_{\mathbf{x}\mathbf{x}'} \mathbf{B}_{\mathbf{x}'\mathbf{x}''}\,.$$

Next, we define the *independent particle polarizability* χ_0 as the first building block of the ring diagrams and we let $\mathbf{X}_0$ denote its matrix representation

$$\langle\rangle \;=\; \chi_0(\mathbf{x}t, \mathbf{x}'t') \;=\; -G_0(\mathbf{x}t, \mathbf{x}'t')\, G_0(\mathbf{x}'t', \mathbf{x}t)\,, \quad \mathbf{X}_{0\mathbf{x}\mathbf{x}'}(t - t') = \chi_0(\mathbf{x}t, \mathbf{x}'t') \tag{6.2}$$

The negative sign is required according to the Fermion sign rule of Feynman diagrams since $\mathbf{X}_0$ is one closed Fermion loop.

From now on, we will connect the building blocks $\mathbf{X}_0$ and $\mathbf{V}$ in series. In the time domain this corresponds to convolutions while it corresponds to simple products in the frequency domain. Thus, we transform $\mathbf{X}_0$ into the frequency domain with respect to the time difference, giving

$$\mathbf{X}_0(\omega) = \int \mathrm{d}(t - t')\, e^{+\mathrm{i}\omega(t - t')}\, \mathbf{X}_0(t - t')\,.$$

We use $e^{+\mathrm{i}\omega(t - t')}$ for the forward Fourier transform into the frequency domain. Using this convention, the poles of the polarizability as a function of ω coincide with the positive elementary excitation energies $\varepsilon_a - \varepsilon_i$ of $\hat{H}_0$. See (6.41) for more details in the case of the uniform electron gas. The Coulomb propagator $\mathbf{V}$ is independent of the frequency.

We can now evaluate the diagrams of the Random Phase Approximation. In (5.44) we already derived an expression for the second order ring diagram in the time domain where $\mathrm{d}i = \mathrm{d}\mathbf{x}_i\, \mathrm{d}t_i$:

$$(-\mathrm{i})\; \langle\!\langle\rangle\!\rangle \;=\; \frac{1}{4} \iiiint \mathrm{d}1\, \mathrm{d}2\, \mathrm{d}3\, \mathrm{d}4\, \delta(t_1)\, \underbrace{G_0(1,3)\, G_0(3,1)}_{=-\chi_0(1,3)}\, V(3,4)\, \underbrace{G_0(4,2)\, G_0(2,4)}_{=-\chi_0(4,2)}\, V(2,1)$$

---

[1] A matrix with continuous indices is actually an operator. However, for numerical evaluation the coordinates will be discretized justifying a matrix notation for the practical application.

In the frequency domain there is only one frequency ω to integrate over, since we have only one loop and the frequency is conserved at every vertex. The integral over all frequencies corresponds to a convolution of all time differences rather than absolute times. Therefore, we do not need to anchor the diagram at a certain time anymore, here done by $\delta(t_1)$. Using the matrix notation for the integrals over space we get

$$
\text{(diagram)} \;=\; \frac{\mathrm{i}}{4} \int \frac{\mathrm{d}\omega}{2\pi} \, \mathrm{tr}\Big\{ \mathbf{X}_0(\omega)\mathbf{V}\mathbf{X}_0(\omega)\mathbf{V} \Big\} \;=\; \frac{\mathrm{i}}{4} \int \frac{\mathrm{d}\omega}{2\pi} \, \mathrm{tr}\Big\{ (\mathbf{X}_0(\omega)\mathbf{V})^2 \Big\}. \tag{6.3}
$$

This diagram has two reflection symmetries of order 2. Thus, the symmetry factor of this diagram is 4 giving rise to the factor $1/4$ as discussed in Section 5.8. The next diagram in the RPA is the third order ring diagram. It has one reflection symmetry of order 2 and one rotational symmetry of order 3 indicated by the dotted lines. It is therefore given by

$$
\text{(diagram)} \;=\; \frac{\mathrm{i}}{2\cdot 3} \int \frac{\mathrm{d}\omega}{2\pi} \, \mathrm{tr}\Big\{ (\mathbf{X}_0(\omega)\mathbf{V})^3 \Big\}. \tag{6.4}
$$

All ring diagrams have a reflection symmetry due the symmetry of the independent particle polarizability $\mathbf{X}_0$. Additionally, each ring diagram of order n has a rotational symmetry of order n, allowing us to evaluate any given order

$$
\text{(diagram)}\; n \;=\; \frac{\mathrm{i}}{2n} \int \frac{\mathrm{d}\omega}{2\pi} \, \mathrm{tr}\Big\{ (\mathbf{X}_0(\omega)\mathbf{V})^n \Big\}. \tag{6.5}
$$

We can now do the resummation, summing over the orders before evaluating the frequency integration and the trace:

$$
\text{(diagram)} \;=\; \frac{\mathrm{i}}{2} \int \frac{\mathrm{d}\omega}{2\pi} \, \mathrm{tr}\left\{ \sum_{n=2}^{\infty} \frac{1}{n} (\mathbf{X}_0(\omega)\mathbf{V})^n \right\}. \tag{6.6}
$$

For the diagrammatic notation of the series we use the *screened interaction W* in RPA given by

$$
\overset{W}{\text{(diagram)}} \;=\; \text{(diagram)} \;+\; \text{(diagram)} \;+\; \text{(diagram)} \;+\; \ldots \tag{6.7}
$$

Note that the graphical appearance of a diagram containing the screened interaction W might be deceptive. The eye suggests a simple reflection symmetry of this diagram but in fact the symmetry factor must be considered for each order separately, as we have done it here.

Instead of carrying out the matrix products in (6.6) order by order we search for a matrix function having the same series expansion. The function $\log(1-x)$ has the power series $-x - x^2/2 - x^3/3 - \ldots$ so we can write the RPA energy as

$$
\text{(diagram)} \;=\; -\frac{\mathrm{i}}{2} \int_{-\infty}^{\infty} \frac{\mathrm{d}\omega}{2\pi} \, \mathrm{tr}\Big\{ \log\big(\mathbf{1} - \mathbf{X}_0(\omega)\mathbf{V}\big) + \mathbf{X}_0(\omega)\mathbf{V} \Big\}. \tag{6.8}
$$

$\mathbf{X}_0(\omega)$ has poles along the real frequency axis making a numerical integration difficult. We can rotate the integration contour as long as we do not cross any poles and use the imaginary frequency instead. This rotation is called *Wick rotation* and it is discussed in more detail for the uniform electron gas in Section 6.4. Given $\mathbf{X}_0(\mathrm{i}\nu)$ in imaginary frequency we can substitute $\omega = \mathrm{i}\nu$ in (6.8) and finally get

$$
\text{(diagram)} \quad = \quad \frac{1}{2}\int_{-\infty}^{\infty}\frac{\mathrm{d}\nu}{2\pi}\,\mathrm{tr}\Big\{\log\Big(\mathbf{1} - \mathbf{X}_0(\mathrm{i}\nu)\mathbf{V}\Big) + \mathbf{X}_0(\mathrm{i}\nu)\mathbf{V}\Big\}. \tag{6.9}
$$

For the uniform electron gas (UEG) we can evaluate $\mathbf{X}_0(\mathrm{i}\nu)$ and $\mathbf{V}$ analytically and use (6.9) to evaluate the RPA energy for the UEG numerically. This is done in Section 6.4. For a molecule or a solid $\mathbf{X}_0(\mathrm{i}\nu)$ has to be computed from the Hartree-Fock or DFT spin-orbitals $\psi_p(\mathbf{x})$. Instead of calculating $\mathbf{X}_0(t-t')$ in real time according to (6.2), one can already perform the Wick rotation in the time domain and evaluate

$$
\mathbf{X}_{0\mathbf{xx'}}(\mathrm{i}\tau) = -\mathbf{G}_{0\mathbf{xx'}}(\mathrm{i}\tau)\mathbf{G}_{0\mathbf{x'x}}(-\mathrm{i}\tau) \tag{6.10}
$$

in imaginary time $\mathrm{i}\tau$. Note that the matrices are multiplied elementwise. The particle/hole propagator in imaginary time is given by

$$
\mathbf{G}_{0\mathbf{xx'}}(\mathrm{i}\tau) = \begin{cases} -\sum_i \psi_i(\mathbf{x})\psi_i^*(\mathbf{x}')e^{-(\varepsilon_i-\mu)\tau} & \text{for } \tau \leq 0 \\[2mm] +\sum_a \psi_a(\mathbf{x})\psi_a^*(\mathbf{x}')e^{-(\varepsilon_a-\mu)\tau} & \text{otherwise,} \end{cases} \tag{6.11}
$$

where μ is the Fermi energy. Evaluating the energies of second order Møller–Plesset Perturbation Theory using the imaginary time propagators is equivalent to the Laplace transformed MP2 approach proposed by (Almlöf 1991). To evaluate the Random Phase Approximation $\mathbf{X}_0(\mathrm{i}\tau)$ needs to be Fourier transformed with respect to τ to arrive at the independent particle polarizability in imaginary frequency $\mathbf{X}_0(\mathrm{i}\nu)$ employed by (6.9). The Fourier transform from imaginary time to imaginary frequency, as well as the imaginary frequency integration in (6.9) can be done numerically on a non-equidistant grid to high accuracy with a only few integration points (Kaltak, Klimeš, and Kresse 2014b; Kaltak, Klimeš, and Kresse 2014a). To determine the employed quadrature frequencies and weights a function is chosen that resembles the RPA energy function and whose exact frequency integral is known. The proposed function of imaginary time is the direct MP2 term

$$
\frac{1}{2}\int\frac{\mathrm{d}\nu}{2\pi}\frac{2(\varepsilon_a - \varepsilon_i)}{(\varepsilon_a - \varepsilon_i)^2 + \nu^2}\frac{2(\varepsilon_b - \varepsilon_j)}{(\varepsilon_b - \varepsilon_j)^2 + \nu^2} = \frac{1}{\varepsilon_i + \varepsilon_j - \varepsilon_a - \varepsilon_b}
$$

which is the lowest order of the RPA expansion. The quadrature frequencies ν_k and weights w_k can then be fit such that the dominant terms with $a = b$ and $i = j$ are best reproduced by the numeric integral

$$
\frac{1}{\varepsilon_i + \varepsilon_i - \varepsilon_a - \varepsilon_a} \approx \frac{1}{2}\sum_k w_k\left(\frac{2(\varepsilon_a - \varepsilon_i)}{(\varepsilon_a - \varepsilon_i)^2 + \nu_k^2}\right)^2. \tag{6.12}
$$

This fit is done for all single particle excitation energies $\varepsilon_a - \varepsilon_i$ and the quality of the fit depends on the ratio of the largest and the smallest excitation energy $\max(\varepsilon_a - \varepsilon_i)/\min(\varepsilon_a - \varepsilon_i)$. For
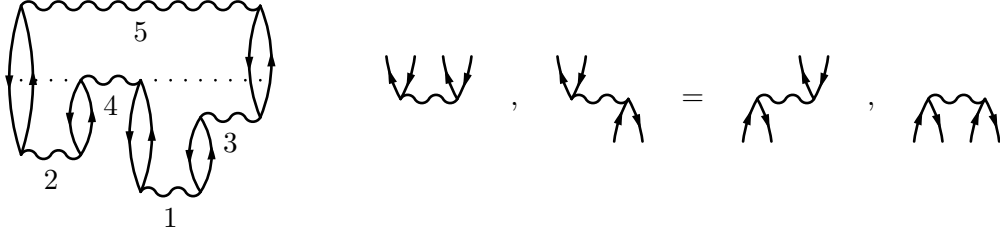
Figure 6.1: Goldstone diagram of an RPA ring diagram forming a closed loop. Each Coulomb interaction is connected to the ring in one of four possible ways of which three are distinct.

a non-metallic system the number of frequency points is negligible compared to the number of possible excitations, required in the conventional approach to calculate $\mathbf{X}_0$ from the Adler-Wiser formula (Adler 1962; Wiser 1963). The above frequency grid allows the RPA energy to be evaluated in $\mathcal{O}(N^3)$ steps, just like DFT but with a considerably higher prefactor. For a metallic system the behavior of the RPA energy for large imaginary frequencies is important for an accurate numerical quadrature. This is discussed in the end of Section 6.4.

6.2 Direct Ring Coupled Cluster Doubles

The Random Phase Approximation can also be evaluated using the matrix elements of the Coulomb integral

$$V_{sr}^{pq} = \iint \mathrm{d}\mathbf{x}\mathrm{d}\mathbf{x}' \, \psi_p^*(\mathbf{x})\psi_q^*(\mathbf{x}') \, \frac{1}{|\mathbf{r} - \mathbf{r}'|} \, \psi_r(\mathbf{x}')\psi_s(\mathbf{x})$$

rather than the propagators G_0 and V. This approach is not as efficient, however an important correction to the error remaining in the RPA is based on this approach.

The RPA ring diagrams form a closed loop and Figure 6.1 shows the Goldstone diagram of one such ring diagram. As discussed in Section 5.4, connected vertices represent contractions and we need to integrate over the time interval between Coulomb interactions. We will do that from bottom to top following the left and the right particle/hole pairs along the loop. In the diagram given as example in Figure 6.1 we start with interaction 1 following the left and the right particle/hole pairs to interaction 3. There, the right pair is contracted at one vertex and a new pair to follow on the right side emerges on the other vertex of interaction 3. Independently, we also follow the left and the right particle/hole pairs starting at interaction 2. At interaction 4 the two processes merge such that there is only one left pair and one right pair remaining after the time indicated by the dotted line. At interaction 5 both pairs are finally contracted and the loop is closed. This procedure is analogous to the one employed for deriving the Fermion sign of Goldstone diagrams in Subsection 5.4.3.

While following the left and the right particle/hole pairs we perform all occurring contractions and integrals over the respective time intervals and we keep the intermediate results in a matrix t_{ij}^{ab} depending on the states of two particle/hole pairs, diagrammatically denoted by

$$t_{ij}^{ab} = \quad \overset{a \; i \; b \; j}{\bigvee {\tiny -}{\tiny -} \bigvee} \quad .$$

t_{ij}^{ab} is called *direct ring Coupled Cluster Doubles (drCCD) amplitudes* and it contains the probability amplitude to arrive at two particle/hole pairs in the given states in any of the

possible ways forming the ring diagrams. We will now go through all cases that can occur following the left and the right particle/hole pair from bottom to top indicated in Figure 6.1.

In the first case, a Coulomb interaction creates two new particle/hole pairs as in interaction 1 in Figure 6.1. This can occur at any time in the past so we need to integrate over the time interval between the Coulomb interaction and the time where we want to use the probability amplitudes t_{ij}^{ab}, which we always move at $t = 0$. One contribution to the drCCD amplitudes is thus

$$t_{ij}^{ab} = (-\mathrm{i}) \int_{-\infty}^{0} \mathrm{d}t\, e^{\eta t}\, e^{\varepsilon_a t}\, e^{\varepsilon_b t}\, e^{-\varepsilon_i t}\, e^{-\varepsilon_j t}\, V_{ij}^{ab} + \dots$$

$$= \frac{V_{ij}^{ab}}{\varepsilon_i + \varepsilon_j - \varepsilon_a - \varepsilon_b + \mathrm{i}\eta} + \dots \tag{6.13}$$

In the next case, a Coulomb interaction contracts the right particle/hole pair creating a new one. This is the case for interaction 3 in Figure 6.1. We can now use the drCCD amplitudes recursively containing all processes until the time of the interaction. The time interval between the interaction and the time where we want to use the new drCCD amplitudes still needs to be integrated as before. The second contribution to the drCCD amplitudes is thus

$$t_{ij}^{ab} = \dots + \frac{\sum_{kc} t_{ik}^{ac} V_{cj}^{kb}}{\varepsilon_i + \varepsilon_j - \varepsilon_a - \varepsilon_b + \mathrm{i}\eta} + \dots \tag{6.14}$$

The Fermion sign of this contribution is positive since there is one more hole and one more closed Fermion loop. Note however, that the denominator is negative giving rise to the alternating sign when evaluating the RPA order by order. The same case can occur for the left particle/hole pair giving

$$t_{ij}^{ab} = \dots + \frac{\sum_{kc} V_{ic}^{ak} t_{kj}^{cb}}{\varepsilon_i + \varepsilon_j - \varepsilon_a - \varepsilon_b + \mathrm{i}\eta} + \dots \tag{6.15}$$

The last case occurs when two independent processes merge at a Coulomb interaction, as in interaction 4 of Figure 6.1. In this contribution, the drCCD amplitudes occur in a quadratic form on the right hand side

$$t_{ij}^{ab} = \dots + \frac{\sum_{klcd} t_{ik}^{ac} V_{cd}^{kl} t_{lj}^{db}}{\varepsilon_i + \varepsilon_j - \varepsilon_a - \varepsilon_b + \mathrm{i}\eta} \cdot \tag{6.16}$$

Taking all contribution (6.13) to (6.16) into consideration and taking the limit $\eta \to 0$ yields the drCCD amplitudes equation

$$(\varepsilon_i + \varepsilon_j - \varepsilon_a - \varepsilon_b)\, t_{ij}^{ab} = V_{ij}^{ab} + \sum_{kc} t_{ik}^{ac} V_{cj}^{kb} + \sum_{kc} V_{ic}^{ak} t_{kj}^{cb} + \sum_{klcd} t_{ik}^{ac} V_{cd}^{kl} t_{lj}^{db}\,. \tag{6.17}$$

This equation is quadratic and can only be solved by iteration. The convergence with respect to the number of iterations is, however, fast. Employing a Shanks transform, 8 iterations are sufficient to yield a converged RPA energy to 5 significant digits of precision even for a system with a low band gap, such as a finite size uniform electron gas (Freeman 1977; Shanks 1955). Each iteration is still costly requiring $\mathcal{O}(N^5)$ steps. The iteration process also requires the amplitudes to be stored demanding $\mathcal{O}(N^4)$ of memory.

Given the drCCD amplitudes, we can evaluate the RPA energy by contracting both particle/hole pairs with the last Coulomb interaction, corresponding to interaction 5 in Figure 6.1. The drCCD amplitudes have a left/right reflection symmetry. The RPA energy is thus

$$ \text{\raisebox{-1ex}{\includegraphics}} \quad = \quad \frac{1}{2} \sum_{ijab} t^{ab}_{ij} V^{ij}_{ab} \,, \tag{6.18} $$

where the two closing Fermion loops result in a positive Fermion sign.

In this approach the time order is always maintained by the way the drCCD amplitudes are recursively defined. Therefore, no particular symmetries have to be considered apart from the reflection symmetry. Ring diagrams that have more than two particle/hole pairs at some instances in time arise from the quadratic contribution (6.16). This is the case for the diagram in Figure 6.1 between interaction 2 and 4. Excluding the quadratic contribution (6.16) gives the *Tamm-Dancoff Approximation (TDA)*, which is the subset of all RPA ring diagrams where there are exactly two particle/hole pairs at all times between the first and the last interaction. From (6.16) and (6.13) follows that the lowest order diagram of RPA that is not part of TDA is of fourth order.

On the other hand, the drCCD amplitude equations are a subset of the amplitude equations including all possible ways to arrive at two particle/hole pairs. These amplitude equations are called *Coupled Cluster Singles Doubles (CCSD) amplitudes* and they contain processes such as

$$ \text{\raisebox{-2ex}{\includegraphics}} \;. $$

Unfortunately, it is computationally more time consuming to calculate the full CCSD amplitudes, scaling like $\mathcal{O}(N^6)$, since the employed tensor multiplications cannot be split into pieces, involving no more than 5 indices. For the calculation of the drCCD amplitudes this can be done. since the matrix of the Coulomb interaction V^{pq}_{sr} can be decomposed into a product of two tensors with 3 indices in the momentum basis:

$$ V^{pq}_{sr} = \int \frac{\mathrm{d}\mathbf{G}}{(2\pi)^3} \, \chi^p_s(\mathbf{G}) \, \chi^{r*}_q(\mathbf{G}) \,, \quad \text{with } \chi^p_q(\mathbf{G}) = \int \mathrm{d}\mathbf{x} \, \frac{\sqrt{4\pi}}{|\mathbf{G}|} \, \psi^*_p(\mathbf{x}) e^{i\mathbf{r}\cdot\mathbf{G}} \psi_q(\mathbf{x}) \,. $$

This allows tensor products involving V^{pq}_{sr} to be "cut" at the Coulomb line, accelerating the evaluation of the direct ring Coupled Cluster Doubles amplitudes to $\mathcal{O}(N^5)$. For the first non-trivial case in (6.17), this is done, for instance, by

$$ \sigma^a_i(\mathbf{G}) = \sum_{ck} t^{ac}_{ik} \chi^k_c(\mathbf{G}) \,, \qquad (\varepsilon_i + \varepsilon_j - \varepsilon_a - \varepsilon_b) \, t^{ab}_{ij} = \ldots + \int \frac{\mathrm{d}\mathbf{G}}{(2\pi)^3} \, \sigma^a_i(\mathbf{G}) \chi^{j*}_b(\mathbf{G}) + \ldots $$

The Coupled Cluster method was developed by (Coester and Kümmel 1960) for the atomic nucleus and later adopted for electronic correlation by (Čížek 1969).

6.3   RPA from the Adiabatic Connection

In the framework of many-body perturbation theory the derivation of the Random Phase Approximation is straight forward. According to the last two sections it can be done either in the frequency domain employing Feynman diagrams and regarding the symmetries of the ring diagrams or in the time domain employing Goldstone diagrams. In Chapter 5 we discussed the equivalence of the two approaches.

Despite the straight forward derivations and the general applicability of many-body perturbation theory to arbitrary reference systems, neither of the two previously discussed derivations are considered standard approaches to the Random Phase Approximation. In this section we discuss the framework of the Adiabatic Connection (AC) employed by Bohm and Pines, which is considered the standard approach to the RPA, at least in solid state physics.

In the Adiabatic Connection (AC) we define a Hamiltonian $\hat{H}(\lambda)$ depending on a coupling constant λ specifying the strength of the full electron-electron Coulomb interaction

$$\hat{H}(\lambda) = \hat{T} + \hat{V}_{\text{ne}} + \hat{V}_{\text{eff}}(\lambda) + \lambda\hat{V}_{\text{ee}}, \quad \lambda \in [0, 1]. \tag{6.19}$$

The effective interaction $\hat{V}_{\text{eff}}(\lambda)$ also depends on the coupling constant and we choose $\hat{V}_{\text{eff}}(\lambda)$ such that the density of the system with the Hamiltonian $\hat{H}(\lambda)$ is for all λ equivalent to the density of the fully interacting system with the Hamiltonian $\hat{H}(1)$. This is in contrast to many-body perturbation theory where the effective interaction is simply scaled by the factor $1 - \lambda$ according to (5.15) and where λ is time dependent. Requiring a constant density for all λ is a strong condition implying that the density of the reference system with the Hamiltonian $\hat{H}(0)$ is equivalent to the density of the fully interacting system. Although this condition is met to a good degree by using a DFT Hamiltonian for $\hat{H}(0)$, the Hohenberg-Kohn theorem only states the existence of such an effective potential $\hat{V}_{\text{eff}}(\lambda)$. For practical considerations it is known that in general no DFT density fully agrees with the density of the respective fully interacting system.

Let now $\Psi(\lambda)$ denote the normalized ground state of the respective Hamiltonian $\hat{H}(\lambda)$, being the solution of

$$\hat{H}(\lambda)\ket{\Psi(\lambda)} = E\ket{\Psi(\lambda)}.$$

The ground state energy E is equivalent for all λ since E is a functional of the density according to the Hohenberg-Kohn theorem and the density is the same for all λ. Even assuming that the density $n(\mathbf{r})$ of the DFT reference is exact we can only directly evaluate the nuclei-electron potential energy E_{ne} as the functionals for the kinetic energy T and for the electron-electron potential energy E_{ee} are unknown:

$$E[n(\mathbf{r})] = T[n(\mathbf{r})] + E_{\text{ne}}[n(\mathbf{r})] + E_{\text{ee}}[n(\mathbf{r})].$$

However, we are only interested in the sum of the kinetic and the potential energy so we may as well use the known kinetic energy of the Kohn-Sham system

$$T_{\text{S}} = -\Big\langle\Psi(0)\Big|\sum_{n=1}^{N}\frac{\nabla_n^2}{2}\Big|\Psi(0)\Big\rangle$$

and ask for the energy to be added to T_{S} and E_{ne} to arrive at the same total energy E. This energy is called *Hartree-exchange-correlation energy* and it is given by

$$E_{\text{Hxc}} = E - E_{\text{ne}} - T_{\text{S}}.$$

Using (6.19) we can express the terms above by expectation values of the fully and the non-interacting Hamiltonian:

$$E - E_{\text{ne}} = \langle \Psi(1)|\hat{H}(1)|\Psi(1)\rangle - \langle \Psi(1)|\hat{V}_{\text{ne}} + \hat{V}_{\text{eff}}(1)|\Psi(1)\rangle$$

$$T_{\text{S}} = \langle \Psi(0)|\hat{H}(0)|\Psi(0)\rangle - \langle \Psi(0)|\hat{V}_{\text{ne}} + \hat{V}_{\text{eff}}(0)|\Psi(0)\rangle,$$

noting that $\hat{V}_{\text{eff}}(1) = \hat{0}$ and $\hat{V}_{\text{eff}}(0)$ is the effective potential of the Kohn-Sham system. This allows us to make the connection between the fully interacting and the non-interacting system

$$E_{\text{Hxc}} = \int_0^1 \mathrm{d}\lambda \frac{\mathrm{d}}{\mathrm{d}\lambda} \langle \Psi(\lambda)|\hat{H}(\lambda) - \hat{V}_{\text{ne}} - \hat{V}_{\text{eff}}(\lambda)|\Psi(\lambda)\rangle \tag{6.20}$$

$\Psi(\lambda)$ is the ground state of $\hat{H}(\lambda)$. As a consequence, we can use the Güttinger theorem (Güttinger 1932), also known as Hellman-Feynman theorem, to evaluate the total derivative of the expectation values involving the Hamiltonian:

$$\frac{\mathrm{d}}{\mathrm{d}\lambda} \langle \Psi(\lambda)|\hat{H}(\lambda)|\Psi(\lambda)\rangle = \left\langle \Psi(\lambda)\left|\frac{\mathrm{d}}{\mathrm{d}\lambda}\hat{H}(\lambda)\right|\Psi(\lambda)\right\rangle \tag{6.21}$$

Furthermore, $\hat{V}_{\text{ne}}$ and $\hat{V}_{\text{eff}}(\lambda)$ are local potentials and their expectation value only depends on the electron density $n(\mathbf{r})$. Since the density is constant for all λ the total derivate of their respective expectation value simplifies to

$$\frac{\mathrm{d}}{\mathrm{d}\lambda} \langle \Psi(\lambda)|\hat{V}_{\text{ne}}|\Psi(\lambda)\rangle = 0 \tag{6.22}$$

$$\frac{\mathrm{d}}{\mathrm{d}\lambda} \langle \Psi(\lambda)|\hat{V}_{\text{eff}}(\lambda)|\Psi(\lambda)\rangle = \left\langle \Psi(\lambda)\left|\frac{\mathrm{d}}{\mathrm{d}\lambda}\hat{V}_{\text{eff}}(\lambda)\right|\Psi(\lambda)\right\rangle. \tag{6.23}$$

Inserting the total derivatives into (6.20) yields the final expression for the Hartree-exchange-correlation energy in the adiabatic connection:

$$E_{\text{Hxc}} = \int_0^1 \mathrm{d}\lambda \langle \Psi(\lambda)|\hat{V}_{\text{ee}}|\Psi(\lambda)\rangle. \tag{6.24}$$

In other words, the Hartree-exchange-correlation energy is the coupling strength averaged potential electron-electron energy.

6.3.1 Fluctuation dissipation theorem

Equation (6.24) cannot be evaluated directly since the ground states $\Psi(\lambda)$ are not available for any λ except 0. However, the whole information of the many-body wavefunction $\Psi(\lambda)$ is not required to evaluate the Coulomb operator. The pair density $n^2(\mathbf{x}, \mathbf{x}')$ is sufficient:

$$\langle \Psi|\hat{V}_{\text{ee}}|\Psi\rangle = \int \mathrm{d}\mathbf{x}_1 \ldots \int \mathrm{d}\mathbf{x}_N \, \Psi^*(\mathbf{x}_1, \ldots, \mathbf{x}_N) \frac{1}{2} \sum_{n \neq m} \frac{1}{|\mathbf{r}_n - \mathbf{r}_m|} \Psi(\mathbf{x}_1, \ldots, \mathbf{x}_N)$$

$$= \frac{1}{2} \int \mathrm{d}\mathbf{x} \int \mathrm{d}\mathbf{x}' \frac{1}{|\mathbf{r} - \mathbf{r}'|} \underbrace{\int \mathrm{d}\mathbf{x}_1 \ldots \int \mathrm{d}\mathbf{x}_N \, \Psi^*(\ldots) \sum_{n \neq m} \delta(\mathbf{x} - \mathbf{x}_n)\delta(\mathbf{x}' - x_m) \, \Psi(\ldots)}_{= n^2(\mathbf{x}, \mathbf{x}')}$$

The pair density can be written in terms of unrestricted summations

$$n^2(\mathbf{x}, \mathbf{x}') = \left\langle \Psi \Big| \sum_{n \neq m} \delta(\mathbf{x} - \mathbf{x}_n)\delta(\mathbf{x}' - \mathbf{x}_m) \Big| \Psi \right\rangle$$

$$= \left\langle \Psi \Big| \sum_{nm} \delta(\mathbf{x} - \mathbf{x}_n)\delta(\mathbf{x}' - \mathbf{x}_m) \Big| \Psi \right\rangle - \underbrace{\left\langle \Psi \Big| \sum_{n} \delta(\mathbf{x} - \mathbf{x}')\delta(\mathbf{x} - \mathbf{x}_n) \Big| \Psi \right\rangle}_{= \delta(\mathbf{x} - \mathbf{x}')n(\mathbf{x})},$$

which allows us to relate it to the density fluctuation operator $\delta\hat{n}(x) = \sum_n \delta(\mathbf{x} - \mathbf{x}_n) - n(x)$, since

$$\langle\Psi|\delta\hat{n}(\mathbf{x})\delta\hat{n}(\mathbf{x}')|\Psi\rangle = \left\langle \Psi \Big| \sum_{n} \delta(\mathbf{x} - \mathbf{x}_n) \sum_{m} \delta(\mathbf{x}' - \mathbf{x}_m) \Big| \Psi \right\rangle + n(\mathbf{x})n(\mathbf{x}')$$

$$- \underbrace{\left\langle \Psi \Big| \sum_{n} \delta(\mathbf{x} - \mathbf{x}_n) \Big| \Psi \right\rangle}_{= n(\mathbf{x})} n(\mathbf{x}') - n(\mathbf{x})n(\mathbf{x}').$$

The pair density and the density fluctuation operator are thus related by

$$n^2(\mathbf{x}, \mathbf{x}') = \langle\Psi|\delta\hat{n}(\mathbf{x})\delta\hat{n}(\mathbf{x}')|\Psi\rangle + n(\mathbf{x})n(\mathbf{x}') - \delta(\mathbf{x} - \mathbf{x}')n(\mathbf{x}). \tag{6.25}$$

Note that although $\langle\Psi|\delta\hat{n}(\mathbf{x})|\Psi\rangle$ is zero, the expectation value of a quadratic form of the density fluctuation operator is in general non-zero. The fluctuation dissipation theorem links the density-density fluctuations at the two sites $\mathbf{x}$ and $\mathbf{x}'$ occurring in (6.25) to the density-density response function $\chi_\lambda(\mathbf{x}, \mathbf{x}', i\nu)$ of the system with the coupling strength λ, here given in imaginary frequency:

$$-\int \frac{d\nu}{2\pi} \chi_\lambda(\mathbf{x}, \mathbf{x}', i\nu) = \langle\Psi(\lambda)|\delta\hat{n}(\mathbf{x})\delta\hat{n}(\mathbf{x}')|\Psi(\lambda)\rangle. \tag{6.26}$$

With time dependent density functional theory (TDDFT) we can finally connect the density-density response function χ_λ of the system with a coupling strength λ to the density-density response function χ_0 of the DFT reference system

$$\chi_\lambda(\mathbf{x}_1, \mathbf{x}_4, i\nu) = \chi_0(\mathbf{x}_1, \mathbf{x}_4, i\nu)$$
$$+ \iint d\mathbf{x}_2 d\mathbf{x}_3 \, \chi_0(\mathbf{x}_1, \mathbf{x}_2, i\nu) \left(\frac{\lambda}{|\mathbf{r}_2 - \mathbf{r}_3|} + f_{xc}^\lambda(\mathbf{x}_2, \mathbf{x}_3, i\nu) \right) \chi_\lambda(\mathbf{x}_3, \mathbf{x}_4, i\nu), \tag{6.27}$$

where the Coulomb interaction is scaled by λ. f_{xc}^λ is called *exchange-correlation kernel* and it contains the change of the DFT effective potential with respect to a change in the electron density. f_{xc}^λ is not explicitly known and it is coupling strength dependent. (6.27) is an implicit integral equation for χ_λ called *Dyson-like equation*. It requires that the density response of the interacting system to a change of the external potential is the same as the density response of the DFT reference system to a change of the effective potential. This assumption is the TDDFT counterpart of the assumption that the DFT density is exact.

The response function of the DFT reference system χ_0 can be evaluated from the DFT spin-orbitals $\psi_p(\mathbf{x})$ with first order perturbation theory:

$$\chi_0(\mathbf{x}, \mathbf{x}', i\nu) = -\sum_{ia} \left(\frac{\psi_a(\mathbf{x})\psi_a^*(\mathbf{x}')\psi_i(\mathbf{x}')\psi_i^*(\mathbf{x})}{\varepsilon_a - \varepsilon_i - i\nu} + \frac{\psi_i(\mathbf{x})\psi_i^*(\mathbf{x}')\psi_a(\mathbf{x}')\psi_a^*(\mathbf{x})}{\varepsilon_a - \varepsilon_i + i\nu} \right) \tag{6.28}$$

See (6.45) for an analogous derivation of the above result for the uniform electron gas. Note that the definition of χ_0 given in this section expects the Coulomb propagator to be $1/|\mathbf{r}-\mathbf{r}'|$. This differs from the convention used elsewhere in this work and has been chosen for consistency of this section with literature. In (6.51) this is discussed in detail. The above definition further assumes a spin-unrestricted reference and an imaginary frequency integration over the entire domain from $-\infty$ to ∞.

Using (6.24), (6.25) and (6.26) the Hartree-exchange-correlation energy is given by

$$
\begin{aligned}
E_{\text{Hxc}} &= \frac{1}{2}\int_0^1 \mathrm{d}\lambda \int \mathrm{d}\mathbf{x} \int \mathrm{d}\mathbf{x}' \frac{1}{|\mathbf{r}-\mathbf{r}'|}\left(n(\mathbf{x})n(\mathbf{x}') - \delta(\mathbf{x}-\mathbf{x}')n(\mathbf{x}) - \int \frac{\mathrm{d}\nu}{2\pi}\chi_\lambda(\mathbf{x},\mathbf{x}',\mathrm{i}\nu)\right) \\
&= E_{\text{H}} + \frac{1}{2}\int_0^1 \mathrm{d}\lambda \int \mathrm{d}\mathbf{x} \int \mathrm{d}\mathbf{x}' \frac{1}{|\mathbf{r}-\mathbf{r}'|}\left(-\delta(\mathbf{x}-\mathbf{x}')n(\mathbf{x}) - \int \frac{\mathrm{d}\nu}{2\pi}\chi_\lambda(\mathbf{x},\mathbf{x}',\mathrm{i}\nu)\right) , \quad (6.29)
\end{aligned}
$$

where the Hartree energy E_{H} is readily factored out. To tackle the remaining Dirac delta function we rewrite $n(\mathbf{x}) = \sum_i \psi_i(\mathbf{x})\psi_i^*(\mathbf{x})$ in the context of the delta function and then use the completeness of the eigenstates $\psi_p(\mathbf{x})$:

$$
\begin{aligned}
\delta(\mathbf{x}-\mathbf{x}')n(\mathbf{x}) &= \delta(\mathbf{x}-\mathbf{x}')\sum_i \psi_i(\mathbf{x}')\psi_i^*(\mathbf{x}) = \sum_{pi}\psi_p(\mathbf{x})\psi_p^*(\mathbf{x}')\psi_i(\mathbf{x}')\psi_i^*(\mathbf{x}) \\
&= \sum_{ji}\psi_j(\mathbf{x})\psi_j^*(\mathbf{x}')\psi_i(\mathbf{x}')\psi_i^*(\mathbf{x}) + \sum_{ai}\psi_a(\mathbf{x})\psi_a^*(\mathbf{x}')\psi_i(\mathbf{x}')\psi_i^*(\mathbf{x}) . \quad (6.30)
\end{aligned}
$$

The first sum over unexcited states can be inserted into (6.29) and factored out giving the *exact exchange* energy

$$
\overset{\displaystyle\bigcirc\!\!\!\!\!\!\!\!\!\longleftrightarrow}{} \qquad E_{\text{x}} = -\frac{1}{2}\int \mathrm{d}\mathbf{x} \int \mathrm{d}\mathbf{x}' \sum_{ij}\frac{\psi_j(\mathbf{x})\psi_j^*(\mathbf{x}')\psi_i(\mathbf{x}')\psi_i^*(\mathbf{x})}{|\mathbf{r}-\mathbf{r}'|} .
$$

The exact exchange energy corresponds to the given first order diagram in many-body perturbation theory with the Kohn-Sham spin-orbitals $\psi_p(\mathbf{x})$ as reference system.

The second sum in (6.30) over excited and unexcited states is the integral of $\chi_0(\mathbf{x},\mathbf{x}',\mathrm{i}\nu)$ given in (6.28) over all imaginary frequencies. Note that there is only one pole at $\nu = \mp\mathrm{i}(\varepsilon_a - \varepsilon_i)$ requiring a convergence factor of $e^{-\mathrm{i}\nu\tau}$ with $0 < |\tau| \ll 1$ for a contour enclosing the pole with vanishing contribution at infinity. We choose to take the limit $\tau \to 0^+$ from above resulting in a clockwise contour. The sum over the residue gives

$$
\int \frac{\mathrm{d}\nu}{2\pi}\chi_0(\mathbf{x},\mathbf{x}',\mathrm{i}\nu) = -\sum_{ia}\psi_a(\mathbf{x})\psi_a^*(\mathbf{x}')\psi_i(\mathbf{x}')\psi_i^*(\mathbf{x}) .
$$

The above result can also be obtained evaluating $\chi_0(\mathbf{x},\mathbf{x}',\mathrm{i}\tau)$ using imaginary time propagators according to (6.10) and (6.11) and then taking the limit $\tau \to 0^+$. Finally, we can insert the exact exchange energy and the above expression into (6.29) to arrive at an expression for the correlation energy:

$$
E_{\text{c}} = -\frac{1}{2}\int_0^1 \mathrm{d}\lambda \int \mathrm{d}\mathbf{x} \int \mathrm{d}\mathbf{x}' \frac{1}{|\mathbf{r}-\mathbf{r}'|}\int \frac{\mathrm{d}\nu}{2\pi}\left(\chi_\lambda(\mathbf{x},\mathbf{x}',\mathrm{i}\nu) - \chi_0(\mathbf{x},\mathbf{x}',\mathrm{i}\nu)\right) , \qquad (6.31)
$$

where $E_{\text{Hxc}} = E_{\text{H}} + E_{\text{x}} + E_{\text{c}}$.

6.3.2   Random Phase Approximation of the polarizability

The Dyson-like equation (6.27) for the polarizability $\chi_\lambda(\mathbf{x}, \mathbf{x}', i\nu)$ can be written in the matrix notation introduced in Section 6.1

$$\mathbf{X}_\lambda(i\nu) = \mathbf{X}_0(i\nu) + \mathbf{X}_0(i\nu)\left(\lambda\mathbf{V} + \mathbf{F}^\lambda_{xc}(i\nu)\right)\mathbf{X}_\lambda(i\nu). \tag{6.32}$$

In the Random Phase Approximation one considers only the Hartree term in the time dependent density functional theory derivation of the above Dyson-like equation, neglecting the exchange correlation kernel $\mathbf{F}^\lambda_{xc}$. The polarizability can then be expanded to

$$\mathbf{X}_\lambda(i\nu) = \mathbf{X}_0(i\nu) + \lambda\mathbf{X}_0(i\nu)\mathbf{V}\mathbf{X}_0(i\nu) + \lambda^2\mathbf{X}_0(i\nu)\mathbf{V}\mathbf{X}_0(i\nu)\mathbf{V}\mathbf{X}_0(i\nu) + \dots$$

Writing (6.31) in the matrix notation and inserting the above expansion gives

$$\begin{aligned}
E_c &= -\frac{1}{2}\int_0^1 d\lambda \int \frac{d\nu}{2\pi} \, \mathrm{tr}\big\{\mathbf{X}_\lambda(i\nu)\mathbf{V} - \mathbf{X}_0(i\nu)\mathbf{V}\big\} \\
&= -\frac{1}{2}\int_0^1 d\lambda \int \frac{d\nu}{2\pi} \, \mathrm{tr}\left\{\lambda\big(\mathbf{X}_0(i\nu)\mathbf{V}\big)^2 + \lambda^2\big(\mathbf{X}_0(i\nu)\mathbf{V}\big)^3 + \dots\right\}.
\end{aligned} \tag{6.33}$$

The explicitly known λ dependency allows us to integrate λ analytically, which leads to the final expression of the correlation energy in the Random Phase Approximation:

$$\begin{aligned}
E_c^{\mathrm{RPA}} &= -\frac{1}{2}\int \frac{d\nu}{2\pi} \, \mathrm{tr}\left\{\frac{1}{2}\big(\mathbf{X}_0(i\nu)\mathbf{V}\big)^2 + \frac{1}{3}\big(\mathbf{X}_0(i\nu)\mathbf{V}\big)^3 + \dots\right\} \\
&= +\frac{1}{2}\int \frac{d\nu}{2\pi} \, \mathrm{tr}\left\{\log\big(\mathbf{1} - \mathbf{X}_0(i\nu)\mathbf{V}\big) + \mathbf{X}_0(i\nu)\mathbf{V}\right\}.
\end{aligned} \tag{6.34}$$

This result is formally equivalent to (6.9) although two very different approaches have been used in the respective derivations. The prescribed Hartree E_H and exact-exchange term E_x also correspond to the two first order diagrams in many-body perturbation theory using a non-Hartree-Fock reference. Note however, that the factors in the series expansion

$$\frac{1}{2}\big(\mathbf{X}_0(i\nu)\mathbf{V}\big)^2 + \frac{1}{3}\big(\mathbf{X}_0(i\nu)\mathbf{V}\big)^3 + \dots$$

have entirely different reasons in the two approaches. In the approach using many-body perturbation theory they originate from the rotational symmetry of the ring diagrams. In the Adiabatic Connection, on the other side, they stem from averaging the potential energy over all λ to arrive at the total energy. Thus, the two approaches can very well disagree when different classes of diagrams are considered.

6.4   RPA for the uniform electron gas

In this section we apply the framework of many-body perturbation theory as discussed in Chapter 5 to the uniform electron gas (UEG) and and use resulting propagators to calculate the Random Phase Approximation for this system.

We choose the free Hamiltonian as a reference only containing the kinetic energy

$$\hat{H}_0 = -\sum_{n=1}^N \frac{\nabla_n^2}{2}$$

for a system with N electrons in a cubic box of length a and volume $\Omega = a^3$. The solutions of the non-interacting Hamiltonian are plane waves commensurate with the box. The normalized spin orbitals and eigenenergies are

$$\psi_{\sigma\mathbf{k}}(\alpha\mathbf{r}) = \delta_{\sigma\alpha}\frac{1}{\sqrt{\Omega}}e^{\mathrm{i}\mathbf{k}\cdot\mathbf{r}}, \qquad \varepsilon_{\sigma\mathbf{k}} = \frac{\mathbf{k}^2}{2}, \qquad \text{where } \mathbf{k} \in \frac{2\pi}{a}\mathbb{Z}^3, \text{ and } \sigma, \alpha \in \{\uparrow, \downarrow\}. \qquad (6.35)$$

The uniform electron gas is the limit of this system taking its volume Ω to infinity while keeping the electron density N/Ω fixed. The average volume per electron is usually given by specifying the the radius r_s of a sphere of equal volume

$$\Omega/N = \frac{4\pi r_s^3}{3}. \qquad (6.36)$$

r_s is called *Wigner–Seitz radius*. In the non-interacting ground state the lowest N spin-orbitals are occupied and the wave numbers $\mathbf{k}$ of these states lie inside a sphere called *Fermi sphere* with radius k_F:

$$\sum_{\sigma, |\mathbf{k}| < k_\mathrm{F}} = N. \qquad (6.37)$$

The density of the wave vectors $\mathbf{k} \in 2\pi\mathbb{Z}^3/a$ increases with increasing box volume so we can approximate the above sum by an appropriate integral

$$\sum_{\sigma, \mathbf{k}} = \sum_\sigma \int \frac{\Omega}{(2\pi)^3}\,\mathrm{d}\mathbf{k} \qquad (6.38)$$

and use it together with (6.37) and (6.36) to find k_F as a function of the Wigner–Seitz radius r_s:

$$k_\mathrm{F}^3 = \frac{9\pi}{2\sum_\sigma}\frac{1}{r_s^3}. \qquad (6.39)$$

In the non-spin polarized case $\sum_\sigma = 2$ and in the spin polarized case $\sum_\sigma = 1$.

6.4.1 Propagators

We can now evaluate the propagators for the uniform electron gas according to (5.43):

$$G_0(\alpha\mathbf{r}t, \alpha'\mathbf{r}'t') = \begin{cases} -\displaystyle\sum_{\sigma, |\mathbf{k}| < k_\mathrm{F}} \psi_{\sigma\mathbf{k}}(\alpha\mathbf{r})\psi_{\sigma\mathbf{k}}^*(\alpha'\mathbf{r}')e^{(-\mathrm{i}\varepsilon_{\sigma\mathbf{k}}+\eta)(t-t')} & \text{for } t \le t' \\[2mm] +\displaystyle\sum_{\sigma, |\mathbf{k}| \ge k_\mathrm{F}} \psi_{\sigma\mathbf{k}}(\alpha\mathbf{r})\psi_{\sigma\mathbf{k}}^*(\alpha'\mathbf{r}')e^{(-\mathrm{i}\varepsilon_{\sigma\mathbf{k}}-\eta)(t-t')} & \text{otherwise.} \end{cases}$$

Inserting the spin orbitals and eigenenergies from (6.35) and approximating the sum over states by the appropriate integral from (6.38) gives

$$G_0(\alpha\mathbf{r}t, \alpha'\mathbf{r}'t') = \begin{cases} -\displaystyle\int\limits_{|\mathbf{k}'| < k_\mathrm{F}} \frac{\mathrm{d}\mathbf{k}'}{(2\pi)^3}\,\delta_{\alpha\alpha'}\,e^{\mathrm{i}\mathbf{k}'\cdot(\mathbf{r}-\mathbf{r}')}e^{(-\mathrm{i}\mathbf{k}'^2/2+\eta)(t-t')} & \text{for } t \le t' \\[4mm] +\displaystyle\int\limits_{|\mathbf{k}'| \ge k_\mathrm{F}} \frac{\mathrm{d}\mathbf{k}'}{(2\pi)^3}\,\delta_{\alpha\alpha'}\,e^{\mathrm{i}\mathbf{k}'\cdot(\mathbf{r}-\mathbf{r}')}e^{(-\mathrm{i}\mathbf{k}'^2/2-\eta)(t-t')} & \text{otherwise,} \end{cases}$$

which we can transform into momentum space $\mathbf{k}$ with respect to $(\mathbf{r} - \mathbf{r}')$. For the case $t \leq t'$ this yields

$$- \int \mathrm{d}(\mathbf{r} - \mathbf{r}') e^{-\mathrm{i}\mathbf{k} \cdot (\mathbf{r} - \mathbf{r}')} \int\limits_{|\mathbf{k}'| < k_{\mathrm{F}}} \frac{\mathrm{d}\mathbf{k}'}{(2\pi)^3} \, \delta_{\alpha\alpha'} \, e^{\mathrm{i}\mathbf{k}' \cdot (\mathbf{r} - \mathbf{r}')} e^{(-\mathrm{i}\mathbf{k}'^2/2 + \eta)(t - t')}$$

$$= - \int\limits_{|\mathbf{k}'| < k_{\mathrm{F}}} \frac{\mathrm{d}\mathbf{k}'}{(2\pi)^3} \, (2\pi)^3 \, \delta(\mathbf{k}' - \mathbf{k}) \, \delta_{\alpha\alpha'} \, e^{(-\mathrm{i}\mathbf{k}'^2/2 + \eta)(t - t')}$$

$$= - \theta(k_{\mathrm{F}} - |\mathbf{k}|) \, \delta_{\alpha\alpha'} \, e^{(-\mathrm{i}\mathbf{k}^2/2 + \eta)(t - t')} \, ,$$

where $\theta(x)$ is the Heaviside step function. In the general case this gives

$$G_0(\mathbf{k}, t - t') = \begin{cases} -\theta(k_{\mathrm{F}} - |\mathbf{k}|) \, e^{(-\mathrm{i}\mathbf{k}^2/2 + \eta)(t - t')} & \text{for } t \leq t' \\ +\theta(|\mathbf{k}| - k_{\mathrm{F}}) \, e^{(-\mathrm{i}\mathbf{k}^2/2 - \eta)(t - t')} & \text{otherwise,} \end{cases} \tag{6.40}$$

as a function of $\mathbf{k}$ and the time difference $(t - t')$, omitting the electron spins. Finally, we can transform the propagator into frequency space ω with respect to $(t - t')$. For the case $t \leq t'$ this gives

$$- \int_{-\infty}^{0} \mathrm{d}(t - t') \, e^{+\mathrm{i}\omega(t - t')} \, \theta(k_{\mathrm{F}} - |\mathbf{k}|) \, e^{(-\mathrm{i}\mathbf{k}^2/2 + \eta)(t - t')}$$

$$= - \frac{(1 - 0) \, \theta(k_{\mathrm{F}} - |\mathbf{k}|)}{\mathrm{i}(\omega - \mathbf{k}^2/2) + \eta} = \frac{\mathrm{i} \, \theta(k_{\mathrm{F}} - |\mathbf{k}|)}{\omega - \mathbf{k}^2/2 - \mathrm{i}\eta} \, .$$

Note that, unlike for the momentum, we use $e^{+\mathrm{i}\omega(t - t')}$ for the forward Fourier transform into frequency space so that the poles of the propagator coincide with the positive eigenenergies. The particle/hole propagator is now quite compact, even for the general case:

$$G_0(\mathbf{k}, \omega) = \frac{\mathrm{i}}{\omega - \mathbf{k}^2/2 + \mathrm{i}\eta_{\mathbf{k}}} \, , \qquad \text{where } \eta_{\mathbf{k}} = \begin{cases} -\eta & \text{for } |\mathbf{k}| < k_{\mathrm{F}} \\ +\eta & \text{otherwise.} \end{cases} \tag{6.41}$$

In the space and time domain we have to integrate over all spins, space and time coordinates of each vertex:

$$\sum_\alpha \int_\Omega \mathrm{d}\mathbf{r} \int \mathrm{d}t \, .$$

In the momentum and frequency domain we integrate over all spins, momenta and frequencies of all propagators connecting the vertices:

$$\sum_\alpha \int \frac{\Omega}{(2\pi)^3} \, \mathrm{d}\mathbf{k} \int \frac{1}{2\pi} \, \mathrm{d}\omega \, . \tag{6.42}$$

Next, we also want to transform the propagator for the Coulomb interaction

$$V(\alpha \mathbf{r} t, \alpha' \mathbf{r}' t') = \frac{-\mathrm{i}}{|\mathbf{r} - \mathbf{r}'|} \, \delta(t - t')$$

in the momentum and frequency domain. The transform with respect to $(t - t')$ is straight forward and simply gives a frequency independent propagator

$$V(\mathbf{r} - \mathbf{r}', \omega) = \frac{-\mathrm{i}}{|\mathbf{r} - \mathbf{r}'|} \, ,$$

$$G_0(\mathbf{k}, \omega) = \frac{\mathrm{i}}{\omega - \mathbf{k}^2/2 + \mathrm{i}\eta_{\mathbf{k}}}$$
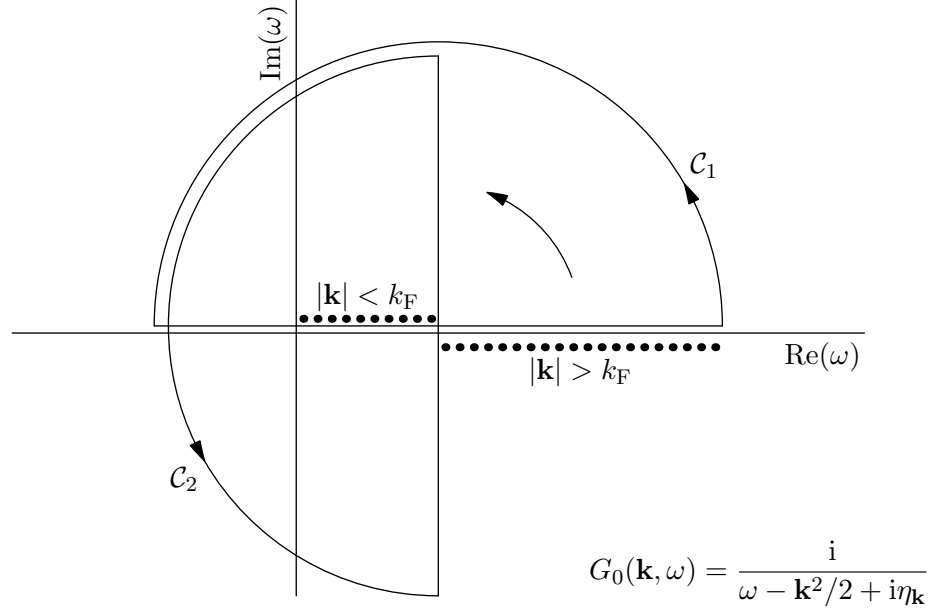
Figure 6.2: $G_0(\omega)$ has one pole above the real axis for $|\mathbf{k}| < k_{\mathrm{F}}$ or below the real axis for $|\mathbf{k}| > k_{\mathrm{F}}$. We can smoothly rotate the integration contour from the real axis to a contour parallel to the imaginary axis without crossing any pole. The arcs indicate the contour at infinity.

omitting the spin coordinates. The transform into momentum space does not converge, however, the propagator for the Yukawa potential can be expressed by a Fourier integral for any parameter $m > 0$:

$$\frac{-\mathrm{i}e^{-m|\mathbf{r}-\mathbf{r}'|}}{|\mathbf{r}-\mathbf{r}'|} = \int \frac{1}{(2\pi)^3}\,\mathrm{d}\mathbf{q}\,e^{\mathrm{i}\mathbf{q}\cdot(\mathbf{r}-\mathbf{r}')}\,\frac{-4\pi\mathrm{i}}{\mathbf{q}^2+m^2} = \int \frac{\Omega}{(2\pi)^3}\,\mathrm{d}\mathbf{q}\,e^{\mathrm{i}\mathbf{q}\cdot(\mathbf{r}-\mathbf{r}')}\,\frac{-4\pi\mathrm{i}}{\Omega(\mathbf{q}^2+m^2)}\,.$$

Taking the limit $m \to 0$ gives the propagator for the Coulomb interaction in momentum space:

$$V(\mathbf{q}, \omega) = -\frac{4\pi\mathrm{i}}{\Omega\mathbf{q}^2}\,. \tag{6.43}$$

Note that we use $\mathbf{k}$ for particle/hole propagators while we use $\mathbf{q}$ for Coulomb propagators. The spin coordinates remain omitted for brevity as the behavior of spin is intuitive in the UEG. A particle or a hole does not change spin during propagation while the Coulomb interaction mediates between particles or holes irrespective of the their spin.

6.4.2 Imaginary frequencies

G_0 has one pole on the positive real frequency axis. The pole is infinitesimally below or above the real axis depending on whether it is a particle, having $|\mathbf{k}| > k_{\mathrm{F}}$, or a hole. On which side of the real axis the pole lies determines whether there is forwards or backwards propagation in time. Figure 6.2 shows the pole of $G_0(\mathbf{k}, \omega)$ as a function of ω with $\mathbf{k}$ as parameter. The poles of the propagators make a numeric frequency integration along the real axis difficult. We can, however, smoothly deform the integration contour as long as we do not cross any

poles. As indicated in Figure 6.2 we can rotate the contour $\mathcal{C}_1$ counterclockwise around the Fermi energy $\mu = k_{\mathrm{F}}^2/2$ to arrive at the contour $\mathcal{C}_2$. Substituting $\omega = \mu + \mathrm{i}\nu$ we get
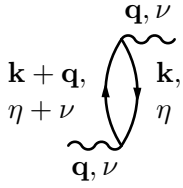
$$\int_{-\infty}^{\infty} \mathrm{d}\omega = \oint_{\mathcal{C}_1} \mathrm{d}\omega = \oint_{\mathcal{C}_2} \mathrm{d}\omega = \int_{-\infty}^{\infty} \mathrm{i}\,\mathrm{d}\nu\,,$$

where we assume that the contribution of a contour at infinity vanishes. This rotation of the integral contour is called *Wick* rotation to *imaginary frequency*. When integrating in imaginary frequency the side of the poles relative to the contour no longer depend on η and we can as well take the limit $\eta \to 0$ before evaluating the imaginary frequency integrals. The particle/hole propagator in imaginary frequency is then given by

$$G_0(\mathbf{k}, \mathrm{i}\nu) = \frac{\mathrm{i}}{\mathrm{i}\nu - (\mathbf{k}^2/2 - \mu)} = \frac{1}{\nu + \mathrm{i}\Delta\varepsilon_{\mathbf{k}}}\,, \quad \text{where } \Delta\varepsilon_{\mathbf{k}} = \mathbf{k}^2/2 - k_{\mathrm{F}}^2/2\,. \tag{6.44}$$

6.4.3   Polarizability

Next, we can evaluate the independent particle polarizability. The polarizability diagram has two open vertices. Let $\mathbf{q}$ and ν denote the momentum and the imaginary frequency incident at the lower vertex shown in the diagram below. From the momentum and frequency conservation at every vertex follows that there is one pair of momentum $\mathbf{k}$ and frequency η to integrate over and that the outgoing momentum and frequency is equal to the incoming ones. In the context of this diagram part $\mathbf{k}$ and η are called *internal* momentum and frequency, respectively, while $\mathbf{q}$ and ν are connected to other diagram parts and are therefore referred to as *external* momentum and frequency, respectively. We evaluate the diagram part by integrating over all internal momenta and frequencies starting with the analytic η integration:

$$\chi_0(\mathbf{q}, \mathrm{i}\nu) = -\sum_\sigma \int \frac{\Omega\,\mathrm{d}\mathbf{k}}{(2\pi)^3} \int \frac{\mathrm{i}\,\mathrm{d}\eta}{2\pi}\, G_0(\mathbf{k}+\mathbf{q}, \mathrm{i}\eta + \mathrm{i}\nu)\, G_0(\mathbf{k}, \mathrm{i}\eta)$$

$$= -\sum_\sigma \int \frac{\Omega\,\mathrm{d}\mathbf{k}}{(2\pi)^3} \int \frac{\mathrm{i}\,\mathrm{d}\eta}{2\pi}\, \frac{1}{\eta + \nu + \mathrm{i}\Delta\varepsilon_{\mathbf{k}+\mathbf{q}}}\, \frac{1}{\eta + \mathrm{i}\Delta\varepsilon_{\mathbf{k}}}$$

$$= -\mathrm{i}\sum_\sigma \int \frac{\Omega\,\mathrm{d}\mathbf{k}}{(2\pi)^3} \left(\frac{\theta(|\mathbf{k}+\mathbf{q}| - k_{\mathrm{F}})\theta(k_{\mathrm{F}} - |\mathbf{k}|)}{\varepsilon_{\mathbf{k}+\mathbf{q}} - \varepsilon_{\mathbf{k}} - \mathrm{i}\nu} \right.$$

$$\left. + \frac{\theta(|\mathbf{k}| - k_{\mathrm{F}})\theta(k_{\mathrm{F}} - |\mathbf{k}+\mathbf{q}|)}{\varepsilon_{\mathbf{k}} - \varepsilon_{\mathbf{k}+\mathbf{q}} + \mathrm{i}\nu} \right) \tag{6.45}$$

The conditions on $\mathbf{k}$ expressed by the Heaviside theta functions arise from the necessity to have one pole on either side of the integration contour for a non-vanishing result. The conditions in (6.45) can be unified by substituting $-\mathbf{k}' = \mathbf{k} + \mathbf{q}$ in the second sum. This gives

$$\chi_0(\mathbf{q}, \mathrm{i}\nu) = -\mathrm{i}\sum_\sigma \int\limits_{|\mathbf{k}| < k_{\mathrm{F}} < |\mathbf{k}+\mathbf{q}|} \frac{\Omega\,\mathrm{d}\mathbf{k}}{(2\pi)^3} \left(\frac{1}{\varepsilon_{\mathbf{k}+\mathbf{q}} - \varepsilon_{\mathbf{k}} - \mathrm{i}\nu} + \frac{1}{\varepsilon_{\mathbf{k}+\mathbf{q}} - \varepsilon_{\mathbf{k}} + \mathrm{i}\nu} \right) \tag{6.46}$$

With effort this expression can also be integrated analytically with respect to the momentum $\mathbf{k}$ and expressed in terms of a real valued function $R(q, u)$ where the Fermi momentum and

the Fermi energy are normalized to 1 and 1/2, respectively (Ziesche 2010):

$$\chi_0(\mathbf{q}, \mathrm{i}\nu) = -\mathrm{i}\,\frac{k_{\mathrm{F}}}{\pi^2}\,R\left(\frac{|\mathbf{q}|}{k_{\mathrm{F}}}, \frac{\nu}{|\mathbf{q}|k_{\mathrm{F}}}\right) \tag{6.47}$$

$$2R(q, u) = 1 - u\left(\arctan\left(\frac{1 + q/2}{u}\right) + \arctan\left(\frac{1 - q/2}{u}\right)\right) \tag{6.48}$$

$$+ \frac{1 + u^2 - q^2/4}{2q}\,\log\left(\frac{u^2 + (q/2 + 1)^2}{u^2 + (q/2 - 1)^2}\right) \tag{6.49}$$

Note that the imaginary units are often traded between the Coulomb kernel $V(\mathbf{q})$ and the polarizability $\chi_0(\mathbf{q}, \mathrm{i}\nu)$ since only their product occurs in the expression for the RPA correlation energy. Throughout this work, except Section 6.3, imaginary units are used exactly as they emerge from Wick rotated imaginary frequency integrations:

$$V(\mathbf{q}) = -\frac{4\pi\mathrm{i}}{\Omega\,\mathbf{q}^2} \qquad \chi(\mathbf{q}, \mathrm{i}\nu) = -\mathrm{i}\sum_{\sigma\mathbf{k}}(\ldots) \qquad \text{used in this work,} \tag{6.50}$$

$$V(\mathbf{q}) = \frac{4\pi}{\Omega\,\mathbf{q}^2} \qquad \chi(\mathbf{q}, \mathrm{i}\nu) = -\sum_{\sigma\mathbf{k}}(\ldots) \qquad \text{also common in literature.} \tag{6.51}$$

6.4.4 Correlation energy

Finally, we can evaluate the correlation energy in the Random Phase Approximation for the uniform electron gas according to (6.9). In the space domain we needed to convolve the propagators connected in series which we denoted by the matrix product. In the momentum domain of a homogeneous system this simplifies to a product. The RPA energy per electron in the uniform electron gas is thus

$$\begin{aligned}E_{\mathrm{c}}^{\mathrm{RPA}}/N &= \frac{\Omega}{N}\frac{1}{2}\int\frac{\mathrm{d}\mathbf{q}}{(2\pi)^3}\int_{-\infty}^{\infty}\frac{\mathrm{d}\nu}{2\pi}\Big\{\log\left(1 - \chi_0(\mathbf{q}, \mathrm{i}\nu)V(\mathbf{q})\right) + \chi_0(\mathbf{q}\mathrm{i}\nu)V(\mathbf{q})\Big\} \\ &= \frac{4\pi r_s^3}{3}\int_0^{\infty}\frac{4\pi q^2\mathrm{d}q}{(2\pi)^3}\int_0^{\infty}\frac{\mathrm{d}\nu}{2\pi}\Big\{\log\left(1 - \chi_0(q, \mathrm{i}\nu)V(q)\right) + \chi_0(q, \mathrm{i}\nu)V(q)\Big\}\end{aligned} \tag{6.52}$$

Note that the sum over all momenta $\mathbf{q}$ of the Coulomb propagator does not include a sum over spins. The given integral can been evaluated using a Gauss–Kronrod rule first in q then in ν to yield the correlation energy in the Random Phase Approximation to 5 significant digits of precision for the non-spin polarized, paramagnetic case with $\sum_\sigma = 2$ and for the spin polarized, ferromagnetic case with $\sum_\sigma = 1$. The results are listed in Table 6.1 for different densities and they include Quantum Monte Carlo results for comparison. Although the RPA systematically overestimates the correlation energy it lacks only about 1/3 of the correlation energy at $r_s = 1$. (Gell-Mann and Brueckner 1957) have shown that in the limit of $r_s \to 0$ the entire correlation energy is contained in the RPA ring diagrams. For low densities, however, the relative error becomes larger and other diagrams become important.

6.4.5 Large momentum behavior

In case of the uniform electron gas the polarizability can be evaluated for an arbitrary magnitude of the momentum transfer q allowing for an accurate numerical integration. For solids

paramagnetic				ferromagnetic			
r_s	E_c^{RPA}		E_c	r_s	E_c^{RPA}		E_c
[a.u.]	[$mE_h\,N$]	$\pm$	[$mE_h\,N$]	[a.u.]	[$mE_h\,N$]	$\pm$	[$mE_h\,N$]
1	-78.799	0.001	-59.632	1	-51.893	0.002	-31.701
2	-61.801	0.001	-45.091	2	-42.416	0.001	-24.090
3	-52.759	<0.001	-37.214	3	-37.179	0.001	-20.048
4	-46.806	<0.001	-32.054	4	-33.633	<0.001	-17.415
5	-42.470	<0.001	-28.339	5	-30.992	<0.001	-15.520
6	-39.117	<0.001	-25.504	6	-28.911	<0.001	-14.071
7	-36.418	<0.001	-23.253	7	-27.209	<0.001	-12.916
8	-34.182	<0.001	-21.414	8	-25.778	<0.001	-11.969
9	-32.289	<0.001	-19.876	9	-24.551	<0.001	-11.174
10	-30.658	<0.001	-18.568	10	-23.482	<0.001	-10.495
12	-27.975	<0.001	-16.454	12	-21.698	<0.001	-9.391
15	-24.929	<0.001	-14.119	15	-19.629	<0.001	-8.160
20	-21.381	<0.001	-11.497	20	-17.156	<0.001	-6.758
30	-17.068	<0.001	-8.486	30	-14.044	<0.001	-5.112
40	-14.463	<0.001	-6.778	40	-12.099	<0.001	-4.156
50	-12.680	<0.001	-5.666	50	-10.736	<0.001	-3.521

Table 6.1: Correlation energy in the Random Phase Approximation for the uniform electron gas at different densities compared to Quantum Monte-Carlo (QMC) results obtained by (Ceperley and Alder 1980) fitted by (Perdew and Zunger 1981). For RPA energies at intermediate spin polarizations see (Vosko, Wilk, and Nusair 1980).

or molecules the finite resolution used for finding the Hartree-Fock or DFT oribitals imposes however an upper limit $G_{\max}$ up to where χ_0 can be evaluated. Therefore, we need to know the asymptotic behavior of the RPA correlation energy for sufficiently large values of $G_{\max}$ in order to extrapolate numerical results to $G_{\max} \to \infty$. Assuming that the system is sufficiently homogeneous at the resolution corresponding to a given $G_{\max}$, the asymptotic behavior of the RPA in a solid or in a molecule is the same as in the uniform electron gas. The latter can be derived analytically and will be outlined here.

Given the expression for the independent particle polarizability χ_0 of the uniform electron gas from (6.46)

$$
\begin{aligned}
\chi_0(\mathbf{q}, \mathrm{i}\nu) &= -\mathrm{i} \sum_{\sigma} \int\limits_{|\mathbf{k}|<k_{\mathrm{F}}<|\mathbf{k}+\mathbf{q}|} \frac{\Omega\,\mathrm{d}\mathbf{k}}{(2\pi)^3} \left(\frac{1}{\varepsilon_{\mathbf{k}+\mathbf{q}} - \varepsilon_{\mathbf{k}} - \mathrm{i}\nu} + \frac{1}{\varepsilon_{\mathbf{k}+\mathbf{q}} - \varepsilon_{\mathbf{k}} + \mathrm{i}\nu} \right) \\
&= -\mathrm{i} \sum_{\sigma} \int\limits_{|\mathbf{k}|<k_{\mathrm{F}}<|\mathbf{k}+\mathbf{q}|} \frac{\Omega\,\mathrm{d}\mathbf{k}}{(2\pi)^3} \frac{\Delta\varepsilon_{\mathbf{k},\mathbf{q}}}{\Delta\varepsilon_{\mathbf{k},\mathbf{q}}^2 + \nu^2}\,,
\end{aligned}
\tag{6.53}
$$

where $\Delta\varepsilon_{\mathbf{k},\mathbf{q}} = \varepsilon_{\mathbf{k}+\mathbf{q}} - \varepsilon_{\mathbf{k}} = \mathbf{k}\cdot\mathbf{q} + \mathbf{q}^2/2$, we can trivially integrate out $\mathbf{k}$ for large enough magnitudes of $\mathbf{q}$ since $|\mathbf{k}| < k_{\mathrm{F}} \ll |\mathbf{q}|$. This yields

$$
\chi_0(q, \mathrm{i}\nu) \sim -\mathrm{i}\,k_{\mathrm{F}}^3\, \frac{q^2}{\left(q^2/2\right)^2 + \nu^2}\,.
\tag{6.54}
$$

Next, we can insert this approximation into the RPA energy expression (6.52) for a given, large q and integrate out the imaginary frequency ν, getting

$$
\begin{aligned}
\int_0^\infty \frac{\mathrm{d}\nu}{2\pi} \left\{ \log\left(1 - \chi_0(q, \mathrm{i}\nu)V(q) \right) + \chi_0(q, \mathrm{i}\nu)V(q) \right\} &\sim \frac{\left(q^2/2\right)\sqrt{\left(q^2/2\right)^2 + 1} - \left(q^2/2\right)^2 - 1/2}{q^2} \\
&= -\frac{1}{q^6} + \frac{1}{q^{10}} + \mathcal{O}\left(\frac{1}{q^{14}}\right),
\end{aligned}
$$

where we expanded in the variable $u = 1/q$ at $u = 0$. The leading order term can finally be used to estimate the missing RPA energy per electron $\Delta E_{\mathrm{c}}^{\mathrm{RPA}}(G_{\max})$ when truncating the momentum integration at a finite momentum $G_{\max}$:

$$
\Delta E_{\mathrm{c}}^{\mathrm{RPA}}(G_{\max}) \sim \int_{G_{\max}}^\infty \mathrm{d}q\, q^2 \left(\frac{1}{q^6} + \mathcal{O}\left(\frac{1}{q^{10}}\right) \right) \sim \frac{1}{G_{\max}^3} + \mathcal{O}\left(\frac{1}{G_{\max}^7}\right).
\tag{6.55}
$$

6.4.6 Large imaginary frequency behavior

Although most implementations of the RPA can evaluate the independent particle polarizability χ_0 at arbitrary imaginary frequencies, knowledge of the asymptotic behavior of the RPA energy for large frequencies ν is useful for choosing an appropriate variable transform for integrating the tail. This is relevant for metallic systems, where we can assume that the system behaves like a Uniform Electron Gas at times short enough.

Unlike in the case of large momenta q, $\mathbf{k}$ cannot be trivially integrated out. However, we can separate the momentum integration of q into three regions and show that they all come to an analogous form of the integrand for that momentum integration. In Subsection 6.4.5
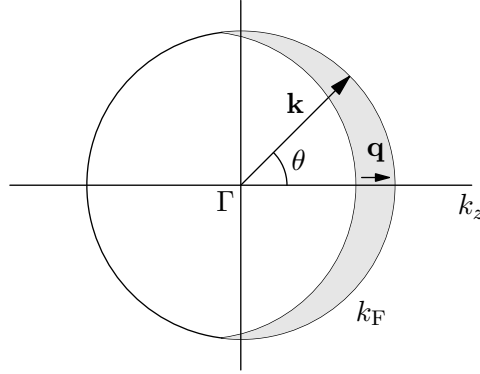
Figure 6.3: Cross section of the set of momenta $\mathbf{k}$ such that $|\mathbf{k}| < k_{\mathrm{F}} < |\mathbf{k} + \mathbf{q}|$ for small magnitudes of the excitation momentum $\mathbf{q}$. In this limit, the set covers half the surface of the Fermi sphere and its maximum thickness is $|\mathbf{q}|$.

we already have gotten an approximation of $\chi_0(q, \mathrm{i}\nu)$ for large q in (6.54). For small q, the volume of the momenta $\mathbf{k}$, such that $|\mathbf{k}| < k_{\mathrm{F}} < |\mathbf{k} + \mathbf{q}|$, is proportional to q, as shown in Figure 6.3. Therefore. the integral in (6.53) transforms as follows

$$
-\mathrm{i} \sum_{\sigma} \int_{|\mathbf{k}| < k_{\mathrm{F}} < |\mathbf{k}+\mathbf{q}|} \frac{\Omega \, \mathrm{d}\mathbf{k}}{(2\pi)^3} \frac{\Delta\varepsilon_{\mathbf{k},\mathbf{q}}}{\Delta\varepsilon_{\mathbf{k},\mathbf{q}}^2 + \nu^2} \sim -\mathrm{i} \, 4\pi k_{\mathrm{F}}^2 \, q \int_0^1 \mathrm{d}\cos\theta \, \cos\theta \, \frac{q^2/2 + k_{\mathrm{F}} q \cos\theta}{(q^2/2 + k_{\mathrm{F}} q \cos\theta)^2 + \nu^2}
$$

$$
\sim -\mathrm{i} \, k_{\mathrm{F}}^2 \frac{q^3/4 + k_{\mathrm{F}} q^2/6}{(q^2/2)^2 + \nu^2} \sim -\mathrm{i} \, k_{\mathrm{F}}^3 \frac{q^2 + \mathcal{O}\left(q^3\right)}{(q^2/2)^2 + \nu^2} \,, \quad (6.56)
$$

where we used that $\Delta\varepsilon_{\mathbf{k},\mathbf{q}} = q^2/2 + k_{\mathrm{F}} q \cos\theta$ and that ν is large compared to $k_{\mathrm{F}} q$. This is the same behavior of $\chi_0(q, \mathrm{i}\nu)$ as for large momenta q. For intermediate q, where the integration volume for $\mathbf{k}$ is roughly independent of $\mathbf{q}$, the $\mathbf{k}$ integration merely averages the contributions to χ_0. For large ν we retrieve

$$
-\mathrm{i} \sum_{\sigma} \int_{|\mathbf{k}| < k_{\mathrm{F}} < |\mathbf{k}+\mathbf{q}|} \frac{\Omega \, \mathrm{d}\mathbf{k}}{(2\pi)^3} \frac{\Delta\varepsilon_{\mathbf{k},\mathbf{q}}}{\Delta\varepsilon_{\mathbf{k},\mathbf{q}}^2 + \nu^2} \sim -\mathrm{i} \, \frac{4\pi k_{\mathrm{F}}^3}{3} \int_{-1}^1 \mathrm{d}\cos\theta \, \frac{q^2/2 + k_{\mathrm{F}} q \cos\theta}{(q^2/2 + k_{\mathrm{F}} q \cos\theta)^2 + \nu^2}
$$

$$
\sim -\mathrm{i} \, k_{\mathrm{F}}^3 \frac{q^2 + \mathcal{O}(q)}{(q^2/2)^2 + \nu^2} \,, \quad (6.57)
$$

Since the integrand has the same form for large ν in all cases, we can use it in the integral over the whole domain of q, getting

$$
\int_0^{\infty} \frac{4\pi q^2 \mathrm{d}q}{(2\pi)^3} \left\{ \log\left(1 - \chi_0(q, \mathrm{i}\nu)V(q)\right) + \chi_0(q, \mathrm{i}\nu)V(q) \right\}
$$

$$
\sim \frac{4\sqrt{\nu}\left(\nu^2 + 1\right)^{3/4} - 4\nu^2 - 3}{6\sqrt{\nu}} = -\frac{1}{16}\frac{1}{\nu^{5/2}} + \frac{5}{192}\frac{1}{\nu^{9/2}} + \mathcal{O}\left(\frac{1}{\nu^{13/2}}\right) \,,
$$

which is expanded in the variable $u = 1/\nu$ at $u = 0$. The other orders in the terms (6.56) and (6.57) yield a leading order term of the form $\mathcal{O}(1/\nu^4)$ for the respective integration region

of q and can therefore be neglected for sufficiently large frequencies ν. These terms can, however, contribute to the next-to-leading order. Finally, we can insert this expansion in the imaginary frequency integration to estimate the missing RPA energy per electron $\Delta E_{\text{c}}^{\text{RPA}}$ when truncating the frequency integration at some finite but large ν_{max}:

$$\Delta E_{\text{c}}^{\text{RPA}} \sim \int_{\nu_{\text{max}}}^{\infty} \mathrm{d}\nu \left(\frac{1}{\nu^{5/2}} + \mathcal{O}\left(\frac{1}{\nu^{9/2}} \right) \right) \sim \frac{1}{\nu_{\text{max}}^{3/2}} + \mathcal{O}\left(\frac{1}{\nu_{\text{max}}^{7/2}} \right). \tag{6.58}$$

Summary

The Random Phase Approximation is the sum of all ring diagrams to infinite order. Momentum conservation dictates that every Coulomb interaction in a ring diagram mediates the same momentum giving rise to a $1/q^{2n}$ divergence in n-th order. This is the strongest divergence possible in n-th order rendering the ring diagrams the most important contribution for low momenta, i.e. at long distances or in the high density regime. The divergence of each diagram when integrating over low momenta is referred to as *infrared catastrophe*. Evaluating the sum over all orders before integrating over the mediated momenta turns the $1/q^{2n}$ divergence of each order into a $\log(1 + 1/q^2)$ divergence, which yields a finite result in the subsequent momentum integration and solves the infrared catastrophe.

Within the framework of many-body perturbation theory, discussed in Chapter 5, the Random Phase Approximation can be readily derived using the independent particle polarizability $\langle\!\rangle = \chi_0$ as a building block. In the frequency domain this can be done using Feynman diagrams where the rotational symmetry of the ring diagrams gives rise to the factors in the expansion of the RPA energy

$$\frac{1}{2} \left(\langle\!\rangle \right)^2 + \frac{1}{3} \left(\langle\!\rangle \right)^3 + \dots$$

The RPA can also be derived in the frequency domain within the Adiabatic Connection (AC) arriving at a formally equivalent result for very different reasons. In many-body perturbation theory the perturbation is slowly introduced to the system leaving it in its ground state. The sum over all connected diagrams, respecting their symmetry, yields the total correlation energy. In the Adiabatic Connection the correlation energy is retrieved from averaging the potential energy over the coupling strength λ:

$$\int_0^1 \mathrm{d}\lambda \left(\lambda \left(\langle\!\rangle \right)^2 + \lambda^2 \left(\langle\!\rangle \right)^3 + \dots \right)$$

In the AC the polarizability χ_λ is the key quantity of interest rather than connected diagrams. Therefore, there are no symmetries to consider and connected (closed) diagrams should be avoided for depicting the RPA within the Adiabatic Connection. It is important to remark that the AC derivation is tailored to a DFT reference system assuming an exact density of the reference for the Adiabatic Connection and an exact density response for the Dyson-like equation of the polarizability.

Finally, the RPA can also be derived in the time domain using Goldstone diagrams and the direct ring Coupled Cluster Doubles amplitudes

$$\bigvee\!\!-\!\!\bigvee.$$

In each iteration of the amplitude equation ring diagrams are added in all possible ways in a time ordered manner. The simple fact that rings have a left and a right side when building them bottom to top requires 4 open connections of this building block according to the left and the right particle/hole pair. Although this approach is not as efficient as calculating the RPA in the imaginary frequency domain, it is easy to include a larger set of diagrams once the amplitudes are found. After all, Wick's theorem requires all contractions to be considered not just the ring diagrams. The additional set of diagrams available given the direct ring Coupled Cluster Doubles amplitudes is called *Second Order Screened Exchange* diagrams. They represent the lowest order correction to the Random Phase Approximation.

Chapter 7

Second Order Screened Exchange

The Random Phase Approximation (RPA) improves considerably on Hartree-Fock or Density Functional Theory results. It is capable of describing van der Waals interactions and works well in a large variety of chemical environments. However, it is biased and tends to overestimate the negative correlation energy. In the previous chapter we have seen that for the uniform electron gas but this has also been shown for various solids and molecules. It is not surprising that the Random Phase Approximation shows an error. Wick's theorem states that all contractions should be considered not just those forming the ring diagrams. That the RPA exhibits a systematic error, however, indicates a general reason behind this error which can serve as a guide to the next class of diagrams partially correcting RPA's bias.

In second order the overestimation of the correlation energy is more evident. According Figure 5.5 the second order (MP2) direct term is negative and reads

$$(-1)^{(2+2)}\frac{1}{2}\sum_{ijab}\frac{V_{ij}^{ab}V_{ab}^{ij}}{\varepsilon_i + \varepsilon_j - \varepsilon_a - \varepsilon_b}\,,$$

where the Fermion sign is explicitly given depending on the number of loops and holes according to (5.38). This term contains contributions in violations of the Pauli exclusion principle, for instance as illustrated below on the left, where the state i occurs twice at the same instance in time. Such contributions are canceled exactly by the respective *exchange diagram* where the two offending states are crossed by anti-symmetrizing the affected interaction as shown on the right. The resulting diagram has one loop less giving an opposite sign:

$$(-1)^{(2+2)}\frac{1}{2}\frac{V_{ii}^{ab}V_{ab}^{ii}}{\varepsilon_i + \varepsilon_i - \varepsilon_a - \varepsilon_b} = -\left\{(-1)^{(1+2)}\frac{1}{2}\frac{V_{ii}^{ab}V_{ab}^{ii}}{\varepsilon_i + \varepsilon_i - \varepsilon_a - \varepsilon_b}\right\}$$

As a consequence, violating contributions would be canceled if all contractions were considered. Ignoring this exchange diagram leaves the violating negative contributions uncanceled resulting in a negative error. For the RPA the sign of the ring diagrams alternates with the order. However, the contributions of each order decay such that the error of the lowest order dominates, which is negative.
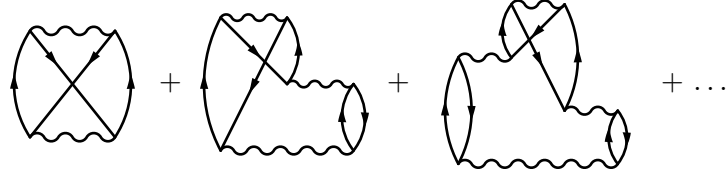
Figure 7.1: Exchanging only the last interaction in the ring diagrams leads to the Second Order Screened Exchange (SOSEX) correction to the Random Phase Approximation.

The systematic error can be alleviated by including exchange diagrams where violations of the Pauli exclusion principle can occur. The lowest order correction to the Random Phase Approximation anti-symmetrizes only one interaction of the RPA ring diagrams. The correction is termed *Second Order Screened Exchange (SOSEX)* if only the last interaction in time is anti-symmetrized. Figure 7.1 shows the additional diagrams included in the SOSEX.

7.1   SOSEX from Direct Ring Coupled Cluster Doubles

The lowest order correction anti-symmetrizes only one interaction of the RPA ring diagrams. This could be any interaction and not necessarily just the last one. However, when calculating the Random Phase Approximation using the direct ring Coupled Cluster Doubles amplitudes t_{ij}^{ab}, as discussed in Section 6.2, calculating the SOSEX corrections comes with hardly any additional costs. We simply close the amplitudes once with a direct interaction V_{ab}^{ij} and once with two indices swapped. Respecting the Fermion sign the RPA+SOSEX energy is then given by

$$\text{} \quad = \quad \frac{1}{2} \sum_{ijab} t_{ij}^{ab} V_{ab}^{ij} - t_{ij}^{ab} V_{ab}^{ji} . \tag{7.1}$$

The Second Order Screened Exchange correction to the RPA was introduced by (Freeman 1977) who applied it to the uniform electron gas. The term SOSEX was later coined by (Grüneis et al. 2009) who studied this correction also for solids. Figure 7.2 shows the Second Order Screened Exchange correction per electron for the uniform electron gas as calculated by Freeman. The error of the Random Phase Approximation with respect to Quantum Monte-Carlo (QMC) results of (Ceperley and Alder 1980) fitted by (Perdew and Zunger 1981) is also given. Remarkably and certainly fortuitously RPA+SOSEX matches the QMC results at $r_s \approx$ 5, which is in the density region of real metals. Anti-symmetrizing only the last interaction seems gives just the right correction to the RPA in the uniform electron gas. However, from a strictly *ab-initio* point of view, there is no reason to restrict the exchange diagrams to those where only the last interaction is anti-symmetrized, except technical convenience when having the drCCD amplitudes at hand.

Anti-symmetrizing each but still only one interaction in the ring diagrams gives worse agreement with QMC in the high density regime $r_s \leq 8$ but better agreement for low densities, where correlation effects are stronger. This is shown in Section 8.2. Note that in a spin-polarized system SOSEX is less fortunate. While still improving on RPA in the density range of interest, it cancels the RPA energy in the low density limit, as discussed in Subsection
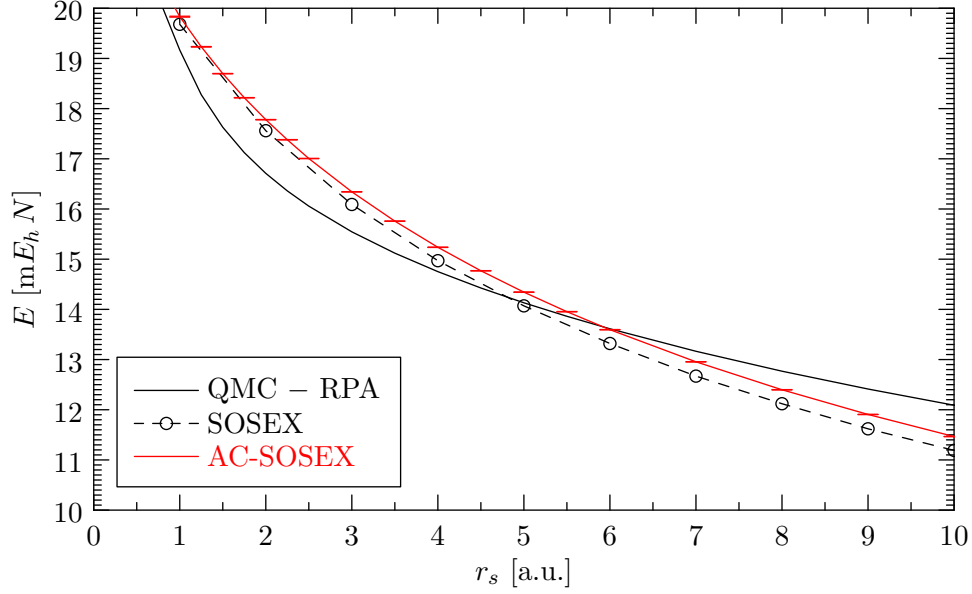
Figure 7.2: The Second Order Screened Exchange energy per electron obtained by (Freeman 1977) for the uniform electron gas. It is compared to the error of the Random Phase Approximation with respect to Quantum Monte-Carlo (QMC) calculations by (Ceperley and Alder 1980) fitted by (Perdew and Zunger 1981). At $r_s \approx 5$ RPA+SOSEX fortuitously matches QMC results. The Adiabatic Connection-SOSEX according to (7.16), which is discussed later, is also shown here.

r_s [a.u.]	$(E_c - E_c^{RPA})$ [mE_h N]	E_c^{SOSEX} [mE_h N]	$E_c^{AC-SOSEX}$ [mE_h N]	$\pm$
1	19.167	19.680	19.832	0.009
2	16.710	17.560	17.780	0.003
3	15.545	16.090	16.342	0.003
4	14.752	14.970	15.237	0.003
5	14.131	14.070	14.343	0.003
6	13.613	13.320	13.595	0.003
7	13.165	12.670	12.955	0.003
8	12.768	12.120	12.398	0.003
9	12.413	11.620	11.906	0.003
10	12.090	11.190	11.466	0.003
12	11.521	—	10.712	0.003
15	10.810	—	9.806	0.003
20	9.884	—	8.679	0.003
30	8.582	—	7.201	0.003
40	7.685	—	6.246	0.003
50	7.014	—	5.564	0.003

Table 7.1: Data of Figure 7.2 including low densities.

8.2.3.

One can also include full anti-symmetrization in the amplitude equation, including terms such as
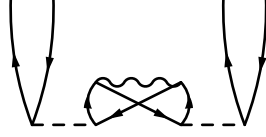
which lead to the full Coupled Cluster Doubles (CCD) amplitude equation. However, calculating the CCD amplitudes requires $\mathcal{O}(N^6)$ operations while the direct ring CCD amplitudes of RPA and SOSEX can be computed in $\mathcal{O}(N^5)$ steps (Scuseria and Schaefer 1989). A major drawback of either method is the large memory requirement scaling like $\mathcal{O}(N^4)$ since the amplitudes t_{ij}^{ab} need to be stored for iterating the amplitude equation.

7.2   Adiabatic Connection-SOSEX

In contrast to calculating the drCCD amplitudes, evaluating the Random Phase Approximation in the frequency domain only requires $\mathcal{O}(N^2)$ memory. Calculating an exchange correction based on two point quantities, such as the independent particle polarizability $\langle\!\rangle = \chi_0$ would therefore be favorable. Ángýan *et al.* suggested an approximation to the drCCD SOSEX within the framework of the Adiabatic Connection that can be implemented with a memory usage of $\mathcal{O}(N^2)$, which we will outline here.

Within the Adiabatic Connection one can define a screened interaction similar to the one defined in many-body perturbation theory in (6.7)

$$\mathbf{W}_\lambda(\mathrm{i}\nu) = \lambda\mathbf{V} + \lambda^2\mathbf{V}\mathbf{X}_0(\mathrm{i}\nu)\mathbf{V} + \lambda^3\mathbf{V}\mathbf{X}_0(\mathrm{i}\nu)\mathbf{V}\mathbf{X}_0(\mathrm{i}\nu)\mathbf{V} + \dots \tag{7.2}$$

using the matrix notation introduced in Section 6.1. The only difference to (6.7) is the dependence on the coupling strength λ. Note that we explicitly write the coupling strength in all diagrams within the Adiabatic Connection to make a clear distinction from the diagrams within many-body perturbation theory discussed in Chapter 5.

We can now define the coupling strength averaged screened interaction

$$\overline{\mathbf{W}}(\mathrm{i}\nu) = \int_0^1 \mathrm{d}\lambda\,\mathbf{W}_\lambda(\mathrm{i}\nu) = \frac{1}{2}\mathbf{V} + \frac{1}{3}\mathbf{V}\mathbf{X}_0(\mathrm{i}\nu)\mathbf{V} + \dots$$

and write the RPA correlation energy found in (6.34) in terms of $\overline{\mathbf{W}}$:

$$E_\mathrm{c}^{\mathrm{RPA}} = -\frac{1}{2}\int\frac{\mathrm{d}\nu}{2\pi}\,\mathrm{tr}\Big\{\mathbf{X}_0(\mathrm{i}\nu)\mathbf{V}\mathbf{X}_0(\mathrm{i}\nu)\overline{\mathbf{W}}(\mathrm{i}\nu)\Big\}. \tag{7.3}$$

Next, we insert the independent particle polarizability given in (6.28),

$$\mathbf{X}_{0\mathbf{x}\mathbf{x}'}(\mathrm{i}\nu) = -\sum_{ia}\left(\frac{\psi_a(\mathbf{x})\psi_a^*(\mathbf{x}')\psi_i(\mathbf{x}')\psi_i^*(\mathbf{x})}{\varepsilon_a - \varepsilon_i - \mathrm{i}\nu} + \frac{\psi_i(\mathbf{x})\psi_i^*(\mathbf{x}')\psi_a(\mathbf{x}')\psi_a^*(\mathbf{x})}{\varepsilon_a - \varepsilon_i + \mathrm{i}\nu}\right),$$

into (7.3), giving

$$
E_c^{\mathrm{RPA}} = -\frac{1}{2} \int \frac{\mathrm{d}\nu}{2\pi} \sum_{ijab} \left(\frac{V_{ib}^{aj}\, \overline{W}_{ja}^{bi}(\mathrm{i}\nu)}{(\varepsilon_a - \varepsilon_i - \mathrm{i}\nu)(\varepsilon_b - \varepsilon_j - \mathrm{i}\nu)} + \frac{V_{ij}^{ab}\, \overline{W}_{ba}^{ji}(\mathrm{i}\nu)}{(\varepsilon_a - \varepsilon_i - \mathrm{i}\nu)(\varepsilon_b - \varepsilon_j + \mathrm{i}\nu)} + \right.
$$
$$
\left. \frac{V_{ab}^{ij}\, \overline{W}_{ji}^{ba}(\mathrm{i}\nu)}{(\varepsilon_a - \varepsilon_i + \mathrm{i}\nu)(\varepsilon_b - \varepsilon_j - \mathrm{i}\nu)} + \frac{V_{aj}^{ib}\, \overline{W}_{bi}^{ja}(\mathrm{i}\nu)}{(\varepsilon_a - \varepsilon_i + \mathrm{i}\nu)(\varepsilon_b - \varepsilon_j + \mathrm{i}\nu)} \right), \quad (7.4)
$$

where we write $\overline{W}_{sr}^{pq}$ analogous to the matrix elements V_{sr}^{pq} of the Coulomb operator:

$$
\overline{W}_{sr}^{pq}(\mathrm{i}\nu) = \iint \mathrm{d}\mathbf{x}_1\, \mathrm{d}\mathbf{x}_2\, \psi_p^*(\mathbf{x}_1)\psi_q^*(\mathbf{x}_2)\, \overline{W}_{\mathbf{x}_1\mathbf{x}_2}(\mathrm{i}\nu)\, \psi_r(\mathbf{x}_2)\psi_s(\mathbf{x}_1).
$$

Although in the Adiabatic Connection the polarizability is the central quantity of interest rather than connected diagrams, we can use similar diagrams to depict the terms in (7.4):

The diagrams are drawn such that the imaginary frequency ν goes from right to left on the Coulomb interaction as indicated by the arrow.

For real valued spin-orbitals $\psi_p(\mathbf{x})$ the Coulomb integrals exhibit time reversal symmetry at each vertex such that $V_{ij}^{ab} = V_{ib}^{aj} = V_{aj}^{ib} = V_{ab}^{ij}$. The same holds for the screened Coulomb integrals since the independent particle polarizability $\mathbf{X}_0(\mathrm{i}\nu)$ is real valued. This simplifies (7.4) to

$$
E_c^{\mathrm{RPA}} = -\frac{1}{2} \int \frac{\mathrm{d}\nu}{2\pi} \sum_{ijab} V_{ab}^{ij}\overline{W}_{ji}^{ba}(\mathrm{i}\nu) f_{ia}(\mathrm{i}\nu) f_{jb}(\mathrm{i}\nu), \qquad \text{with } f_{ia}(\mathrm{i}\nu) = \frac{2(\varepsilon_a - \varepsilon_i)}{(\varepsilon_a - \varepsilon_i)^2 + \nu^2}.
$$

In this form, the frequency dependent RPA energy expression bears resemblance to the drCCD RPA expression $\frac{1}{2}\sum_{ijab} t_{ij}^{ab}V_{ab}^{ij}$ and we can define the *AC-SOSEX* by anti-symmetrizing the Coulomb interaction V in analogy to the drCCD SOSEX expression, arriving at

$$
E_c^{\mathrm{AC-SOSEX}} = +\frac{1}{2} \int \frac{\mathrm{d}\nu}{2\pi} \sum_{ijab} V_{ab}^{ji}\overline{W}_{ij}^{ab}(\mathrm{i}\nu) f_{ia}(\mathrm{i}\nu) f_{jb}(\mathrm{i}\nu). \qquad (7.6)
$$

Above equation still requires $\mathcal{O}(N^4)$ of memory from the two interactions V_{ab}^{ij} and $\overline{W}_{ij}^{ab}$. We can, however, transform it back into the position basis as discussed in Section 5.7, giving

$$
E_c^{\mathrm{AC-SOSEX}} = -\frac{1}{2} \int \frac{\mathrm{d}\nu}{2\pi} \operatorname{tr}\left\{ \mathbf{P}_x^{\mathrm{AC}}(\mathrm{i}\nu)\overline{\mathbf{W}}(\mathrm{i}\nu) \right\}
$$

defining the imaginary frequency dependent exchange polarizability for the AC-SOSEX
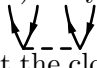
$$
\mathbf{P}_x^{\mathrm{AC}}{}_{\mathbf{x}_1\mathbf{x}_2}(\mathrm{i}\nu) = -\iint \mathrm{d}\mathbf{x}_3\, \mathrm{d}\mathbf{x}_4\, \frac{1}{|\mathbf{r}_3 - \mathbf{r}_4|} \sum_{ia} \psi_i^*(\mathbf{x}_4)\psi_i(\mathbf{x}_1)\psi_a^*(\mathbf{x}_1)\psi_a(\mathbf{x}_3) f_{ia}(\mathrm{i}\nu)
$$
$$
\sum_{jb} \psi_j^*(\mathbf{x}_3)\psi_j(\mathbf{x}_2)\psi_b^*(\mathbf{x}_2)\psi_b(\mathbf{x}_4) f_{jb}(\mathrm{i}\nu). \qquad (7.7)
$$

Note that the exchange polarizability is defined negative since it contains only one Fermion loop. We can give a closed form for the coupling strength averaged screened interaction finding a matrix function with the same Taylor expansion. This yields the final expression for the AC-SOSEX:

$$E_c^{\text{AC−SOSEX}} = +\frac{1}{2} \int \frac{\mathrm{d}\nu}{2\pi} \, \mathrm{tr} \left\{ \mathbf{P}_x^{\text{AC}}(\mathrm{i}\nu) \Big(\mathbf{X}_0(\mathrm{i}\nu) \mathbf{V} \mathbf{X}_0(\mathrm{i}\nu) \Big)^{-1} \Big(\log \Big(\mathbf{1} - \mathbf{X}_0(\mathrm{i}\nu) \mathbf{V} \Big) + \mathbf{X}_0(\mathrm{i}\nu) \mathbf{V} \Big) \right\} .$$
(7.8)

The exchange polarizability is a quantity depending on two positions. Thus, evaluating the AC-SOSEX as given above requires only $\mathcal{O}(N^2)$ of memory rather than $\mathcal{O}(N^4)$, greatly broadening the applicability of the AC-SOSEX to larger systems. However, calculating the exchange polarizability still requires $\mathcal{O}(N^5)$ steps, which is equally time consuming as calculating the SOSEX from the direct ring Coupled Cluster Doubles amplitudes. In the Random Phase Approximation the respective polarizability analogous to $\mathbf{P}_x^{\text{AC}}(\mathrm{i}\nu)$ simply factors into $\mathbf{X}_0(\mathrm{i}\nu) \mathbf{V} \mathbf{X}_0(\mathrm{i}\nu)$, allowing for an evaluation in only $\mathcal{O}(N^3)$ steps. This can not be done for the AC-SOSEX since $\mathbf{x}_3$ and $\mathbf{x}_4$ occur in both sums in (7.7). Reducing the memory consumption from $\mathcal{O}(N^4)$ to $\mathcal{O}(N^4)$ is still an important improvement since it is easier to allocate more CPUs to a calculation than it is to allocate more memory per CPU.

7.3   Difference between drCCD SOSEX and AC-SOSEX

Despite the similarity of (7.6) and the expression for the drCCD SOSEX (7.1) they are only identical in second order but not beyond. First, the drCCD amplitudes are constructed monotonous in time according to (6.13)-(6.16), which guarantees that the closing Coulomb interaction in

is indeed the last interaction in time. In contrast, the averaged screened interaction $\overline{\mathbf{W}}(\mathrm{i}\nu)$ contains interactions that reach both, in the past and in the future. Thus, the left diagram shown in Figure 7.3 is contained in the AC-SOSEX while it is not contained in the drCCD SOSEX. Furthermore, anti-symmetrizing the first and the last case in (7.5) yields terms that have no correspondence in many-body perturbation theory. The AC-SOSEX introduces anti-symmetrization by simply swapping i and j at the unscreened interaction V. For the last term this yields for example

$$V_{ai}^{jb} \overline{W}_{bi}^{ja} \, .$$

This term, however, contradicts the requirement of many-body perturbation theory that upper indices can only match lower indices and vice-versa since upper and lower indices refer to creation and annihilation operators, respectively. This term can therefore not be drawn diagrammatically in the usual manner such that the upper/lower indices correspond to outgoing/incoming connections. We can, however, draw the term respecting the propagation direction of particles and holes. The resulting diagram is depicted on the right of Figure 7.3. It exhibits a particle a turning into a hole j at the left vertex of the Coulomb interaction and a hole i turning into a particle b at the right vertex. This diagram will be termed *swapped ladder diagram* since it resembles a particle-hole ladder diagram where b and j are swapped. Employing the same notion of diagrams as in (7.5), the AC-SOSEX can be depicted
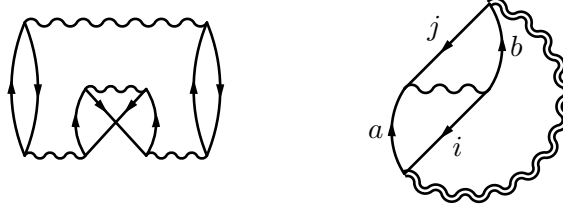
Figure 7.3: Diagrams contained in the AC-SOSEX that are not part of the SOSEX based on the drCCD amplitudes. The factors from the coupling strength integration are omitted. The right diagram shows a particle turning into a hole and vice-versa, which has no correspondence in many-body perturbation theory.

diagrammatically by

$$E_\text{c}^\text{AC-SOSEX} = +\frac{1}{2}\left(\text{} \right).$$

(7.9)

7.3.1 Diamond C(A4)

We can study the swapped ladder diagram for a small test system consisting of diamond C(A4) with 128 states. It is based on a Hartree-Fock reference with $2\times2\times2$ k-points in a primitive cell comprising 2 atoms with 4 electrons per atom. Although the system is only coarsely described by 128 states it serves well as a benchmark for individual diagrams beyond second order. In this finite band gap system we can limit the order of the AC-SOSEX diagrams from (7.9) solely to third order while still getting finite results. This excludes all diagrams that are not contained in the drCCD SOSEX except the third order swapped ladder diagram. The AC-SOSEX expression from (7.9) expands in third order to all possible permutations of the interaction times, analogous to Figure 5.9. Including the factor 1/3 from the coupling strength integration this gives

$$E_\text{c}^\text{AC-SOSEX(3)} = \frac{1}{2\cdot3}\left(\text{} \right).$$

(7.10)

The lower diagrams are equivalent to the upper diagrams since each can be continuously deformed into the respective upper diagram without changing the order of the Coulomb interactions. The left two and the right two diagrams are identical due to time reversal symmetry. This leaves two diagrams with distinct energies to evaluate, the exchange diagram

and the swapped ladder diagram:

 $= (-1)^{2+3} \sum\limits_{ijkabc} \dfrac{V_{ab}^{ji} V_{ik}^{ac} V_{jc}^{bk}}{(\varepsilon_i + \varepsilon_k - \varepsilon_a - \varepsilon_c)(\varepsilon_i + \varepsilon_j - \varepsilon_a - \varepsilon_b)} = -1.151\,\mathrm{m}E_h\,N$

$$(7.11)$$

 $= (-1)^{2+3} \sum\limits_{ijkabc} \dfrac{V_{ai}^{jb} V_{ik}^{ac} V_{bc}^{jk}}{(\varepsilon_i + \varepsilon_k - \varepsilon_a - \varepsilon_c)(\varepsilon_j + \varepsilon_k - \varepsilon_b - \varepsilon_c)} = -1.141\,\mathrm{m}E_h\,N$

$$(7.12)$$

Although the denominators differ, they yield almost the same energy per electron. Thus, the AC-SOSEX energy for the test system in third order hardly differs from the drCCD SOSEX energy in third order. The latter is simply given by the exchange diagram in (7.11):

$$E_{\mathrm{c}}^{\mathrm{AC-SOSEX}(3)} = -\frac{1}{3}\big(2 \cdot 1.151 + 1.141\big) = -1.148\,\mathrm{m}E_h\,N$$

$$E_{\mathrm{c}}^{\mathrm{SOSEX}(3)} = -1.151\,\mathrm{m}E_h\,N$$

In fourth order, the AC-SOSEX expression from (7.9) expands to 24 possible permutations of the interaction times, 12 of which are distinct Goldstone diagrams. This cancels the factor $1/2$ of (7.9). The factor from the coupling strength integration is $1/4$, giving

$$E_{\mathrm{c}}^{\mathrm{AC-SOSEX}(4)} = \frac{1}{4}\Bigg(\quad$$

where $t.r.$ denotes the time reversed variants of the shown 6 diagrams. Note that the diagrams are drawn such that the permutations of the interaction times are evident and not according to minimal self intersection. The diagrams can be evaluated by iterating the doubles amplitudes t_{ij}^{ab} employing only a subset of the direct ring Coupled Cluster Doubles amplitude equations. The following steps are for instance used to calculate the second diagram in (7.13) indicating

the employed part of the drCCD amplitude equation above each equals sign:

$$t^{(0)} \qquad t_{ij}^{ab(0)} \stackrel{(6.13)}{=} \frac{V_{ij}^{ab}}{\varepsilon_i + \varepsilon_j - \varepsilon_a - \varepsilon_b}$$

$$t^{(1)} \qquad t_{ij}^{ab(1)} \stackrel{(6.16)}{=} \frac{\sum_{klcd} t_{ik}^{ac(0)} V_{cd}^{kl} t_{lj}^{db(0)}}{\varepsilon_i + \varepsilon_j - \varepsilon_a - \varepsilon_b}$$

$$t^{(1)} \qquad \stackrel{(7.1)}{=} -\frac{1}{2} \sum_{ijab} t_{ij}^{ab(1)} V_{ab}^{ji} \,.$$

Evaluating the second row of diagrams in (7.13) requires two additional parts of the doubles amplitude equation that are not part of the drCCD amplitude equation:

$$t = 0 \qquad t_{ij}^{ab} = \frac{-\sum_{kc} V_{ia}^{ck} t_{kj}^{cb}}{\varepsilon_i + \varepsilon_j - \varepsilon_a - \varepsilon_b} \qquad (7.14)$$

$$t = 0 \qquad t_{ij}^{ab} = \frac{-\sum_{klcd} t_{ik}^{ac} V_{cd}^{lk} t_{lj}^{db}}{\varepsilon_i + \varepsilon_j - \varepsilon_a - \varepsilon_b} \qquad (7.15)$$

In the case of the swapped ladder amplitude equation (7.14) there is one additional hole k but no additional loop, resulting in a negative sign. In the exchange amplitude equation (7.15) there are two additional holes and one additional loop also giving a negative sign. The latter is part of the full Coupled Cluster Doubles (CCD) amplitude equations while the swapped ladder equation only occurs in the AC-SOSEX. Table 7.2 lists the energies per electron of all diagrams of the AC-SOSEX in third and fourth order modulo time reversal symmetry. The AC-SOSEX energy in fourth order is thus

$$E_{\text{c}}^{\text{AC–SOSEX}(4)} = \frac{1}{2}\big(0.212 + 0.105 + 0.208 + 0.208 + 0.103 + 0.209\big) = +0.522 \,\text{m}E_h\, N \,.$$

The drCCD SOSEX energy is formed by the diagrams of the first row in Table 7.2 only, yielding a very similar result:

$$E_{\text{c}}^{\text{SOSEX}(4)} = 0.212 + 0.105 + 0.208 = +0.525 \,\text{m}E_h\, N \,.$$

The top row in Table 7.2 shows diagrams where the last interaction is anti-symmetrized while in the second row it is the second last interaction that is anti-symmetrized. The table indicates that the energy of the SOSEX or AC-SOSEX diagrams hardly depends on which of the interactions is anti-symmetrized when using the swapped ladder diagram instead of the
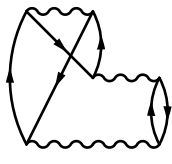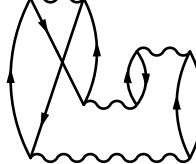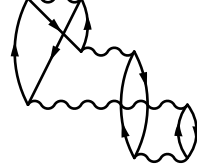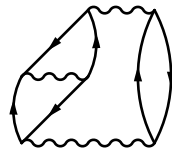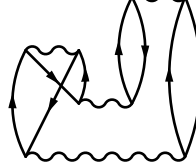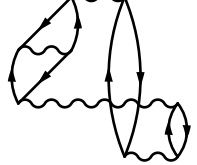
C(A4)	3$^{\text{rd}}$ order	4$^{\text{th}}$ order		
		(a)	(b)	(c)
SOSEX				
$E\ [\text{m}E_h\,N]$	-1.151	$+0.212$	$+0.105$	$+0.208$
AC-SOSEX				
$E\ [\text{m}E_h\,N]$	-1.141	$+0.208$	$+0.103$	$+0.209$

Table 7.2: Goldstone diagrams forming the third and the fourth order of the drCCD SOSEX and the AC-SOSEX correction. The drCCD SOSEX consists of diagrams of the first row only. A weighted average of the first and second row yields the AC-SOSEX energy.

proper ladder diagram. Finally, the factor $1/n$ from the coupling strength integration simply averages the energies from anti-symmetrizing each of the n interactions, as shown in (7.10) for third order and in (7.13) for fourth order. Since the energies of the diagrams are very similar anti-symmetrizing each of the n interactions, the average is also very similar to the energy of the diagrams where only the last interaction is anti-symmetrized. The averaged energy forms the AC-SOSEX energy while the latter forms the drCCD SOSEX originally proposed by Freeman. This argument holds at least up to fourth order in the diamond test system and the truncation at fourth order describes the drCCD SOSEX already to an accuracy of 5%.

7.3.2 Uniform electron gas

In a metallic system it is not possible to truncate the AC-SOSEX expression at any finite order beyond the second order since all of the described higher order exchange diagrams diverge. It is, however, possible to study the AC-SOSEX diagrams of (7.9) numerically for the uniform electron gas (UEG) as the prototypical metal. In the UEG we let spin and momenta denote the states i, j, a and b occurring in the diagrams. For the third and the fourth diagram of (7.9) we choose for instance the following definition of momenta:
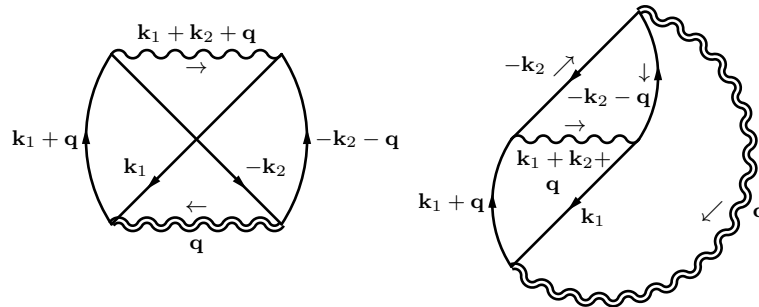
$\mathbf{k}_1$ and $-\mathbf{k}_2$ are required to be hole states while $\mathbf{k}_1 + \mathbf{q}$ and $-\mathbf{k}_2 - \mathbf{q}$ must be particle states. Thus, $\mathbf{k}_i$ must be below and $\mathbf{k}_i + \mathbf{q}$ must be above the Fermi momentum k_F for $i \in \{1, 2\}$. Note that in the swapped ladder diagram on the right the momenta $-\mathbf{k}_2$ and $-\mathbf{k}_2 - \mathbf{q}$ are defined opposite to the propagation directions of the respective states, as indicated by the arrows next to the labels. The spins of all four states must be the same. In the UEG the sum over the states is replaced by the sum over the spin and integrals over all internal momenta according to (6.38), arriving at

$$E_c^{\text{AC-SOSEX}} = +\frac{\Omega}{N}\frac{1}{2}\int\frac{\mathrm{d}\nu}{2\pi}\int\frac{\mathrm{d}\mathbf{q}}{(2\pi)^3}\sum_{\sigma}\iint_{|\mathbf{k}_i|<k_F<|\mathbf{k}_i+\mathbf{q}|}\frac{\Omega^2\mathrm{d}\mathbf{k}_1\mathrm{d}\mathbf{k}_2}{(2\pi)^6}V(\mathbf{k}_1+\mathbf{k}_2+\mathbf{q})\overline{W}(\mathbf{q},\nu)$$
$$\left(\frac{1}{(\Delta\varepsilon_{\mathbf{k}_1,\mathbf{q}}-\mathrm{i}\nu)(\Delta\varepsilon_{-\mathbf{k}_2,-\mathbf{q}}-\mathrm{i}\nu)}+\frac{1}{(\Delta\varepsilon_{\mathbf{k}_1,\mathbf{q}}-\mathrm{i}\nu)(\Delta\varepsilon_{-\mathbf{k}_2,-\mathbf{q}}+\mathrm{i}\nu)}+\right.$$
$$\left.\frac{1}{(\Delta\varepsilon_{\mathbf{k}_1,\mathbf{q}}+\mathrm{i}\nu)(\Delta\varepsilon_{-\mathbf{k}_2,-\mathbf{q}}-\mathrm{i}\nu)}+\frac{1}{(\Delta\varepsilon_{\mathbf{k}_1,\mathbf{q}}+\mathrm{i}\nu)(\Delta\varepsilon_{-\mathbf{k}_2,-\mathbf{q}}+\mathrm{i}\nu)}\right),\quad(7.16)$$

with $i \in \{1, 2\}$ and the single particle excitation energy $\Delta\varepsilon_{\mathbf{k}_i,\mathbf{q}} = (\mathbf{k}_i + \mathbf{q})^2/2 - \mathbf{k}_i^2/2$. The same expression can be derived using imaginary frequency propagators defined in (6.44) and integrating out the two additional imaginary frequencies analogous to the derivation of χ_0 in (6.45).

Integrating out $\mathbf{k}_1$ and $\mathbf{k}_2$ turns out to be a tedious task for the above equation. Although there are closed expressions for the second and the third case they are overly complicated. For the swapped ladder diagrams in the first and the fourth case no such expressions were found. However, a straight-forward Monte-Carlo integration of $\mathbf{k}_1$ and $\mathbf{k}_2$ has proven to be sufficiently accurate when sampling the momenta $\mathbf{k}_i$ with a probability density function (PDF) given by

$$\text{PDF}(\mathbf{k}_i) \propto \begin{cases} \left|\dfrac{1}{\Delta\varepsilon_{\mathbf{k}_i,\mathbf{q}}\pm\mathrm{i}\nu}\right| & \text{for } |\mathbf{k}_i| < k_F < |\mathbf{k}_i + \mathbf{q}|, \\ 0 & \text{otherwise.} \end{cases}$$

Figure 7.2 and Table 7.1 show the resulting AC-SOSEX energies as a function of density given by the Wigner-Seitz radius, r_s. The uncertainties from the integrations are indicated by the error bars. For the Monte-Carlo integration of $\mathbf{k}_1$ and $\mathbf{k}_2$ a precision of 5 significant digits can be achieved with less than 30000 samples for each q and ν, depending on momentum, frequency and density. The error from the momentum and imaginary frequency integration is of similar magnitude.

The differences between the two SOSEX variants are not as small as for an isolating system but they are still below 3% for the density range with $r_s \leq 10$. For lower densities no drCCD SOSEX reference values were found.

Summary

The Random Phase Approximation (RPA) systematically overestimates the negative correlation energy. This originates, at least partially, from violations of the Pauli exclusion principle in the ring diagrams of the RPA such as
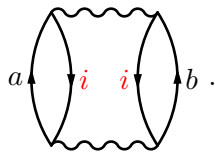
By the merit of Wick's theorem, violations of the Pauli exclusion principle do not have to be considered as long as all contractions of the occurring operators are included. The contractions correcting these violations are those from the respective exchange diagrams where the offending states are crossed by anti-symmetrizing an affected Coulomb interaction.

Thus, the lowest order correction to the Random Phase Approximation anti-symmetrizes one Coulomb interaction occurring in the ring diagrams. If this interaction is the last interaction in time the respective correction is termed Second Order Screened Exchange (SOSEX) containing the following diagrams:
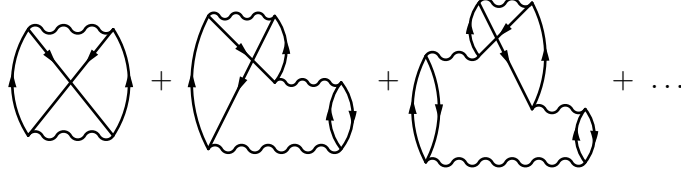
The SOSEX can only be computed from the direct ring Coupled Cluster Doubles (drCCD) amplitudes since monotonicity in time is required to be able to anti-symmetrize only the last interaction. When calculating the RPA using the drCCD amplitudes the SOSEX can be easily computed with hardly any additional costs. However, calculating the drCCD amplitudes requires $\mathcal{O}(N^4)$ of memory limiting the applicability of RPA+SOSEX to rather small systems.

To overcome the limitations regarding memory consumption the Adiabatic-Connection (AC) SOSEX can be used requiring only $\mathcal{O}(N^2)$ of memory. It yields very similar results compared to the SOSEX although it contains terms that have no correspondence in many-body perturbation theory where particles turn into holes and vice-versa herein called swapped ladder diagrams. This is due to the numerical oddity that it hardly matters which of the n occurring interactions in n-th order are anti-symmetrized as long as the swapped ladder diagrams are used rather than actual ladder diagrams. In third order this means for instance:
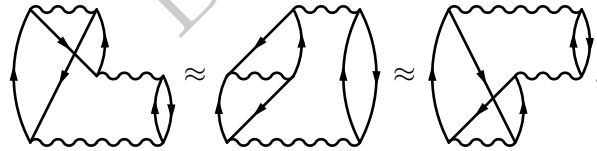
such that

Thus, the AC-SOSEX can be considered a recipe for imitating the SOSEX energy while reducing the memory requirements to $\mathcal{O}(N^2)$.

Apart from technical convenience when having the drCCD amplitudes at hand, there is however no reason to limit the considered exchange diagrams to those where only the last interaction is anti-symmetrized. From an *ab-initio* point of view one should consider all diagrams where one interaction is anti-symmetrized and where violations of the Pauli principle can occur as the lowest order correction to the RPA. This is discussed in the next chapter.

Chapter 8

Adjacent Pairs Exchange

The Second Order Screened Exchange (SOSEX) correction to the Random Phase Approximation (RPA) arises from anti-symmetrizing only the last Coulomb interaction of RPA's ring diagrams as shown in Figure 7.1. When calculating the RPA using the direct ring Coupled Cluster Doubles (drCCD) amplitudes t_{ij}^{ab}, as introduced by (Freeman 1977), this comes at virtually no extra costs and represents a natural choice for the lowest order correction to the RPA. However, when calculating the RPA in the frequency domain, which is more efficient, there is a priori no reason to choose this particular class of diagrams as the lowest order correction to the RPA. Furthermore, it is not possible to evaluate the SOSEX diagrams directly since the last interaction in time cannot be explicitly addressed in the frequency domain. The AC-SOSEX approach, discussed in Section 7.2, offers an approximation but it contains swapped ladder diagrams that are not part of the many-body perturbation expansion. So the question remains, which diagrams, that are actually part of the many-body perturbation expansion, can be efficiently evaluated in the frequency domain and offer a good lowest order correction to the systematic error of the Random Phase Approximation.

8.1 Drivation of the Adjacent Pairs Exchange correction

As discussed in the beginning of Chapter 7, violations of the Pauli exclusion principle in RPA's ring diagrams suggest to anti-symmetrize the Coulomb interactions wherever such a violation can occur. In lowest order it should be only one but not necessarily just the last Coulomb interaction to be anti-symmetrized. This is done by cutting out one Coulomb interaction including the adjacent pair bubbles from the RPA ring diagrams and anti-symmetrizing this interaction if that can correct for a violation of the Pauli exclusion principle.

8.1.1 Two Sided Adjacent Pairs Exchange

Two adjacent pair bubbles have four possible time orders with respect to the Coulomb interaction between them, shown in Figure 8.1(a). In the first and in the last case an anti-symmetrization of the contained Coulomb interaction only cancels contributions where the same states i and a occur in consecutive bubbles, as illustrated in Figure 8.1(b). In general, such contributions do not violate the Pauli exclusion principle. Following this argument, we exclude these cases and study a correction to the Random Phase Approximation where both
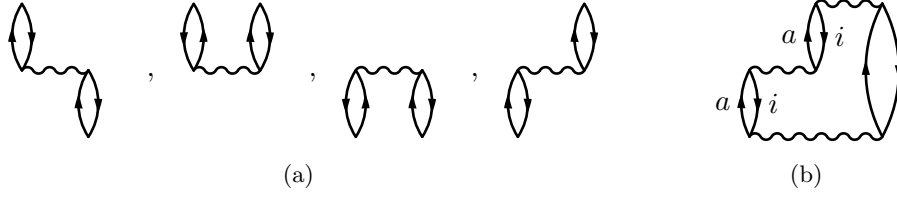
Figure 8.1: (a) The possible time orders of a Coulomb interaction and its two adjacent pair bubbles. (b) Anti-symmetrizing the first and the last case only cancels contributions i and a as indicated here for example. In general, these contributions do not violate the Pauli exclusion principle.
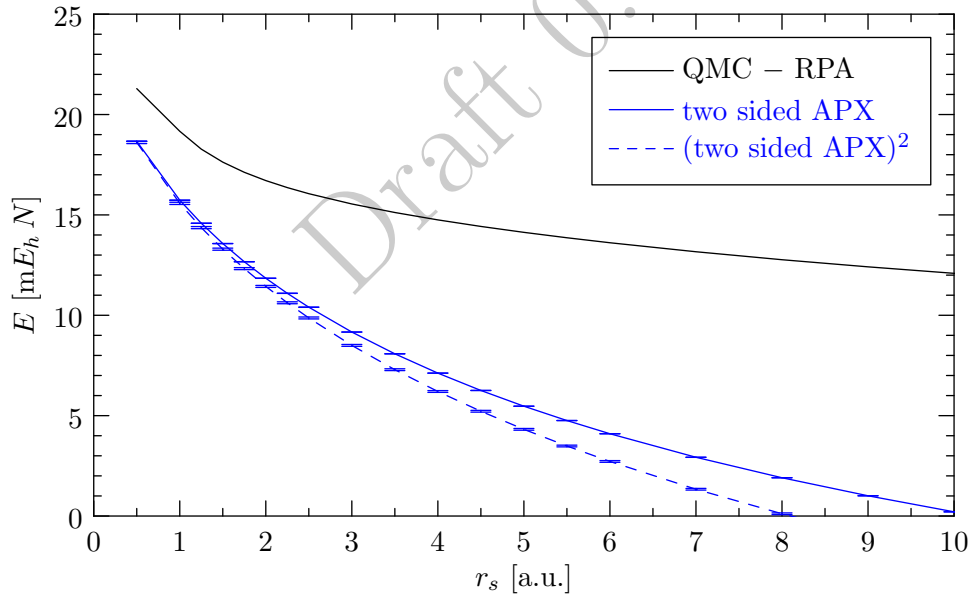
Figure 8.2: The Two sided Adjacent Pairs Exchange (2APX) energy per electron for the uniform electron gas compared to the error of the Random Phase Approximation with respect to Quantum Monte-Carlo (QMC) calculations by (Ceperley and Alder 1980) fitted by (Perdew and Zunger 1981). Anti-symmetrizing more than one interaction in the RPA ring diagrams by the application of (8.1) worsens the accuracy with respect to Quantum Monte Carlo results.

remaining cases are anti-symmetrized to

$$\text{(8.1)}$$

and inserted into the RPA ring diagrams. Since these diagrams are polarization parts with two open vertices the memory requirement for calculating this correction scales like $\mathcal{O}(N^2)$ with the system size N. This is equivalent to the memory requirement of the AC-SOSEX and considerably less than $\mathcal{O}(N^4)$ of the conventional SOSEX, calculated from the direct ring Coupled Cluster Doubles (drCCD) amplitudes. We term this correction *two sided Adjacent Pairs Exchange (2APX)* and its expansion in terms of Goldstone diagrams is given by

$$E_{\text{c}}^{\text{2APX}} = \quad + \quad + \quad + \ldots + \quad$$
$$t.r. \;+\; \ldots \tag{8.2}$$

The second row contains only the right contribution of (8.1) and *t.r.* refers to diagrams emerging from the second row by time reversal, containing only the left contribution of (8.1).

The two sided Adjacent Pair Exchange correction differs from the Second Order Screened Exchange correction already in third order. Time reversal of any SOSEX diagram beyond second order gives a distinct diagram and that is contained in the two sided APX. Since third order is the lowest order where the two sided APX and SOSEX differ and since this order is in general negative, the two sided APX correction is expected to be less than the SOSEX correction. Evaluating the two sided APX for the Uniform Electron Gas, as discussed in Section 8.2, confirms this expectation. As shown in Figure 8.2 the two sided APX considerably underestimates the desired energy correction, given by the difference of the RPA and Quantum Monte Carlo results. At low densities, where $r_s > 10$, it even becomes negative, actually worsening the systematic error of RPA.

The two sided Adjacent Pairs Exchange correction seems the most plausible lowest order correction to the Random Phase Approximation. However, despite improving on the RPA in the UEG for densities with $r_s < 10$, the two sided APX does not offer a balanced correction to the RPA since it always underestimates, but never overestimates the missing correlation energy. One could include diagrams, where two, three or more of the RPA's Coulomb interactions are anti-symmetrized, in the fashion discussed above, as the next orders of the correction. These corrections are still forming a ring and can thus be efficiently evaluated in the frequency domain, once the two sided Adjacent Pairs Exchange polarization part $\mathbf{P}_{\text{x}}^{\text{2AXP}}$ has been calculated. In terms of Feynman diagrams and propagator matrices, the corrections
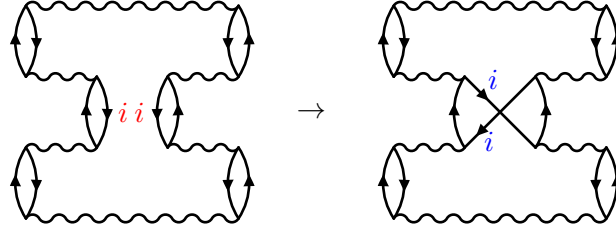
Figure 8.3: Exchange of pair bubbles that are non-adjacent

with one or two Coulomb interactions anti-symmetrized are given by

$$
E_{\mathrm{c}}^{2\mathrm{APX}} = \;\; \text{(diagram)}
$$

$$
= \frac{1}{2}\left(\frac{1}{2}\,\mathbf{P}_{\mathrm{x}}\mathbf{V} + \mathbf{P}_{\mathrm{x}}\mathbf{V}\mathbf{X}_0\mathbf{V} + \mathbf{P}_{\mathrm{x}}\mathbf{V}\mathbf{X}_0\mathbf{V}\mathbf{X}_0\mathbf{V} + \dots\right) \tag{8.3}
$$

$$
E_{\mathrm{c}}^{(2\mathrm{APX}^2)} = \;\; \text{(diagram)} \;\; + \;\; \text{(diagram)}
$$

$$
= E_{\mathrm{c}}^{2\mathrm{APX}} + \frac{1}{2\cdot 2}\left(\mathbf{P}_{\mathrm{x}}\mathbf{V} + \mathbf{P}_{\mathrm{x}}\mathbf{V}\mathbf{X}_0\mathbf{V} + \mathbf{P}_{\mathrm{x}}\mathbf{V}\mathbf{X}_0\mathbf{V}\mathbf{X}_0\mathbf{V} + \dots\right)^2 \tag{8.4}
$$

with

$$
\text{(}\mathbf{P}_{\mathrm{x}}\text{)} = \text{(diagram)} + \text{(diagram)},
$$

and where the superscript of $\mathbf{P}_{\mathrm{x}}^{2\mathrm{APX}}$, the trace, the imaginary time integration - including the sign - and the imaginary time arguments have been omitted for brevity. The RPA screened interaction $\approx\!\!\approx$ is given by (6.7). All diagrams posses reflection symmetry but note that the symmetry factor differs in the case where only one occurrence of $\mathbf{P}_{\mathrm{x}}^{2\mathrm{APX}}$ is inserted into the ring diagrams compared to other case. This is due to a reflection symmetry introduced when closing $\mathbf{P}_{\mathrm{x}}^{2\mathrm{APX}}$ with only one Coulomb interaction $\mathbf{V}$. Figure 8.2 shows $E_{\mathrm{c}}^{2\mathrm{APX}}$ and $E_{\mathrm{c}}^{(2APX)^2}$ according to (8.3) and (8.4). More insertions of $\mathbf{P}_{\mathrm{x}}^{2\mathrm{APX}}$ into the ring diagrams of the Random Phase Approximation actually worsen the a accuracy of the two sided APX with respect to Quantum Monte Carlo results. More than two insertions of $\mathbf{P}_{\mathrm{x}}^{2\mathrm{APX}}$ into the ring diagrams of the RPA offer no improvement either so none of the two sided APX approximations ever overestimates the missing correlation energy and thus none is balanced.

We could investigate more complex exchange processes, for instance those correcting violations of the Pauli exclusion principle of pair bubbles in the RPA that are not adjacent, as sketched in Figure 8.3. However, the exclusion principle is only violated if the two effected pair bubbles propagate at overlapping times. This would require a time order which can only be provided when evaluating the Random Phase Approximation from the direct ring Coupled Cluster Doubles (drCCD) amplitudes, loosing the advantage of the reduced memory requirements of an RPA implementation in the frequency domain.
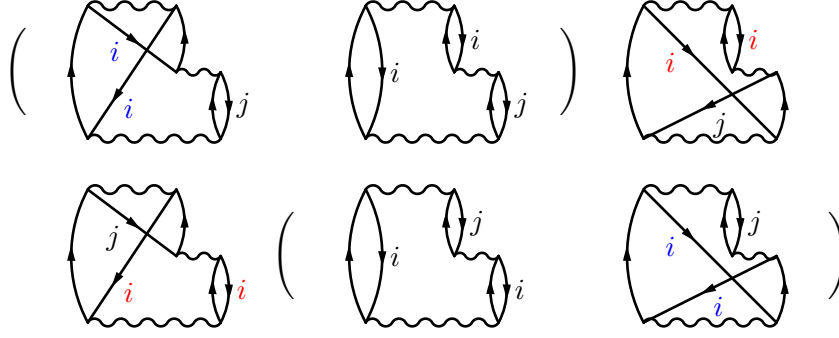
Figure 8.4: The two sided Adjacent Pairs Exchange correction introduces new violations of the Pauli exclusion principle, as shown here in third order in the case of two identical hole indices. One of the two exchange diagrams exactly cancels the offending contributions of the RPA diagram, indicated by parenthesis and blue index labels. The other exchange diagram, however, introduces new violations shown by red index labels.

8.1.2 Adjacent Pairs Exchange

The unbalanced performance of the two sided APX and its higher order variants rises the question whether really all Coulomb interactions should be anti-symmetrized if that can correct for violations of the Pauli exclusion principle. It turns out that the two sided APX, while indeed correcting for all violations occurring in adjacent pairs, introduces new violations. In third order this is most apparent and illustrated in Figure 8.4. The lower/upper row shows the case where the lower/upper two pair bubbles of the RPA propagate in the same hole state i. The diagram shown with blue index labels exchanges these two propagators and exactly cancels the offending contributions of the RPA. This is indicated by parenthesis around the RPA and the respective exchange diagram. The other diagram, however, introduces new violations to the Pauli exclusion principle, shown by the red index labels.

The key issue in this case is that the leftmost and longest pair bubble of the RPA diagram is exchanged in both diagrams of the two sided APX corrections. While this guarantees that all possible violating contributions are canceled, it always introduces new violations. For a more balanced correction we therefore require that each pair bubble is exchanged at most once. The simplest correction satisfying this requirement is the (single sided) *Adjacent Pairs Exchange (APX)* correction, where only one case of (8.1) is contained. For a system with time reflection symmetry it is irrelevant which of the cases we choose and without loss of generality we choose to anti-symmetrize adjacent pair bubbles in the third case of time orders shown in Figure 8.1(a):

$$ \text{(8.5)} $$

In terms of Feynman diagrams and the matrix notation of the propagators, introduced in

Section 6.1, the APX correction is then given by

$$E_c^{APX} = \left(\!\mathbf{P_x}\!\right)\!\!\} = \bigotimes + \left(\!\mathbf{P_x}\!\right)\!\! + \left(\!\mathbf{P_x}\!\right)\!\!\} + \dots \tag{8.6}$$

$$= -\frac{1}{2}\int\frac{d\nu}{2\pi}\,\mathrm{tr}\Big\{\mathbf{P}_x^{APX}\mathbf{V} + \mathbf{P}_x^{APX}\mathbf{V}\mathbf{X}_0\mathbf{V} + \mathbf{P}_x^{APX}\mathbf{V}\mathbf{X}_0\mathbf{V}\mathbf{X}_0\mathbf{V} + \dots\Big\}$$

$$= -\frac{1}{2}\int\frac{d\nu}{2\pi}\,\mathrm{tr}\Big\{\mathbf{P}_x^{APX}\mathbf{W}\Big\}$$

with

$$\left(\!\mathbf{P_x}\!\right) = \bigotimes \ ,$$

and where the imaginary time arguments as well as the superscript of $\mathbf{P}_x^{APX}$ in the diagrams have been omitted for brevity. All diagrams exhibit a single reflection symmetry but note that, unlike in the two sided APX case, there is no additional symmetry introduced when closing $\mathbf{P}_x^{APX}$ with one Coulomb interaction $\mathbf{V}$ since the $\mathbf{P}_x^{APX}$ contains only one of the two time orders contained in $\mathbf{P}_x^{2APX}$. Despite the ring form of the APX diagrams beyond second order, none of them has a rotational symmetry in contrast to the respective RPA diagrams. This simplifies the sum over all orders of the perturbation compared to the RPA since all orders have the same factor. We can use the infinite sum of a geometric series to give an explicit form for the APX energy:

$$E_c^{APX} = -\frac{1}{2}\int_{-\infty}^{\infty}\frac{d\nu}{2\pi}\,\mathrm{tr}\left\{\mathbf{P}_x^{APX}(i\nu)\mathbf{V}\Big(\mathbf{1}-\mathbf{X}_0(i\nu)\mathbf{V}\Big)^{-1}\right\} , \tag{8.7}$$

where the imaginary frequency dependent exchange polarizability for the APX contains only one of the four time orders contained in $\mathbf{P}_x^{AC}$, which was given in (7.7):

$$\mathbf{P}_x^{APX}{}_{\mathbf{x}_1\mathbf{x}_2}(i\nu) = -\iint d\mathbf{x}_3\,d\mathbf{x}_4\,\frac{1}{|\mathbf{r}_3-\mathbf{r}_4|}\sum_{ia}\psi_i^*(\mathbf{x}_4)\psi_i(\mathbf{x}_1)\psi_a^*(\mathbf{x}_1)\psi_a(\mathbf{x}_3)\frac{1}{\varepsilon_a-\varepsilon_i+i\nu}$$

$$\sum_{jb}\psi_j^*(\mathbf{x}_3)\psi_j(\mathbf{x}_2)\psi_b^*(\mathbf{x}_2)\psi_b(\mathbf{x}_4)\frac{1}{\varepsilon_b-\varepsilon_j-i\nu} . \tag{8.8}$$

8.2 APX for the uniform electron gas

Evaluating the Adjacent Pairs Exchange (APX) energy for the Uniform Electron Gas (UEG) is very similar to evaluating the AC-SOSEX energy according to (7.16). In contrast to the AC-SOSEX expression, only one of the four time orders of two adjacent pair bubbles are contained in the APX. In the chosen order, the Coulomb interaction of the exchange polarizability $\mathbf{P}_x^{APX}$

occurs after both open vertices of $\mathbf{P}_{\mathrm{x}}^{\mathrm{APX1}}$
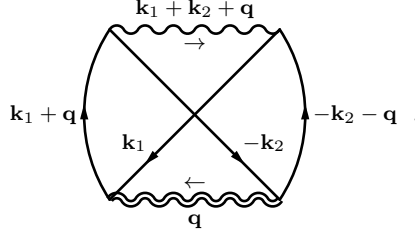
Furthermore, the APX uses the screened interaction W, represented by the double wiggly line, as given by (6.7) rather than the coupling strength averaged screened interaction $\overline{W}$, since all orders of the expansion have the same factor. The APX correction to the Random Phase Approximation per electron is thus given by

$$E_{\mathrm{c}}^{\mathrm{APX}} = +\frac{\Omega}{N}\frac{1}{2}\int\frac{\mathrm{d}\nu}{2\pi}\int\frac{\mathrm{d}\mathbf{q}}{(2\pi)^3}\sum_{\sigma}\iint_{|\mathbf{k}_i|<k_{\mathrm{F}}<|\mathbf{k}_i+\mathbf{q}|}\frac{\Omega^2\mathrm{d}\mathbf{k}_1\mathrm{d}\mathbf{k}_2}{(2\pi)^6}\,V(\mathbf{k}_1+\mathbf{k}_2+\mathbf{q})W(\mathbf{q},\nu)$$
$$\frac{1}{(\Delta\varepsilon_{\mathbf{k}_1,\mathbf{q}}+\mathrm{i}\nu)(\Delta\varepsilon_{-\mathbf{k}_2,-\mathbf{q}}-\mathrm{i}\nu)}\,, \qquad (8.9)$$

with $i \in \{1,2\}$ and the single particle excitation energy $\Delta\varepsilon_{\mathbf{k}_i,\mathbf{q}} = (\mathbf{k}_i+\mathbf{q})^2/2 - \mathbf{k}_i^2/2$. As in the case of the AC-SOSEX, the above expression can be evaluated by a Monte-Carlo integration for $\mathbf{k}_1$ and $\mathbf{k}_2$ using a probability density function (PDF) given by

$$\mathrm{PDF}(\mathbf{k}_i) \propto \begin{cases} \left|\dfrac{1}{\Delta\varepsilon_{\mathbf{k}_i,\mathbf{q}}\pm\mathrm{i}\nu}\right| & \text{for } |\mathbf{k}_i| < k_{\mathrm{F}} < |\mathbf{k}_i+\mathbf{q}|\,, \\ 0 & \text{otherwise.} \end{cases}$$

The momentum $\mathbf{q}$ and the imaginary frequency ν can be integrated using a Gauss–Kronrod rule, analogous to the evaluation of the Random Phase Approximation. However, the asymptotic behavior of the APX energy for large imaginary frequencies differs from that of the RPA and the AC-SOSEX, such that a different variable transform for integrating the frequency tail must be used. The asymptotic behavior for large frequencies is discussed Subsection 8.2.2.

For the lowest order of the APX, the accuracy of the numerical integrations can be benchmarked against the MP2 exchange energy, which is independent of the density and it is known *analytically* from the work of (Onsager, Mittag, and Stephen 1966):

$$\frac{\log(2)}{6} - 3\frac{\zeta(3)}{(2\pi)^2} \approx 0.02417915891814441 E_h\,N\,.$$

For the Monte-Carlo integration of $\mathbf{k}_1$ and $\mathbf{k}_2$ a precision of 5 significant digits can be achieved with less than 30000 samples for each q and ν, depending on momentum, frequency and density. The error from the momentum and imaginary frequency integration is of similar magnitude. Figure 8.5 and Table 8.1 show the resulting APX energies as a function of density given by the Wigner-Seitz radius, r_s. The uncertainties from the integrations are indicated by the error bars.

---

[1]In the given diagram, the time order of the vertices is only relevant with respect to the Coulomb interaction. It is therefore neither a Goldstone nor a Feynman diagram. The proper Feynman diagram of APX is the leftmost diagram of (8.6).
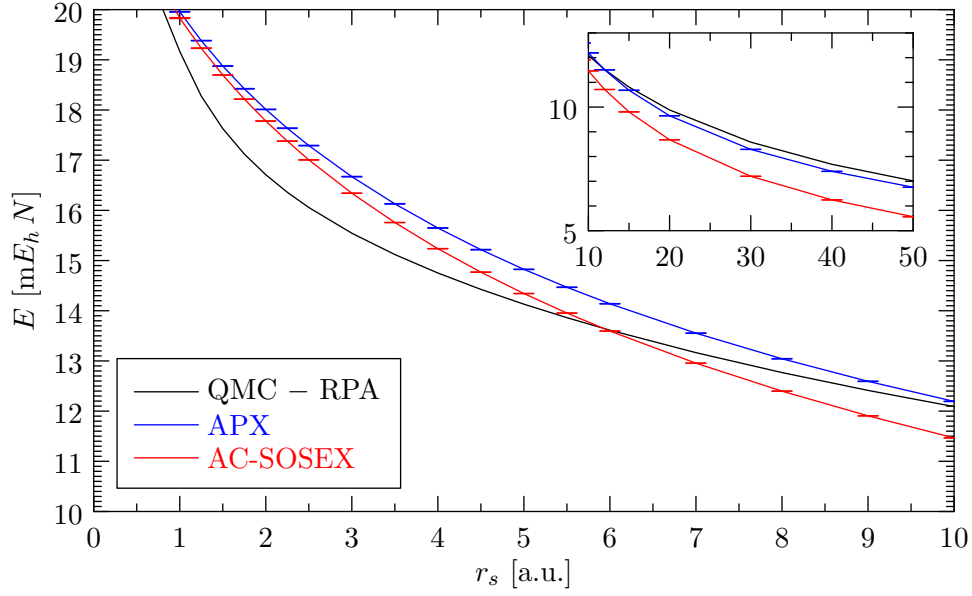
Figure 8.5: The Adjacent Pairs Exchange (APX) energy per electron for the uniform electron gas compared to the error of the Random Phase Approximation with respect to Quantum Monte-Carlo (QMC) calculations by (Ceperley and Alder 1980) fitted by (Perdew and Zunger 1981). RPA+APX also fortuitously matches the QMC results but only at $r_s \approx 10$. However, in the low density regime, where correlation is stronger, APX is considerably closer to the QMC results than AC-SOSEX. For results of the spin-polarized uniform electron gas see Subsection 8.2.3.

r_s	$(E_\mathrm{c} - E_\mathrm{c}^{\mathrm{RPA}})$	$E_\mathrm{c}^{\mathrm{APX}}$		$E_\mathrm{c}^{\mathrm{AC-SOSEX}}$	
[a.u.]	$[\mathrm{m}E_h\,N]$	$[\mathrm{m}E_h\,N]$	$\pm$	$[\mathrm{m}E_h\,N]$	$\pm$
1	19.167	19.956	0.005	19.832	0.009
2	16.710	18.012	0.005	17.780	0.003
3	15.545	16.672	0.005	16.342	0.003
4	14.752	15.649	0.005	15.237	0.003
5	14.131	14.825	0.004	14.343	0.003
6	13.613	14.139	0.004	13.595	0.003
7	13.165	13.553	0.004	12.955	0.003
8	12.768	13.043	0.004	12.398	0.003
9	12.413	12.594	0.004	11.906	0.003
10	12.090	12.194	0.004	11.466	0.003
12	11.521	11.506	0.004	10.712	0.003
15	10.810	10.680	0.004	9.806	0.003
20	9.884	9.650	0.004	8.679	0.003
30	8.582	8.289	0.004	7.201	0.003
40	7.685	7.400	0.004	6.246	0.003
50	7.014	6.757	0.004	5.564	0.003

Table 8.1: Data of Figure 8.5 including low densities.

8.2.1 Large momentum behavior

In a solid or in a molecule, the finite resolution of the DFT or the Hartree-Fock reference imposes an upper limit $G_{\max}$ on up to where the exchange polarizability $\mathbf{P}_x^{\text{APX}}$ and the independent particle polarizability $\mathbf{X}_0$ can be evaluated. Assuming that the system is sufficiently homogeneous at that resolution the asymptotic behavior for large momenta in the Uniform Electron Gas can be used to extrapolate results retrieved at finite $G_{\max}$ to the limit of an infinite basis set, where $G_{\max} \to \infty$.

We can write the APX correction in the UEG from (8.9) in terms an exchange polarizability $P_x^{\text{APX}}(q, i\nu)$, analogous to the general APX expression (8.7):

$$E_c^{\text{APX}} = -\frac{\Omega}{N} \frac{1}{2} \int \frac{\mathrm{d}\nu}{2\pi} \int \frac{\mathrm{d}\mathbf{q}}{(2\pi)^3} \, P_x^{\text{APX}}(\mathbf{q}, i\nu) V(\mathbf{q}) \Big(1 - \chi_0(\mathbf{q}, i\nu) V(\mathbf{q})\Big)^{-1}, \tag{8.10}$$

$$P_x^{\text{APX}}(\mathbf{q}, i\nu) = -\sum_\sigma \iint\limits_{|\mathbf{k}_i| < k_F < |\mathbf{k}_i + \mathbf{q}|} \frac{\Omega^2 \mathrm{d}\mathbf{k}_1 \mathrm{d}\mathbf{k}_2}{(2\pi)^6} \, V(\mathbf{k}_1 + \mathbf{k}_2 + \mathbf{q}) \, \frac{1}{(\Delta\varepsilon_{\mathbf{k}_1,\mathbf{q}} + i\nu)(\Delta\varepsilon_{-\mathbf{k}_2,-\mathbf{q}} - i\nu)} . \tag{8.11}$$

To get an approximation P_x^{APX} for large momenta q we can trivially integrate $\mathbf{k}_1$ and $\mathbf{k}_2$, since $|\mathbf{k}_i| < k_F \ll q$, getting

$$P_x^{\text{APX}}(q, i\nu) \sim \frac{1}{q^2} \frac{1}{(q^2/2 + i\nu)(q^2/2 - i\nu)} . \tag{8.12}$$

Inserting this and the approximation of $\chi_0(q, i\nu) V(q)$ for large q, given in (6.54), into the APX energy expression, we can integrate ν for a given, large momentum q:

$$\int \frac{\mathrm{d}\nu}{2\pi} \frac{1}{q^4} \frac{1}{(q^2/2 + i\nu)(q^2/2 - i\nu)} \left(1 - \frac{1}{(q^2/2)^2 + \nu^2}\right)^{-1} = \frac{1}{q^4 \sqrt{q^4 - 4}} .$$

The missing energy ΔE_c^{APX} of the APX correction when truncating the momentum integration at a finite but large momentum $G_{\max}$ is thus

$$\Delta E_c^{\text{APX}}(G_{\max}) \sim \int_{G_{\max}}^\infty \frac{q^2}{q^4 \sqrt{q^4 - 4}} \sim a_3 \frac{1}{G_{\max}^3} + a_7 \frac{1}{G_{\max}^7} + \mathcal{O}\left(\frac{1}{G_{\max}^{11}}\right), \tag{8.13}$$

where we have expanded the integrand in the variable $u = 1/q$ at $u = 0$. Hence, the APX energy and, similarly, the AC-SOSEX energy have the same asymptotic behavior with respect to large momenta $\mathbf{q}$ as the Random Phase Approximation. However, the convergence with respect to $G_{\max}$ is slower since the exchange corrections are more short ranged, which may require the use of more than the leading order term of the Taylor expansion for an accurate extrapolation to the infinite basis set limit.

8.2.2 Large imaginary frequency behavior

For the frequency integration of metallic systems, such as the Uniform Electron Gas, knowledge about the asymptotic behavior of the APX correction with respect to large imaginary frequencies is important for choosing an appropriate variable transform for the tail.

For large momenta q, we can use the approximation of P_x^{APX} in (8.12), gotten in the previous subsection. Considering large frequencies ν, we can still use the same approximation
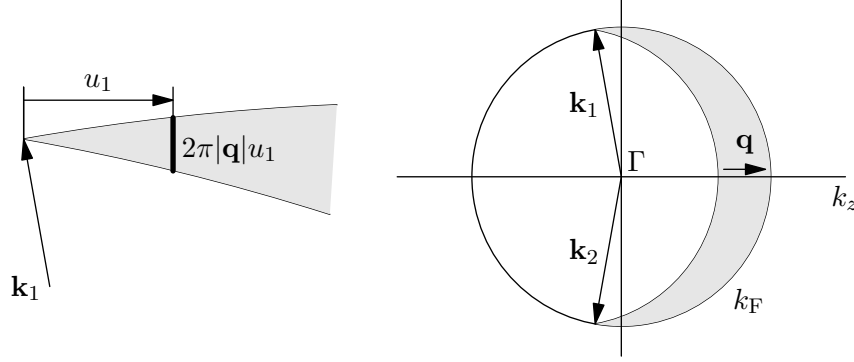
Figure 8.6: Cross section of the set of momenta $\mathbf{k}_i$ such that $|\mathbf{k}_i| < k_\mathrm{F} < |\mathbf{k}_i + \mathbf{q}|$ for excitation momenta $\mathbf{q} \leq 2$. The momentum of the Coulomb interaction $\mathbf{k}_1 + \mathbf{k}_2 + \mathbf{q}$ vanishes for the shown $\mathbf{k}_1$ and $\mathbf{k}_2$. The vicinity of the singular $\mathbf{k}_1$ is magnified on the left, showing the employed coordinates for the integration of this regions and a volume element in form of a ring with area $2\pi|\mathbf{q}|u_1$.

for intermediate $q > 2k_\mathrm{F}$ since the denominator of the propagator $V(\mathbf{k}_1 + \mathbf{k}_2 + \mathbf{q})$ is non-vanishing and the volume of the integration region of $\mathbf{k}_1$ and $\mathbf{k}_2$ is independent of q. In this case the integration of $\mathbf{k}_1$ and $\mathbf{k}_2$ merely averages the contributions. For $q \leq 2k_\mathrm{F}$, the volume of the integration region of $\mathbf{k}_1$ and $\mathbf{k}_2$ depends on q and there are also contributions where the propagator $V(\mathbf{k}_1 + \mathbf{k}_2 + \mathbf{q})$ becomes singular, as shown in Figure 8.6. In this case, we split the integration into two parts. In the first part both, $\mathbf{k}_1$ and $\mathbf{k}_2$ are in the vicinity of the singular contribution, shown for $\mathbf{k}_1$ on the left of Figure 8.6. In the remaining part either $\mathbf{k}_1$, $\mathbf{k}_2$ or both are away from the singular contribution. For the first part, we can transform the integration of $\mathbf{k}_1$ and $\mathbf{k}_2$ into an integration of the respective distances u_1 and u_2 from the singular contribution in the direction of $\mathbf{q}$. In the remaining part, we approximate the integral assuming that $\mathbf{k}_1 + \mathbf{k}_2$ average out and taking into consideration that the integration volume of each $\mathbf{k}_i$ scales like $q^3 + q^2$. We get

$$
\iint\limits_{|\mathbf{k}_i| < k_\mathrm{F} < |\mathbf{k}_i + \mathbf{q}|} \frac{\Omega^2 \mathrm{d}\mathbf{k}_1 \mathrm{d}\mathbf{k}_2}{(2\pi)^6} V(\mathbf{k}_1 + \mathbf{k}_2 + \mathbf{q}) \sim \iint_0^{k_\mathrm{F} - q/2} \mathrm{d}u_1 \mathrm{d}u_1 \frac{(2\pi)^2 q^2 u_1 u_2}{(u_1 + u_2)^2} + \frac{(a_3 q^3 + a_2 q^2)^2}{q^2}
$$
$$
\sim q^2 + \mathcal{O}\left(q^3\right) . \tag{8.14}
$$

Since $q \leq 2$ and ν is large, we can ignore the propagators of $P_\mathrm{x}^\mathrm{APX}$ containing the imaginary frequency for the integration of $\mathbf{k}_1$ and $\mathbf{k}_2$.

We can now insert the respective approximation of $P_\mathrm{x}^\mathrm{APX}$ for small q, intermediate q and large q into the expression for the APX energy (8.10) and integrate q. For χ_0 we use the approximations (6.56), (6.57) and (6.54) for small, intermediate and large momenta q, respectively. The results are long and apart from their expansion in ν of no particular interest. For small and intermediate q the integration of q yields $1/\nu^2 + \mathcal{O}\left(1/\nu^4\right)$ and for large q we get $1/\nu^2 + \mathcal{O}\left(1/\nu^{5/2}\right)$. Finally, we can insert this expansion in the imaginary frequency integration of the APX energy and estimate the missing energy per electron $\Delta E_\mathrm{c}^\mathrm{APX}(\nu_\mathrm{max})$
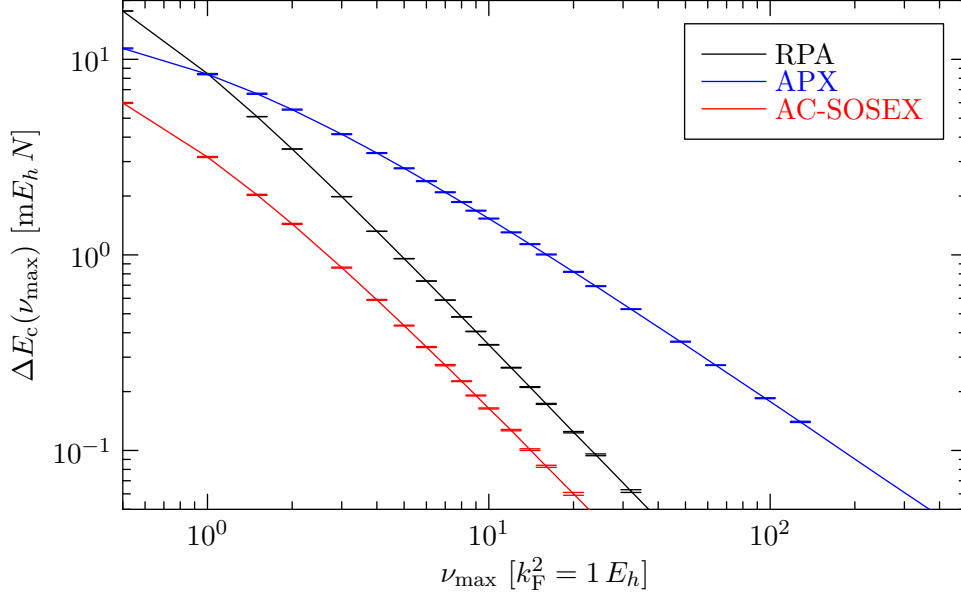
Figure 8.7: Numerical comparison of the missing correlation energy per electron for the Random Phase Approximation and its corrections when truncating the imaginary frequency integration at ν_{max}. ν_{max} is given in units of k_F^2 and $k_F = 1$ a.u.

when truncating the integration at some finite but large imaginary frequency ν_{max}:

$$\Delta E_c^{APX}(\nu_{max} \sim \int_{\nu_{max}}^{\infty} d\nu \left(\frac{1}{\nu^2} + \mathcal{O}\left(\frac{1}{\nu^{5/2}}\right)\right) \sim \frac{1}{\nu_{max}} + \mathcal{O}\left(\frac{1}{\nu_{max}^{3/2}}\right). \tag{8.15}$$

The asymptotic behavior of the APX energy differs from that of the Random Phase Approximation and from that of the AC-SOSEX, which can be derived in an analogous fashion. This originates from the imaginary frequency behavior of P_x^{APX}, containing only one of the four time orders contained in the RPA and in the AC-SOSEX. Figure 8.7 compares the asymptotic behavior of RPA, AC-SOSEX and APX for the Uniform Electron Gas numerically.

8.2.3 Spin-polarized Uniform Electron Gas

We can readily evaluate the RPA and the Adjacent Pairs Exchange correction for the spin-polarized Uniform Electron Gas using only one spin in the sum over all spins $\sum_\sigma$, occurring in the expression of $P_x^{APX}(\mathbf{q}, i\nu)$ in (8.11) and $\chi_0(\mathbf{q}, i\nu)$ in (6.46). Considering that k_F also depends on wheter the UEG is spin-polarized or not according to (6.39), yields correlation energies of RPA+APX shown in Figure 8.8 and Table 8.2. For comparison, the correlation energy of RPA+AC-SOSEX according to (7.16) is also given.

Unlike in the non-spin-polarized case, neither of the SOSEX variants offers a balanced correction to the Random Phase Approximation, overestimating the missing energy for the entire range of densities. The accuracy with respect to Quantum Monte Carlo results also worsens for low densities. For low densities we can assume $\mathbf{k}_1 + \mathbf{k}_2 + \mathbf{q} \approx \mathbf{q}$ since $|\mathbf{k}_i| < k_F \ll 1$. In this limit, two adjacent RPA bubbles only differ from the respective exchange diagram in
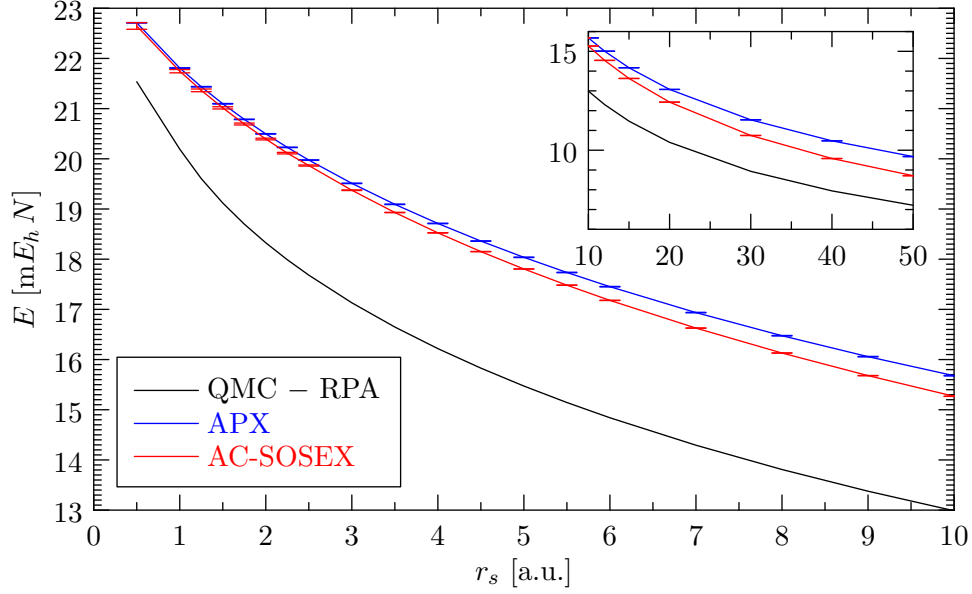
Figure 8.8: The Adjacent Pairs Exchange (APX) energy per electron for the spin-polarized uniform electron gas compared to the error of the Random Phase Approximation with respect to Quantum Monte-Carlo (QMC) calculations by (Ceperley and Alder 1980) fitted by (Perdew and Zunger 1981). For low densities, anti-symmetrization of a ring diagram merely changes its sign, such that SOSEX or its variants simply remove the correlation energy already captured by the RPA.

r_s [a.u.]	$(E_c - E_c^{RPA})$ $[mE_h\,N]$	E_c^{APX} $[mE_h\,N]$	$\pm$	$E_c^{AC-SOSEX}$ $[mE_h\,N]$	$\pm$
1	20.192	21.809	0.005	21.746	0.033
2	18.326	20.497	0.005	20.394	0.017
3	17.131	19.511	0.005	19.374	0.006
4	16.218	18.712	0.005	18.525	0.003
5	15.472	18.037	0.005	17.805	0.003
6	14.840	17.452	0.005	17.179	0.003
7	14.293	16.936	0.005	16.627	0.003
8	13.809	16.475	0.005	16.130	0.003
9	13.377	16.058	0.005	15.680	0.003
10	12.987	15.678	0.005	15.268	0.003
12	12.307	15.007	0.005	14.541	0.003
15	11.469	14.169	0.004	13.628	0.003
20	10.398	13.073	0.004	12.431	0.003
30	8.932	11.536	0.004	10.745	0.003
40	7.943	10.474	0.004	9.580	0.003
50	7.215	9.678	0.004	8.710	0.003

Table 8.2: Data of Figure 8.8 including low densities.

the Fermion sign and the additional spin variable from having two loops instead of one:
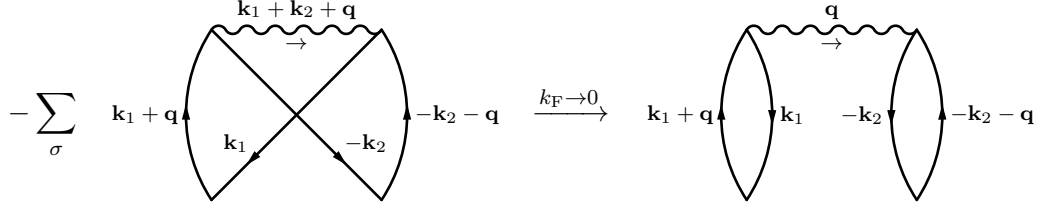
In the spin-polarized case, the exchange diagram entirely cancels the two pair bubbles for densities low enough and as a consequence RPA+SOSEX excatly cancels in the limit $k_F \to 0$. RPA+APX becomes even positive, since APX contains more diagrams than RPA. This occurs, however, only at very low densities beyond $r_s \approx 88$.

8.3 APX for solids

In solids or in molecules the Adjacent Pairs Exchange correction can be evaluated in a similar fashion as the Random Phase Approximation. Collecting positive and negative imaginary frequencies and rotating the matrices cyclically converts all involved matrices into symmetric, real valued matrices:

$$
E_c^{\mathrm{APX}} = -\frac{1}{2} \int_0^\infty \frac{d\nu}{2\pi} \operatorname{tr} \left\{ \mathbf{V}^{\frac{1}{2}} \left(\mathbf{P}_x^{\mathrm{APX}}(\mathrm{i}\nu) + \mathbf{P}_x^{\mathrm{APX}}(-\mathrm{i}\nu) \right) \mathbf{V}^{\frac{1}{2}} \left(\mathbf{1} - \mathbf{V}^{\frac{1}{2}} \mathbf{X}_0(\mathrm{i}\nu) \mathbf{V}^{\frac{1}{2}} \right)^{-1} \right\}.
$$

This makes the evaluation of the inverse numerically more stable. The independent particle polarizability $\mathbf{X}_0$ and the exchange polarizability $\mathbf{P}_x^{\mathrm{APX}}$ can be evaluated in imaginary frequency according to (6.10) and (8.16) in $\mathcal{O}(N^3)$ and in $\mathcal{O}(N^5)$ steps, respectively. The memory requirement for both cases is $\mathcal{O}(N^2)$. Accepting a memory footprint of $\mathcal{O}(N^3)$, the evaluation of the APX and, similarly, of the AC-SOSEX correction can be improved to $\mathcal{O}(N^4)$ by storing the intermediate tensor $\mathbf{\Gamma}(\mathrm{i}\nu)$

$$
\mathbf{\Gamma}_{\mathbf{x}\mathbf{x}'\mathbf{x}''}(\mathrm{i}\nu) = \int_0^\infty d\tau\, e^{+\mathrm{i}\nu\tau} \mathbf{G}_{0\mathbf{x}\mathbf{x}'}(\mathrm{i}\tau) \mathbf{G}_{0\mathbf{x}'\mathbf{x}''}(-\mathrm{i}\tau)
$$

and then evaluating the exchange polarizability in terms of $\mathbf{\Gamma}$:

$$
\mathbf{P}_x^{\mathrm{APX}}{}_{\mathbf{x}_1\mathbf{x}_2}(\mathrm{i}\nu) = -\iint d\mathbf{x}_3\, d\mathbf{x}_4\, \frac{1}{|\mathbf{r}_3 - \mathbf{r}_4|} \mathbf{\Gamma}_{\mathbf{x}_4\mathbf{x}_1\mathbf{x}_3}(+\mathrm{i}\nu) \mathbf{\Gamma}_{\mathbf{x}_3\mathbf{x}_2\mathbf{x}_4}(-\mathrm{i}\nu).
$$

8.3.1 k-points and G_{max} convergence

In the diagrams of the Random Phase Approximation each Coulomb interaction mediates the same momentum q according to momentum conservation at each vertex. This makes the RPA the most important contribution for small momenta or, equivalently, at long distances. The diagrams of the Adjacent Pairs Exchange correction contain one Coulomb interaction with a different momentum than all others. Thus, the APX correction is more short ranged than the Random Phase Approximation resulting in a faster k-point convergence, as shown in the inset of Figure 8.9.
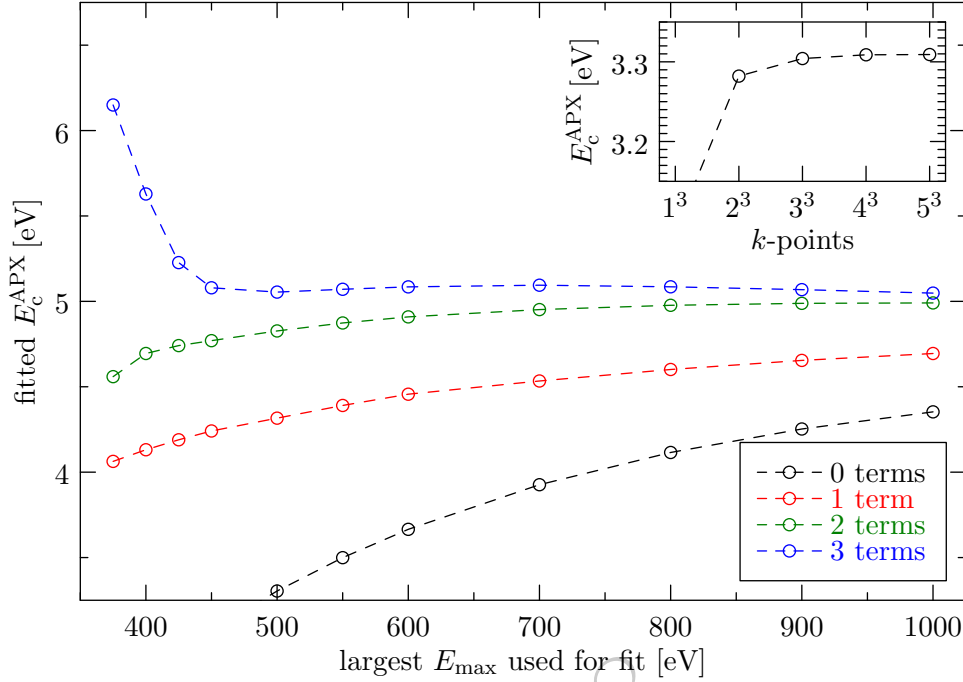
Figure 8.9: Basis set extrapolation of the APX energy for LiF with 10 electrons. The black points show the energies obtained at different cutoff energies $E_{\max}$. The colored points show a fit using one, two or three orders in the expansion of the APX energy with respect to large cutoff momenta. Each fit only uses data points with a cutoff energy below or equal to that of the fitted point. The inset shows the convergence of the APX energy with respect to different k point meshes.

The downside of the short ranged nature of the APX is that the convergence of the APX energy is slower with respect to the highest momentum $G_{\max}$ contained in $\mathbf{X}_0$ and $\mathbf{P}_{\mathrm{x}}^{\mathrm{APX}}$. Assuming that the system is homogeneous at distances short enough, the asymptotic behavior of the missing APX energy is equivalent to that of the Uniform Electron Gas, shown in Subsection 8.2.1. Figure 8.9 shows the convergence of the APX energy with respect to the employed energy cutoff $E_{\max} = G_{\max}^2/2$. Note that the automatic finite basis set extrapolation implemented in VASP cannot be used for the APX correction for two reasons. First, unlike $\mathbf{X}_0$, $\mathbf{P}_{\mathrm{x}}^{\mathrm{APX}}$ changes with each considered cutoff momentum since the Coulomb kernel changes. Recalculating the exchange polarizability is, however, too time consuming. Second, it is often not sufficient to consider only the leading order term of the asymptotic behavior. For an accurate extrapolation to $G_{\max} \to \infty$ it may be necessary to include the second, or higher order terms of the large momentum expansion for the Uniform Electron Gas. The asymptotic behavior can then be fit to

$$\Delta E_{\mathrm{c}}^{\mathrm{APX}}(G_{\max}) \sim a_3 \, \frac{1}{G_{\max}^3} + a_7 \, \frac{1}{G_{\max}^7} + \mathcal{O}\left(\frac{1}{G_{\max}^{11}}\right),$$

where ENMAX $= G_{\max}^2/2$ is manually risen. Only the first result line with the largest automatically chosen cutoff should be used and the number of bands NBANDS should be close to the maximum number of bands specified in the OUTCAR file of the DFT or Hartree-Fock
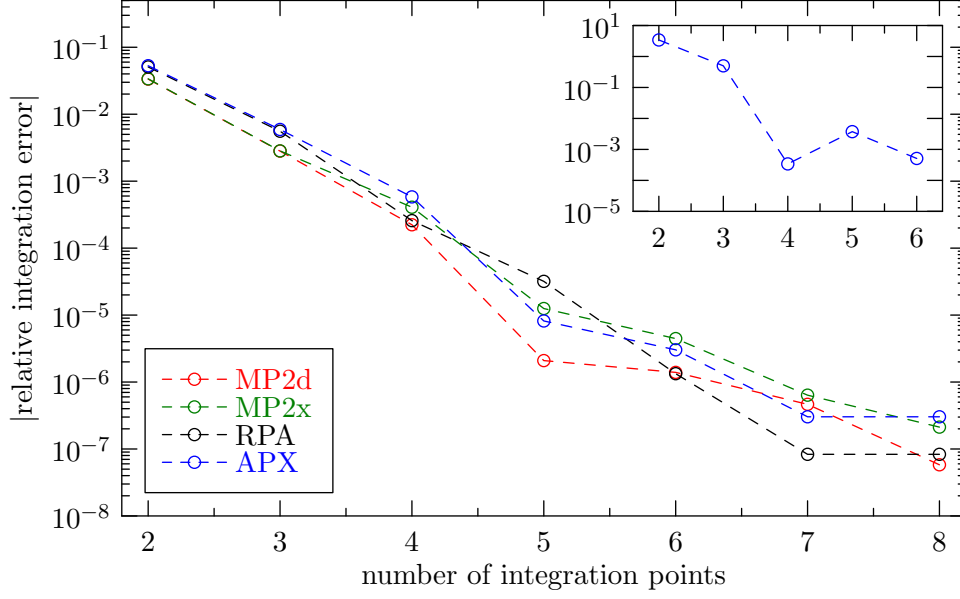
Figure 8.10: Relative error of the imaginary frequency integration for different approximations of the correlation energy of LiF, depending on the number of samples. The system contains 10 electrons and¡s 384 bands. The inset shows the error for the difference of the APX energy for different unit cell volumes, once at $15.4\,\text{Å}^3$ and once at $15.9\,\text{Å}^3$. The error is below $1\,\mu\text{eV}$ beyond the shown number of integration points.

calculation for each respective value of `ENCUT`. Note that `NBANDS` must be a multiple of the number of cores employed for the APX calculation. To avoid aliasing effects it is therefore advantageous to choose `ENMAX` such that the reported maximum number of bands is as close as possible to `NBANDS`.

8.3.2 Frequency grid

Directly evaluating (8.8) would require $\mathcal{O}(N^8)$ steps. However, $\mathbf{P}_{\text{x}}^{\text{APX}}$ can be calculated in imaginary time using the imaginary time propagators given in (6.11). Subsequently, it can be Fourier transformed numerically to imaginary frequency on a non-equidistant grid, analogous to calculating the independent particle polarizability as proposed by (Kaltak, Klimeš, and Kresse 2014b).

$$\mathbf{P}_{\text{x}}^{\text{APX}}{}_{\mathbf{x}_1\mathbf{x}_2}(\text{i}\nu) = -\iint \text{d}\mathbf{x}_3\,\text{d}\mathbf{x}_4\,\frac{1}{|\mathbf{r}_3-\mathbf{r}_4|}\int_0^\infty \text{d}\tau_1\,e^{+\text{i}\nu\tau_1}\mathbf{G}_{0\mathbf{x}_3\mathbf{x}_1}(\text{i}\tau_1)\mathbf{G}_{0\mathbf{x}_1\mathbf{x}_4}(-\text{i}\tau_1)$$
$$\int_0^\infty \text{d}\tau_2\,e^{-\text{i}\nu\tau_2}\mathbf{G}_{0\mathbf{x}_4\mathbf{x}_2}(\text{i}\tau_2)\mathbf{G}_{0\mathbf{x}_2\mathbf{x}_3}(-\text{i}\tau_2) \qquad (8.16)$$

The imaginary time propagators can be calculated in $\mathcal{O}(N^3)$ steps. If the number of samples for the two imaginary time and the final imaginary frequency integration is independent of the system size, the evaluation of the APX scales like $\mathcal{O}(N^4)$. The prefactor might, however, be considerable.

In the Random Phase Approximation the employed quadrature frequencies and weights are determined from a fit to the function of the direct MP2 energy, since it resembles the RPA energy function and its exact frequency integral is known. In the case of the APX energy the respective lowest order function would be the exchange MP2 energy

$$\frac{1}{2} \int \frac{d\nu}{2\pi} \frac{2(\varepsilon_a - \varepsilon_i)(\varepsilon_b - \varepsilon_j) + 2\nu^2}{\left((\varepsilon_a - \varepsilon_i)^2 + \nu^2\right)\left((\varepsilon_b - \varepsilon_j)^2 + \nu^2\right)} = \frac{1}{\varepsilon_i + \varepsilon_j - \varepsilon_a - \varepsilon_b}$$

and the quadrature frequencies ν_k and weights w_k could be fit such that the dominant terms with $a = b$ and $i = j$ are best reproduced by the numeric integral

$$\frac{1}{\varepsilon_i + \varepsilon_i - \varepsilon_a - \varepsilon_a} \approx \frac{1}{2} \sum_k w_k \frac{2(\varepsilon_a - \varepsilon_i)^2 + 2\nu_k^2}{\left((\varepsilon_a - \varepsilon_i)^2 + \nu_k^2\right)^2} \tag{8.17}$$

for all single particle excitation energies $\varepsilon_a - \varepsilon_i$. In general, this yields a different grid of optimal frequencies and weights than the grid obtained for the Random Phase Approximation according to (6.12). However, the APX energy also contains the independent particle polarizability in all orders beyond the second order, which suggests that the a frequency grid, optimized for the exchange MP2 term, might no longer be optimal for higher orders anyway. Figure 8.10 shows the convergence of the APX energy in LiF containing 10 electrons with respect to the number of imaginary frequency points, using a grid which is optimized for the RPA rather than for the APX. The convergence hardly differs for the different energies, justifying the use of the RPA optimized grid for calculating $\mathbf{P}_x^{APX}$ and subsequently the APX energy. For metallic systemy, knowledge about asymptotic behavior of the APX with respect to large imaginary frequencies is important since the quality of the frequency grid degrades with vanishing band gap. APX has a different behavior for large frequencies in the Uniform Electron Gas than the Random Phase Approximation, as discussed in Subsection 8.2.2. However, since APX requires a different calculation setup with less k-points but higher plane wave cutoff momenta, evaluating APX and RPA on different frequency grids in metallic systems does not pose a considerable disadvantage.

8.3.3   Lattice constants

Calculating lattice constants beyond the Random Phase Approximation requires sub-meV accuracy for the energy difference at different volumes of the system under consideration. In this case, the basis set extrapolation of the APX energy differences does not require more than one term in the expansion of the large momentum behavior. In fact, the quality of the extrapolation deteriorates when using more than one term in the expansion since the higher order terms mostly cancel in the energy difference. Figure 8.11 shows the basis set convergence of the energy difference for LiF with 10 electrons. The volumes of the primitive cells are $15.9\,\text{Å}^3$ and $15.4\,\text{Å}^3$. The data contains considerable aliasing effects since the number of bands must be a multiple of the number of cores employed by the calculation, such that the number of bands is not always equally close to the maximum number of plane waves supported by the respective cutoff energy. All calculations were conducted with a $3 \times 3 \times 3$ k-points mesh, providing sufficient accuracy, as indicated in the inset of Figure 8.11.

At each volume, the Adjacent Pairs Exchange correction is calculated and converged with respect to the cutoff energy using VASP with a PBE-DFT reference. The Exact-Exchange+ RPA results were taken from the Birch Murnaghan fit of previous converged RPA calculation,
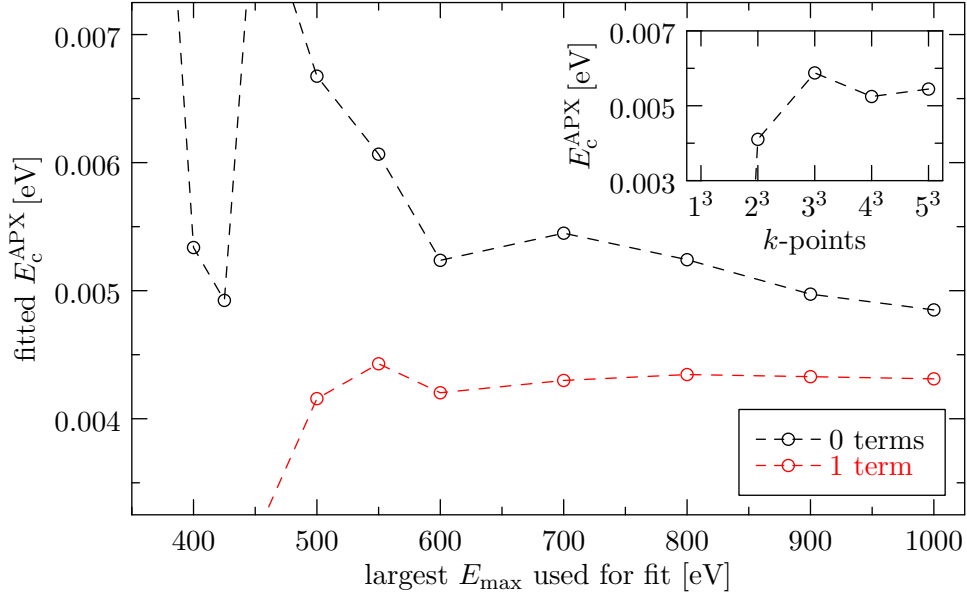
Figure 8.11: Basis set extrapolation of the APX energy difference at different volumes of LiF containing 10 electrons. The volumes of the primitive unit cell are $15.9\,\text{Å}^3$ and $15.4\,\text{Å}^3$. The black points show the energy differences obtained at different cutoff energies E_{max}. Aliasing effects can be clearly seen. The red points show a fit using in the leading order of the expansion of the APX energy with respect to large cutoff momenta. Each fit only uses data points with a cutoff energy below or equal to that of the fitted point. Higher order fits offer no improvement since they largely cancel in the difference. The inset shows the convergence of the APX energy difference with respect to different k point meshes.

Solid		$a_0\,[\text{Å}]$						
		RPA	%	SOSEX	%	APX	%	exp.
C	(A4)	3.572	0.5	3.552	<0.1	3.550	−0.1	3.553
LiH	(B1)	3.983	0.1	3.989	0.3	3.992	0.4	3.979
LiF	(B1)	3.998	0.7	3.955	−0.4	3.974	<0.1	3.972
LiCl	(B1)	5.074	<0.1	—	—	—	—	5.070
NaF	(B1)	4.625	0.9	—	—	—	—	4.582
MgO	(B1)	4.225	0.9	—	—	—	—	4.189
GaP	(B3)	5.442	<0.1	—	—	—	—	5.439

Table 8.3: Lattice constants from the Random Phase Approximation, SOSEX and the Adjacent Pairs Exchange correction compared to experiment. The experimental lattice constants were extrapolated to $T = 0\,\text{K}$ and to exclude the zero point energy (ZPE).

employing the same PAW potentials. The resulting RPA+APX energy is then fit to a Birch-Murnaghan equation of state to retrieve the RPA+APX lattice constants. The pressure derivative of the bulk modulus was taken from ... Table 8.3 lists lattice constants from RPA, SOSEX and APX in comparison with experiment, extrapolated to $T = 0\,\mathrm{K}$ and corrected to exclude the phononic zero point energy.

8.4   Summary and discussion

The Random Phase Approximation exhibits a systematic error which origins, at least partially, from violations of the Pauli exclusion principle. As discussed in the beginning of Chapter 7, violating contributions are canceled by diagrams where the propagators of the offending states are exchanged. In the lowest order only one pair of propagators is exchanged.

The Adjacent Pairs Exchange (APX) correction to the RPA constitutes the largest set of Feynman diagrams correcting as many violations as possible in lowest order without introducing new violations and still forming one ring only:

This makes the Random Phase Approximation plus the Adjacent Pairs Exchange correction a purely *ab-initio* choice of diagrams when the memory scaling for their evaluation must not exceed $\mathcal{O}(N^2)$, since the ring form of the APX allows its evaluation using only polarization parts with 2 open ends and RPA is the most important class of diagrams for high densities, becoming exact in the limit $r_s \to 0$. This argument relies on the prevalence of long ranged states making the RPA an accurate approximation in the first place, which might not hold in the presence of more localized states at the Fermi edge. However, in cases where the RPA offers a good approximation, no test against experiment is required to argue that APX offers the lowest order correction - which makes it *ab-initio*[2].

Table 8.4 compares the SOSEX, the AC-SOSEX and the APX correction to the Random Phase Approximation in terms of contained Goldstone diagrams, along with their respective computational costs in time and memory. The diagrams of SOSEX constitute the largest set of Goldstone, rather than Feynman, diagrams correcting as many violations as possible under the same conditions than in the APX. In the case of SOSEX, forming a ring is necessary for the applicability of the direct ring Coupled Cluster Doubles amplitudes, which can be constructed in $\mathcal{O}(N^5)$ steps, as discussed in Section 6.2. Dropping the condition for the SOSEX diagrams to form a ring raises the time complexity for the construction of the amplitudes to $\mathcal{O}(N^6)$. Accepting this time complexity and the memory complexity of SOSEX, the full Coupled Cluster Singles and Doubles (CCSD) approximation can be employed. It includes considerably more diagrams, as indicated in Table 8.4, relieving the need of a correction to the Random Phase Approximation in general. In cases, where CCSD is known to be less accurate, as for instance in dissociation processes, the distinguishable Coupled Cluster method may offer improvement at the same computational costs.

---

[2]Still, only a test against the uniform electron gas induced further examination of the two sided APX and the possibility of new violations introduced by it. Testing against systems - theoretical or not - is therefore necessary, of course.
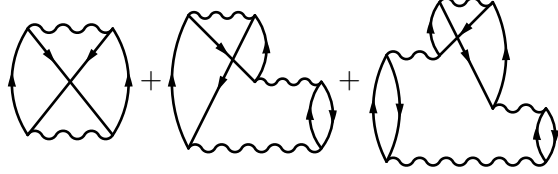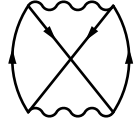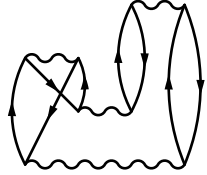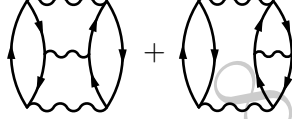
approximation	Goldstone diagrams	time	memory
SOSEX	$+$ ... $+$ ... $+$ ...	$\mathcal{O}(N^5)$	$\mathcal{O}(N^4)$
AC-SOSEX	$+ \frac{1}{3}$ (... $+$ ... $+$ ...) $+$ ...	$\mathcal{O}(N^5)$	$\mathcal{O}(N^2)$
APX	SOSEX $+$ $+$ ...	$\mathcal{O}(N^5)$	$\mathcal{O}(N^2)$
CCSD	RPA $+$ APX $+$ $+$ ... $+$ ...	$\mathcal{O}(N^6)$	$\mathcal{O}(N^4)$

Table 8.4: Comparison of different approximations beyond the Random Phase Approximation, showing the lowest order Goldstone diagrams introduced by the respective approximation. The AC-SOSEX is not derived within the same many-body perturbation theory framework as the other approximations. It can, however, be translated into Goldstone diagrams when including swapped ladder diagrams, as shown here in third order and which are discussed in Section 7.3.

Including exchange diagrams to cancel violating contributions in the RPA diagrams offers an *ab-initio* strategy for selecting the lowest order diagrams of many-body perturbation theory, correcting for RPA's systematic error. In the framework of the Adiabatic Connection, the unknown exchange-correlation kernel $\mathbf{f}_{xc}^\lambda$, occurring in the Dyson-like equation (6.27) of the polarizability $\mathbf{X}_\lambda$, has to be included for a correction to the RPA. The AC-SOSEX contains the exchange-correlation kernel in lowest order:

$$\mathbf{X}_\lambda^{\text{AC}-\text{SOSEX}} = \mathbf{X}_0 \tilde{\mathbf{f}}_{xc}^\lambda \mathbf{X}_0 + \mathbf{X}_0 \tilde{\mathbf{f}}_{xc}^\lambda \mathbf{X}_0 \lambda \mathbf{V} \mathbf{X}_0 + \dots ,$$

approximating the kernel by $\tilde{\mathbf{f}}_{xc}^\lambda$, which is given implicitly by

$$\mathbf{X}_0 \tilde{\mathbf{f}}_{xc}^\lambda \mathbf{X}_0 = \lambda \left(\vphantom{\Bigg(} \quad + \quad + \quad + \quad \right) .$$

In the first and in the last diagram, particles turn into holes and vice versa at the Coulomb interaction, which has no correspondence in many-body perturbation theory. This is, therefore, not an obvious choice for an approximation in the author's opinion. It neither originates

from time dependent DFT nor from many-body perturbation theory, which is employed by AC-RPA after all to calculate the independent particle polarizability $\mathbf{X}_0$. As discussed in Section 7.2, the above approximation rather comes from transforming the RPA energy expression into the particle/hole basis, applying the analogy of SOSEX to exchange two indices, ignoring the time order, and then transforming it back to the position basis. However, the results are very similar to those of SOSEX for reasons discussed in Section 7.3, which are in no obvious connection to its derivation. Owing to its similar results to SOSEX, the AC-SOSEX can be considered a numerical recipe to approximate the SOSEX energy, requiring only $\mathcal{O}(N^2)$ of memory.

The Adjacent Pairs Exchange corrections contains more diagrams than the Second Order Screened Exchange correction since APX is the pendant of SOSEX in terms of Feynman diagrams rather than Goldstone diagrams. This does, however, not imply that APX is more accurate in any given situation. After all, the surprisingly high accuracy of SOSEX or APX in case of the uniform electron gas is certainly fortuitously and no theory, involving only first and second order exchange diagrams can be expected to provide this accuracy in general. The spin-polarized uniform electron gas is an example of a system, where RPA+SOSEX or RPA+APX can yield zero or even positive correlation energies in the limit of dilute densities. For densities of real metals, the performance in the spin-polarized case is better. APX misses an accurate correction to RPA by less than 20% and SOSEX is slightly better. It is assumed that AC-SOSEX is close to SOSEX since no SOSEX calculations for the spin-polarized UEG in the thermodynamic limit have been found. It is worth mentioning that finite spin-polarized systems often exhibit a (quasi)-degenerate ground state, rendering many-body perturbation theory, as discussed here and employed by most implementations, inaccurate at best. (Quasi)-degenerate many-body perturbation theory is discussed, for instance, in (Shavitt and Bartlett 2009).

APX and SOSEX are identical up to third order resulting only in small differences. In the case of the non-spin-polarized uniform electron gas, RPA+SOSEX matches Quamtum Monte Carlo correlation energies already at $r_s \approx 5$, where RPA+APX still has an error of about than $0.7\,\mathrm{m}E_h$ per electron, which is a relative error 5%. For lower densities with $r_s > 8$, where correlation effects are more prevalent, APX improves on SOSEX and its accuracy is never worse than $0.3\,\mathrm{m}E_h$ per electron, even up to $r_s = 50$. Note, that the accuracy is given with respect to the (Perdew and Zunger 1981) fit of the (Ceperley and Alder 1980) QMC resutls. The Adjacent Pairs Exchange correction can be computed in $\mathcal{O}(N^5)$ with a memory requirement scaling like $\mathcal{O}(N^2)$. This is equivalent to the AC-SOSEX but considerably less memory demanding than SOSEX. If a memory demand of $\mathcal{O}(N^3)$ is permissible, APX and AC-SOSEX can also be evaluated in $\mathcal{O}(N^4)$ steps. Both, APX and AC-SOSEX are implemented in `VASP` and first applications on lattice constants show excellent agreement with experiment. A more extensive survey including atomization energies is still to be made.

Not all improvements beyond the Random Phase Approximation are based on the inclusion of exchange processes. In the GW approximation the iterative scheme of RPA, used to build an effective interaction W from the Coulomb interaction V according to (6.7), is extended by an iterative scheme to improve the description of the propagator G_0 towards an effective propagator G of the fully interacting system, referred to as *dressed* propagator. There is a whole family of such approximations, based on the work of (Hedin 1965). The central quantity of interest in these approximations is the dressed propagator, rather than connected diagrams, as in the Goldstone approach of many-body perturbation theory, discussed here. This makes a comparison between the two approaches hard, as there is no consideration of symmetries

and the propagators are approximated by merely shifting the poles of the initial propagators G_0. In most cases the dressed propagator is used to retrieve excitation spectra but there are also total energy calculations within the GW approximation, usually employing the formula of (Galitskii and Migdal 1958). In Appendix A, an alternative approach is suggested to evaluate the total energy in the G_0W_0 approximation strictly within the many-body perturbation theory discussed here. The total energies retrieved by this approximation are expected to be more accurate than those of the RPA at computational costs that should not exceed $\mathcal{O}(N^4)$ but this remains to be tested in the future. Also, G_0W_0 is only the least accurate approximation of the mentioned family of approximations, depending on the reference such as DFT or HF and further, exchange effects are known to be important not only to correct for violations of the exclusion principle, so it is unclear, whether G_0W_0 total energies are a viable option to RPA+APX or RPA+AC-SOSEX.

Finally, it is worth mentioning that most of time and memory requirement of high accuracy methods, such as Coupled Cluster Singles and Doubles (CCSD) strongly depends on the number of unoccupied states ψ_a, needed for a convergent result. This number can be reduced without considerably sacrificing the accuracy such that CCSD or even higher accuracy methods become feasible for larger systems. One way of reducing the number of unoccupied states is by means of natural orbitals, applicable in the case where large voids are between the atoms or molecules, such as in atomization energy calculations of solids. Another way of reducing the number of unoccupied states is by including explicit correction already in the description of the unperturbed system. This can be done by augmenting the Slater determinant, which is a product of functions depending on one electron position only, by a set of functions $f(\mathbf{x}_1, \mathbf{x}_2)$ explicitly depending on two electron positions, hence the name f_{12} methods. In all cases there is still an underlying perturbation expansion to be evaluated and the Adjacent Paris Correction as well as AC-SOSEX can also profit from such a reduction of the number of unoccupied states.

Draft 0.8

Bibliography

Güttinger, P. (Aug. 1932). "Das Verhalten von Atomen im magnetischen Drehfeld". *Z. Physik* 73.3-4, pp. 169–184. DOI: `10.1007/BF01351211`.

Møller, C. and M. S. Plesset (Oct. 1934). "Note on an Approximation Treatment for Many-Electron Systems". *Phys. Rev.* 46.7, pp. 618–622. DOI: `10.1103/PhysRev.46.618`.

Macke, W. (1950). "Über die Wechselwirkungen im Fermi-Gas, Polarisationserscheinungen, Correlationsenergie, Elektronenkondensation". *Z. Naturforsch.* 5a.8, pp. 192–208.

Wick, G. C. (Oct. 1950). "The Evaluation of the Collision Matrix". *Phys. Rev.* 80.2, pp. 268–272. DOI: `10.1103/PhysRev.80.268`.

Shanks, D. (1955). "Non-linear transformation of divergent and slowly convergent sequences". *J. Math. Phys.* 34.1, pp. 1–42.

Gell-Mann, M. and K. A. Brueckner (Apr. 1957). "Correlation Energy of an Electron Gas at High Density". *Phys. Rev.* 106.2, pp. 364–368. DOI: `10.1103/PhysRev.106.364`.

Goldstone, J. (Feb. 1957). "Derivation of the Brueckner Many-Body Theory". *Proceedings of the Royal Society A: Mathematical, Physical and Engineering Sciences* 239.1217, pp. 267–279. DOI: `10.1098/rspa.1957.0037`.

Galitskii, V. M. and A. B. Migdal (1958). "Application of quantum field theory methods to the many body problem". *Sov. Phys. JETP* 7.1, pp. 96–104.

Coester, F. and H. Kümmel (June 1960). "Short-range correlations in nuclear wave functions". *Nuclear Physics* 17, pp. 477–485. DOI: `10.1016/0029-5582(60)90140-1`.

Adler, S. L. (Apr. 1962). "Quantum Theory of the Dielectric Constant in Real Solids". *Phys. Rev.* 126.2, pp. 413–420. DOI: `10.1103/PhysRev.126.413`.

Wiser, N. (Jan. 1963). "Dielectric Constant with Local Field Effects Included". *Phys. Rev.* 129.1, pp. 62–69. DOI: `10.1103/PhysRev.129.62`.

Hedin, L. (Aug. 1965). "New Method for Calculating the One-Particle Green's Function with Application to the Electron-Gas Problem". *Phys. Rev.* 139.3A, A796–A823. DOI: `10.1103/PhysRev.139.A796`.

Onsager, L., L. Mittag, and M. J. Stephen (Jan. 1966). "Integrals in the Theory of Electron Correlations". *Ann. Phys.* 473.1-2, pp. 71–77. DOI: `10.1002/andp.19664730108`.

Čížek, J. (1969). "On the Use of the Cluster Expansion and the Technique of Diagrams in Calculations of Correlation Effects in Atoms and Molecules". *Advances in Chemical Physics*. Ed. by R. LeFebvre and C. Moser. John Wiley & Sons, Inc., pp. 35–89.

Freeman, D. (June 1977). "Coupled-cluster expansion applied to the electron gas: Inclusion of ring and exchange effects". *Physical Review B* 15.12, pp. 5512–5521. DOI: `10.1103/PhysRevB.15.5512`.

Ceperley, D. M. and B. J. Alder (Aug. 1980). "Ground State of the Electron Gas by a Stochastic Method". *Phys. Rev. Lett.* 45.7, pp. 566–569. DOI: `10.1103/PhysRevLett.45.566`.

Vosko, S. H., L. Wilk, and M. Nusair (Aug. 1980). "Accurate spin-dependent electron liquid correlation energies for local spin density calculations: a critical analysis". *Can. J. Phys.* 58.8, pp. 1200–1211. DOI: `10.1139/p80-159`.

Perdew, J. P. and A. Zunger (May 1981). "Self-interaction correction to density-functional approximations for many-electron systems". *Phys. Rev. B* 23.10, pp. 5048–5079. DOI: `10.1103/PhysRevB.23.5048`.

Scuseria, G. E. and H. F. Schaefer (1989). "Is coupled cluster singles and doubles (CCSD) more computationally intensive than quadratic configuration interaction (QCISD)?" *The Journal of Chemical Physics* 90.7, p. 3700. DOI: `10.1063/1.455827`.

Almlöf, J. (June 1991). "Elimination of energy denominators in Møller—Plesset perturbation theory by a Laplace transform approach". *Chemical Physics Letters* 181.4, pp. 319–320. DOI: `10.1016/0009-2614(91)80078-C`.

Peskin, M. E. and D. V. Schroeder (1995). *An introduction to quantum field theory*. Reading, Mass: Addison-Wesley Pub. Co.

Holm, B. and F. Aryasetiawan (Aug. 2000). "Total energy from the Galitskii-Migdal formula using realistic spectral functions". *Phys. Rev. B* 62.8, pp. 4858–4865. DOI: `10.1103/PhysRevB.62.4858`.

Fetter, A. L. and J. D. Walecka (2003). *Quantum theory of many-particle systems*. Mineola, N.Y: Dover Publications.

Preparata, F. P. and M. I. Shamos (2008). *Computational geometry: an introduction*. 6. print. Texts and monographs in computer science. New York: Springer.

Grüneis, A., M. Marsman, J. Harl, L. Schimka, and G. Kresse (Oct. 2009). "Making the random phase approximation to electronic correlation accurate". *The Journal of Chemical Physics* 131.15, p. 154115. DOI: `10.1063/1.3250347`.

Kutzelnigg, W. (Dec. 2009). "How many-body perturbation theory (MBPT) has changed quantum chemistry". *International Journal of Quantum Chemistry* 109.15, pp. 3858–3884. DOI: `10.1002/qua.22384`.

Shavitt, I. and R. J. Bartlett (2009). *Many-body methods in chemistry and physics: MBPT and coupled-cluster theory*. Cambridge; New York: Cambridge University Press.

Ziesche, P. (Sept. 2010). "The high-density electron gas: How momentum distribution $n(k)$ and static structure factor $S(q)$ are mutually related through the off-shell self-energy $\Sigma(k,\omega)$". *Annalen der Physik* 522.10, pp. 739–765. DOI: `10.1002/andp.201000022`.

Ren, X., P. Rinke, G. E. Scuseria, and M. Scheffler (July 2013). "Renormalized second-order perturbation theory for the electron correlation energy: Concept, implementation, and benchmarks". *Phys. Rev. B* 88.3, p. 035120. DOI: `10.1103/PhysRevB.88.035120`.

Kaltak, M., J. Klimeš, and G. Kresse (Aug. 2014a). "Cubic scaling algorithm for the random phase approximation: Self-interstitials and vacancies in Si". *Phys. Rev. B* 90.5, p. 054115. DOI: `10.1103/PhysRevB.90.054115`.

— (June 2014b). "Low Scaling Algorithms for the Random Phase Approximation: Imaginary Time and Laplace Transformations". *J. Chem. Theory Comput.* 10.6, pp. 2498–2507. DOI: `10.1021/ct5001268`.

Lancaster, T. and S. Blundell (2014). *Quantum field theory for the gifted amateur*. First Edition. Oxford: Oxford University Press.

Coleman, P. (Oct. 2015). *Introduction to Many-Body Physics*. New York, NY: Cambridge University Press.

Part IV

Appendices

Appendix A

Total energies in G_0W_0 from connected diagrams

Given the propagator G_0 in matrix form and in imaginary time according to (6.11)[1]

$$\mathbf{G}_{0\mathbf{xx}'}(i\tau) = \begin{cases} -\sum_i \psi_i(\mathbf{x})\psi_i^*(\mathbf{x}')e^{-(\varepsilon_i-\mu)\tau} & \text{for } \tau \leq 0 \\ +\sum_a \psi_a(\mathbf{x})\psi_a^*(\mathbf{x}')e^{-(\varepsilon_a-\mu)\tau} & \text{otherwise,} \end{cases}$$

we can Fourier transform it to imaginary frequency $\mathbf{G}_0(i\eta)$. We also write the screened Coulomb interaction $\mathbf{W}_0$ in the Random Phase Approximation (RPA) in the same form

$$\begin{aligned} \mathbf{W}_0(i\nu) &= \mathbf{V} + \mathbf{V}\mathbf{X}_0(i\nu)\mathbf{V} + \mathbf{V}\mathbf{X}_0(i\nu)\mathbf{V}\mathbf{X}_0(i\nu)\mathbf{V} + \dots \\ &= \mathbf{V}\left(\mathbf{1} - \mathbf{X}_0(i\nu)\mathbf{V}\right)^{-1}, \end{aligned} \tag{A.1}$$
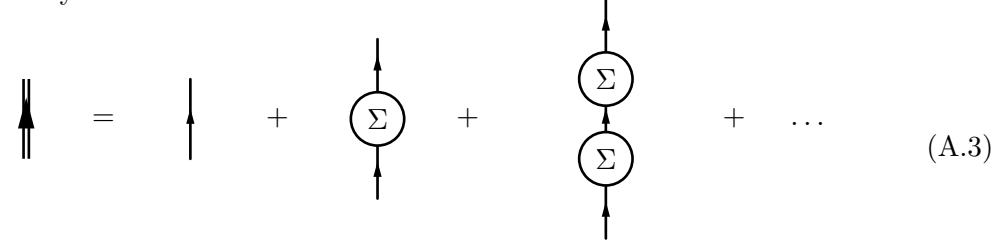
where $\mathbf{X}_0$ is the independent particle polarizability in imaginary frequency as retrieved from a Fourier transform of (6.10). The *irreducible self energy* $\boldsymbol{\Sigma}$ can then be approximated in the RPA by

$$\boldsymbol{\Sigma}_{0\mathbf{xx}'}(i\eta) = \int_{-\infty}^{\infty} \frac{i\,d\nu}{2\pi} \mathbf{G}_{0\mathbf{xx}'}(i\eta + i\nu)\left(\mathbf{W}_{0\mathbf{xx}'}(i\nu) - \mathbf{V}_{\mathbf{xx}'}\right). \tag{A.2}$$

Note that the matrices are multiplied elementwise and that we exclude the exchange term G_0V since it cancels with the effective interaction in a Hartree-Fock reference as discussed in Section

---

[1]Note that the propagator used here differs by a factor of i from the usual definition of the propagator, as discussed in the footnote of (5.42)

5.6. In the G_0W_0 approximation the full propagator $\mathbf{G}$ is approximated by inserting the above approximation to the irreducible self energy $\mathbf{\Sigma}_0$ into the propagator of the unperturbed system $\mathbf{G}_0$ arbitrarily many times

$$\mathbf{G} \quad = \quad \mathbf{G}_0 \quad + \quad \mathbf{G}_0\mathbf{\Sigma}_0\mathbf{G}_0 \quad + \quad \mathbf{G}_0\mathbf{\Sigma}_0\mathbf{G}_0\mathbf{\Sigma}_0\mathbf{G}_0 \quad + \quad \dots,$$

(A.3)

where we omit the imaginary frequency argument for brevity. Properties of the interacting system can then be extracted from this approximation to the full propagator $\mathbf{G}$. To get the total energy the formula of (Galitskii and Migdal 1958) can be used on the full imaginary time propagator $\mathbf{G}(i\tau)$, retrieved from an inverse Fourier transform of $\mathbf{G}(i\eta)$ at $\tau \to 0$ from above:

$$E = -\frac{i}{2} \int d\mathbf{x} \lim_{\mathbf{r}' \to \mathbf{r}} \lim_{\tau \to 0^+} \left(\frac{\partial}{i\,\partial\tau} - i\,\hat{h}_\mathbf{x} \right) \mathbf{G}_{\mathbf{r}\alpha\,\mathbf{r}'\alpha}(i\tau),$$

(A.4)

where $\hat{h}_\mathbf{x}$ is the single body Hamiltonian of the unperturbed system acting on $\mathbf{G}_\mathbf{x}$. This can be interpreted as cutting out one occurrence of G_0 by the differential operator and then closing the remaining diagrams contained in G (Ziesche 2010).

Here, an alternative way to the Galitskii-Migdal formula is proposed for evaluating the total energy in G_0W_0, respecting the symmetries of all connected diagrams occurring in this approximation, as discussed in Subsection 5.8.2. Figure A.1 shows all diagrams order by order, where each row contains an order of the expansion of $\mathbf{W}_0$ contained in $\mathbf{\Sigma}_0$ according to (A.1) and each column contains an order of $\mathbf{G}$ according to (A.3). Note that the symmetries of the first column differ from the symmetries of all other columns since closing $\mathbf{\Sigma}_0$ with one $\mathbf{G}_0$ forms a bubble equivalent to $\mathbf{X}_0$. The diagrams of the first column form the ring diagrams of the RPA. All the remaining diagrams have rotational symmetry but no reflection symmetry and can be summed to infinite order in the same fashion as it was done in the RPA in (6.8), arriving at

$$E_c^{G_0W_0} = E_c^{\mathrm{RPA}} + i \int \frac{i\,d\eta}{2\pi} \mathrm{tr} \left\{ -\frac{1}{2}\Big(\mathbf{G}_0(i\eta)\Sigma_0(i\eta) \Big)^2 - \frac{1}{3}\Big(\mathbf{G}_0(i\eta)\Sigma_0(i\eta) \Big)^3 - \dots \right\}$$

$$= E_c^{\mathrm{RPA}} - \int_{-\infty}^{\infty} \frac{d\eta}{2\pi} \mathrm{tr} \Big\{ \log\Big(\mathbf{1} - \mathbf{G}_0(i\eta)\mathbf{\Sigma}_0(i\eta) \Big) + \mathbf{G}_0(i\eta)\mathbf{\Sigma}_0(i\eta) \Big\}.$$

(A.5)

This approach still has to be tested and compared to previous G_0W_0 total energies, as for instance retrieved by (Holm and Aryasetiawan 2000). The two approaches do differ after all. Conventional G_0W_0 uses a normalization factor for calculating $\mathbf{G}$ while this approach uses symmetry factors. An implementation for the uniform electron gas in the thermodynamic limit is still ongoing.

$$E_c^{G_0W_0} \;=\; E_c^{\mathrm{RPA}} \;-\; \frac{1}{2}\Big(\mathbf{G}_0(\mathrm{i}\eta)\mathbf{\Sigma}_0(\mathrm{i}\eta)\Big)^2 \;-\; \frac{1}{3}\Big(\mathbf{G}_0(\mathrm{i}\eta)\mathbf{\Sigma}_0(\mathrm{i}\eta)\Big)^3 \;-\; \dots$$

Figure A.1: Connected (closed) diagrams occurring in the G_0W_0 approximation of the correlation energy. The parts of the self energy are given in blue while the parts of the closing propagator are given in red. With each column the number of insertions of $\mathbf{\Sigma}_0\mathbf{G}_0$ into $\mathbf{G}$ increments, while the number of insertions of $\mathbf{X}_0\mathbf{V}$ into $\mathbf{\Sigma}_0$ increments with each row. The single Fermion loop in the center results in a negative Fermion sign of all diagrams beyond RPA. Imaginary units, the imaginary frequency integration and the trace are omitted for clarity.